The Hydrogen-Storage Challenge: Nanoparticles for Metal-Catalyzed Ammonia Borane Dehydrogenation

Clève D Mboyi, Didier Poinsot, Julien Roger, Katia Fajerweg, Myrtil L Kahn, Jean-Cyrille Hierso

To cite this version:

Clève D Mboyi, Didier Poinsot, Julien Roger, Katia Fajerweg, Myrtil L Kahn, et al.. The Hydrogen-Storage Challenge: Nanoparticles for Metal-Catalyzed Ammonia Borane Dehydrogenation. Small, 2021, pp.2102759. 10.1002/smll.202102759 . hal-03359543

HAL Id: hal-03359543
https://hal.science/hal-03359543v1

Submitted on 30 Sep 2021

Review

The hydrogen-storage challenge: nanoparticles for metal-catalyzed ammonia borane dehydrogenation

Clève D. Mboyi,[a] Didier Poinsot,[a] Julien Roger,[a] Katia Fajerwerg,[b] Myrtil L. Kahn,[b] and Jean-Cyrille Hierso*[a]

Dedicated to Prof. Peter. R. Schreiner on the occasion of his 55th birthday for his inspiring friendship, energy and enthusiasm

[a] Dr. C. D. Mboyi, D. Poinsot, Dr. J. Roger, Prof. Dr. J.-C. Hierso
Institut de Chimie Moléculaire de l’Université de Bourgogne (ICMUB) UMR-CNRS 6302
Université Bourgogne Franche-Comté (UBFC)
9 avenue Alain Savary, 21078 Dijon (France)
E-mail: jean-cyrille.hierso@u-bourgogne.fr

[b] Dr. K. Fajerwerg, Dr. M. L. Kahn
Laboratoire de Chimie de Coordination (LCC-CNRS), Université de Toulouse, INPT,
205 route de Narbonne 31077 Toulouse Cedex 4 (France)

TO CITE THIS PAPER:

Clève D. Mboyi, Didier Poinsot, Julien Roger, Katia Fajerwerg, Myrtil L. Kahn, and Jean-Cyrille Hierso, Small 2021, 2102759

https://doi.org/10.1002/smll.202102759

Review

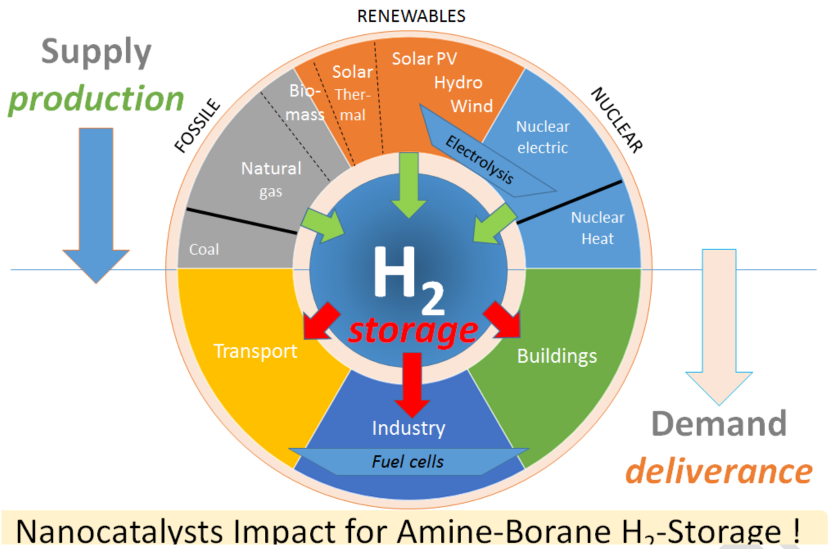

ABSTRACT

Dihydrogen is one of the sustainable energy vectors envisioned for the future. However, the rapidly reversible and secure storage of large quantities of hydrogen is still a technological and scientific challenge. In this context, this review proposes a recent state-of-the-art on H_2 production capacities from the dehydrogenation reaction of ammonia borane (and selected related amine-boranes) as a safer solid-source of H_2 by hydrolysis (or solvolysis), according to the different developed nanoparticle-based catalysts. The review groups the results according to the transition metals constituting the catalyst according a special view to current cost/availability consideration. This includes the noble metals Rh, Pd, Pt, Ru, Ag, as well as transition metals such as Co, Ni, Cu, and Fe. For each element, the monometallic and polymetallic structures, isolated or supported, are presented and the performances described in terms of TOF and recyclability. The structure-property links are highlighted whenever possible. It appears from all these works that the mastery of the preparation of catalysts remains a crucial point; not only in terms of process but also in terms of mastery of the electronic structures of the elaborated nanomaterials. A particular effort of the scientific community remains to be made in this multidisciplinary field with major societal stakes.

CONTENT

ABBREVIATIONS

(3-aminopropyl)triethoxysilane (APTS)
ammonia borane (AB)
aminoborane (H_2NBH_2)
2,2′-bipyridine-5,5′-dicarboxylic acid (H_2bpdc)
carbon nanotube (CNT)
covalent triazine framework (CTF)
dimethylamine borane (DMAB)
dodecaborate-based supramolecular organic frameworks (BOFs)
double solvent approach (DSA)
electron energy loss spectroscopy (EELS)
energy dispersive X-ray spectroscopy (EDS)
ethylenediamine bisborane (EDAB)
Fourier transformed extended X-ray absorption fine structure (FT-EXAFS)
graphene oxide (GO)
graphitic carbon nitride (g-C_3N_4)
high-resolution transmission electron microscopy (HRTEM)
high-angle annular dark-field imaging (HAADF)
hollow porous carbon spheres (HPCS)
hydrazine borane (HB)
liquid organic hydrogen carrier (LOHC)
localized surface plasmon resonance (LSPR)
ionic liquid (IL)
Ketjen Black (KB)
mesoporous carbon nitride (MCN)
mesoporous graphitic carbon nitride (mpg-CN)
methylamine borane (MeAB)
metal organic framework (MOF)
nanodiamond (ND)
nanoparticle (NP)
nitrogen-doped carbon nanotube (NCNT)

nitrogen-doped graphene (NG)
nitrogen-doped reduced graphene oxide (N-rGO)
polydopamine (PDA)
polyethylenimine (PEI)
polyhalogenated aromatics (PHAs)
poly(N-vinyl-2-pyrrolidone) (PVP)
porous coordination cage (PCC)
reduced graphene oxide (rGO)
reverse-double solvent approach (R-DSA)
room temperature (RT)
scanning transmission electron microscopy (STEM)
scanning electron microscopy (SEM)
single-atom alloy (SAA)
supported ionic liquid phase (PsIL)
total turnover number (TTO)
transmission electron microscopy (TEM)
triethylene glycol-terminated dendrimers (TGD)
turnover frequency (TOF)
Vulcan carbon (VC)
X-ray absorption near-edge structure (XANES)

1. INTRODUCTION

Developing a sustainable future energy policy requires humanity to focus not only on the scientific and technical challenges, but also on decisive adaptations by the socioeconomic system and a change in individual and collective attitudes towards energy.[1] That said, the priority scientific issue clearly concerns the depletion of oil reserves and anthropogenic global planet warming that is also related to a constant increase in emissions of greenhouse gases. A hydrogen-based economy is one potential approach towards a controlled and progressive change in our standard of living, while lowering carbon dioxide warming and toxic gas emissions.[2]

Hydrogen is the most abundant element in the universe, about 75% by mass of known matter, and is among the most-abundant element on the Earth's surface. Yet, as simple corpse, H_2 hydrogen gas is very rare in our atmosphere. The chemical energy per mass of hydrogen (142 MJ kg^{-1}) is larger than that of other chemical fuels, especially liquid hydrocarbons from petrol (47 MJ kg^{-1}). Once produced, H_2 is a clean synthetic fuel whose oxidation exhausts water vapor as gas (the formation of toxic nitrogen oxides NO_x may occur when burnt with air). Electrochemically reacted with oxygen in a fuel cell (which produces electricity and heat), electron transfer from oxygen to hydrogen in an electric engine is not limited by the Carnot efficiency and can reach more than 50% efficiency in transforming chemical to mechanical energy, thus twice as much as the thermal combustion process.[1] In addition to clean hydrogen production, hydrogen-storage is also a major challenge to solve.[3] A very striking example, early on detailed by Schlapbach and Züttel,[1] concerns hydrogen-storage for mobile applications. Considering a vehicle burning about 24 kg of gasoline in a combustion engine for covering 400 km, 8 kg of hydrogen are needed to cover the same range for the combustion engine version and only 4 kg hydrogen for an electric engine with a fuel cell.

While this is good news, H_2 as molecular gas at room temperature (RT) and atmospheric pressure, occupies a volume of 45 m^3 for 4 kg which corresponds to a balloon of 5 m in diameter. Conventional physical storage under high pressure and/or low temperature under gas or liquid forms remains still delicate from technological and economic requirement and societal acceptability. For instance, at 300 bars, an internal volume of 225 liters is needed for 4 kg of hydrogen. Actually, among all issues related to the applications of hydrogen energy, chemical storage focused on secure and efficient hydrogen-storage is regarded as the key solution to be developed. Ideally, hydrogen-storage material should i) absorb and release H_2 quickly, ii) have a high content of hydrogen, iii) have a low molecular weight, and iv) cost effective to produce and regenerate.

This extremely challenging but vital approach has been intensively studied from a diversity of approaches since the year 2000's; rendering gigantic a comprehensive compilation of results and analysis. Accordingly, our present review is focused on a critical discussion of the advances achieved in the promising field of the use of ammonia borane dehydrogenation as source of H_2, achieved from well-defined and characterized transition metal nanoparticles (NPs) –mainly after 2016 since various relevant reviews appeared before–.

However, we would like in preamble providing the reader with a selected panorama of the reviews, surveys, perspectives and opinions, we selected from their relevant point of view and the context and background information they give.[4,5,6,7,8,9,10,11,12,13,14,15,16,17,18,19,20,21,22,23] As summarized in Table 1, Schlapbach and Züttel published in 2001 a general (and indispensable) contribution focused on the context and challenges of hydrogen-storage for mobile application.[1] By providing a didactic discussion, pragmatically illustrated with many essential quantitative data (for instance, stored hydrogen per mass and per volume: a comparison of metal hydrides, carbon nanotubes, petrol and other hydrocarbons as H carrier) they early on set a critical/political vision of the topic, concluding that "*Sustainability — and humanity — will profit if the price we pay for energy includes costs for long-term production, transport and distribution of energy, materials, and restoration of the damaged environment*." Relevant concise general discussions about hydrogen energy, including aspects such as needs, production, storage, transportation, distribution, and end-uses of hydrogen fuel are also available.[2,3] The more focused question of ammonia borane (AB, $H_3N{\rightarrow}BH_3$) usable to transport and store hydrogen for fueling automobiles was discussed by Marder in a 2007 highlight paper,[4] mainly on the basis of molecular transition metal complexes as pre-catalysts for AB dehydrogenation (10% Pd on charcoal was also employed[24]). On this theme more detailed discussions followed, with the contributions by Baker and Manners,[5,6,10] notably addressing the preparation and physical/chemical properties of ammonia borane, aminoborane, iminoborane and derivatives, as well as their reactivity under thermolysis, in the presence of transition metals and in solvolysis. Of particular interest is the contribution of Demirci,[7] which described precisely how and why, sodium borohydride ($NaBH_4$) that was presented in the early 2000s as a promising hydrogen storage material (with a convenient theoretical gravimetric hydrogen storage capacity of 10.8 wt%) was recommended as no-go for on-board automotive hydrogen storage despite ten years of significant progress (notably because of too low effective gravimetric H_2 storage capacities, inefficiency of recycling of hydrolysis by-product $NaBO_2$ and global cost). This, illustrating in a "real" case the challenging combination of properties sought after: adequate gravimetric–volumetric storage capacity, thermodynamic stability, high kinetic of hydrogen generation, reversibility of storage (regeneration) and cost efficiency. Based on the assessment that the control over the nature of final reaction product(s) resulting from the dehydrogenation of AB is essential in recognizing the potential utility of a system as a fuel provider, Gordon *et al.* examined the mechanisms of dehydrogenation for various molecular catalysts in different conditions and also chemical regeneration of nitrogen/boron-based waste (polyborazylene).[9] The essential question of liquid-phase hydrogen-storage materials –related with potential high temperatures for hydrogen desorbing and limited kinetics for recharging in the solid-state– was reviewed by Xu in 2010.[8] A discussion was provided concerning: *i*) catalytic hydrolysis of sodium and lithium borohydrides and ammonia borane, other solid catalysts, *ii*) decomposition of the RT liquids hydrazine and formic acid, either under heterogeneous or homogeneous conditions. This survey introduced a series of pertinent review works by Xu group, dedicated to hydrolysis and solvolysis with heterogeneous catalysts.[11,13,15] The reviews by Özkar and Xu,[14,15,18] highlighted the progressive shift operated by both the "homogeneous" and "heterogeneous" chemist community to a tightly related, almost unified, view of metal-catalyzed ammonia borane dehydrogenation efficiently achieved by cluster and nanoparticle catalysts,[25,26,27,28,29,23] either supported or not.[30,31,32,33] A number of anterior reviews that are pertinent in the context of the H_2 storage challenge are worth consulting; in particular compilation/comparison of catalyst performances can be found.[15,18] Also, some are centered on amine-boranes and derivatives,[12] or extensively treating ammonia borane,[17] dehydrogenation mechanisms,[16] or alternative approaches for storage/production of H_2 (like liquid organic H_2 carriers, LOHCs)[20,21,22] or treating of supported or colloidal nanocatalysts.[19,23]

Table 1. Selection of general and more specialized reviews on chemical hydrogen-storage

Title	Authors	Year	Ref
Hydrogen-storage materials for mobile applications	Schlapbach, L. *et al.*	2001	**[1]**
The hydrogen issue	Armaroli, N. *et al.*	2011	**[2]**
Hydrogen storage: materials, methods and perspectives	Pandith, A. H. *et al.*	2015	**[3]**
Will we soon be fueling our automobiles with ammonia–borane?	Marder, T. B.	2007	**[4]**
Ammonia–borane: the hydrogen source par excellence	Baker, T. *et al.*	2007	**[5]**
B–N compounds for chemical hydrogen storage	Manner, I. *et al.*	2009	**[6]**
Ten-year efforts and a no-go recommendation for sodium borohydride for on-board automotive hydrogen storage	Demerci, U. B. *et al.*	2009	**[7]**
Liquid-phase chemical hydrogen storage: catalytic hydrogen generation under ambient conditions	Xu, Q. *et al.*	2010	**[8]**

Ammonia borane as a hydrogen carrier: dehydrogenation and regeneration	Gordon, J.-C. *et al.*	2010	**[9]**
Ammonia-borane and related compounds as dihydrogen sources	Manner, I. *et al.*	2010	**[10]**
Catalytic hydrolysis of ammonia borane for chemical hydrogen storage	Xu, Q. *et al.*	2011	**[11]**
Recent process and development of metal aminoborane	Zhang, J.-G. *et al.*	2013	**[12]**
Synergistic catalysis over bimetallic alloy nanoparticles	Xu, Q. *et al.*	2013	**[13]**
Transition metal nanoparticles in catalysis for the hydrogen generation from the hydrolysis of ammonia-borane	Özkar, S. *et al.*	2013	**[14]**
Dehydrogenation of Ammonia Borane by Metal Nanoparticle Catalysts	Xu, Q. *et al.*	2016	**[15]**
Ruthenium-catalyzed ammonia borane dehydrogenation: mechanism and utility	Williams, T. J. *et al.*	2017	**[16]**
Ammonia borane, a material with exceptional properties for chemical hydrogen storage	Demerci, U. B.	2017	**[17]**
Ammonia borane as hydrogen storage materials	Özkar, S. *et al.*	2018	**[18]**
Recent advances in noble metal catalysts for hydrogen production from ammonia borane	Xu, L. *et al.*	2020	**[19]**
A future energy supply based on liquid organic hydrogen carriers (LOHC)	Teichmann, D. *et al.*	2011	**[20]**
Liquid organic hydrogen carriers (LOHCs): toward a hydrogen-free hydrogen economy	Wasserscheid, P. *et al.*	2017	**[21]**
Recent developments of effective catalysts for hydrogen storage technology using N-ethylcarbazole	Ye, M. *et al.*	2020	**[22]**
Catalysis with Colloidal Ruthenium Nanoparticles	Philippot, K. *et al.*	2020	**[23]**

2. AMMONIA BORANE PROPERTIES AND REACTIVITY

Physical and chemical properties of ammonia borane AB and some important related compounds (*N*-methylamine borane) have been reviewed in details regarding their use as hydrogen carrier, and the reader can refer to these comprehensive reports.[6,17] Some essential properties are worth reminding: ammonia borane is solid at ambient conditions (at 25 °C, M = 30.8 g mol^{-1} and ρ = 0.78 g cm^{-3}) and structurally related to gaseous ethane (at 0 °C, M = 30.0 g mol^{-1}; ρ = 1.36 x10^{-3} g cm^{-3}). While AB and ethane have similar gravimetric hydrogen densities (19.6 wt% and 20.0 wt%, respectively), AB has a much higher volumetric density (146 g_H L^{-1} *vs* less than 0.3 g_H L^{-1}, respectively). AB carry three protic $H^{\delta+}$ and three hydridic $H^{\delta-}$ polarizing hydrogens that ease the release of H_2 via both intra- and intermolecular interactions, which contrast with the high energy covalent C–H bonding in ethane. Dehydrogenation of ethane to ethylene is thus endothermic (ΔH = 32.6 kcal mol^{-1}) as the cleavage of two C–H bonds is not fully balancing the formation of dihydrogen and a C=C double bond.[6] In contrast, dehydrogenation of ammonia borane to aminoborane (H_2NBH_2) is exothermic (ΔH = –5.09 kcal mol^{-1}) as the initial dative (N→B) bond is converted into a stronger covalent one. AB has a melting point of 112−114 °C and is soluble in organic (THF, tetraglyme) and polar solvents –including water and methanol– and some ionic liquids (imidazolium chloride). Below 200 °C, about 13 wt% H_2 can be recovered from ammonia borane (neat AB possesses three equiv. of H_2 but only two equiv. is released at this temperature). In "hydrogen economy" topic, recommendations from United State Department of Energy are often given as reference.[1,7,15] Accordingly, for energy carrier in portable devices and vehicles, hydrogen fuel cells should have high energy content combined with small volume and light mass, the minimum gravimetric and volumetric capacities for hydrogen chemical carriers being 5.5 wt% and 40 g L^{-1} for the year 2025, ultimately increasing up to 6.5 wt% and 50 g L^{-1}. In this regard, AB is very promising. The mechanistic of AB (and derivatives) dehydrogenation, and the resulting products formation, have been investigated experimentally and theoretically.[6,9,10,16,17]

Ammonia borane was originally reported to release hydrogen by thermal treatment, but is actually not suitable for solid-state chemical hydrogen storage since it decomposes (more than it dehydrogenates) forming ammonia, diborane, borazine and complex oligomeric mixtures.[17] Thus, solvolysis and catalytic strategies were developed towards milder H_2 release conditions (down to RT) potentially limiting the amounts of undesirable products. Hydrolysis and other solvolysis (methanolysis)[34,35] of ammonia borane is promoted by the addition of a transition metal catalyst. Because of the recyclability issue, a very large number of heterogeneous catalysts were reported since the mid-2000's. Noble transition metals like rhodium,[36] ruthenium,[37] platinum,[38] palladium,[39] and silver,[40] as well as non-noble metals like nickel,[41] cobalt,[42] copper,[43] iron[44] and various composite multimetallic systems (from bimetallic[45] up to tetrametallic[46]) have been reported as highly active for AB dehydrogenation. Heterogeneous catalysts can be in the form of non-supported nanoparticles,[29,47,48] nanoparticles supported on inorganic oxides (silica,[31,49] alumina,[31,50] ceria,[36,51] TiO_2,[52] *etc.*), on carbon allomorphs[53] (carbon nanotubes CNTs,[38,54,55] graphene,[37,56] graphene oxide derivatives,[57,58] nanodiamond ND,[59] *etc*.), on highly structured mesoporous silica,[60] metal organic framework (MOF),[61,62] and porous organic frameworks,[63] for the most common supports.[64]

There are several types of mechanisms for the catalytic hydrolysis of AB described in the literature. Very recently Liu and Lu *et al.* reviewed the metal-catalyzed hydrolysis of ammonia borane.[48] The dehydrogenation of AB is an exothermic reaction that is achieved either by pyrolysis or solvolysis. The first one, as a thermal decomposition, is assumed to be a stepwise process, where the exact temperature at which a decomposition step occurs are very much dependent on the heating rate and conditions,[6] but generally around 100 ± 30 °C or above. The experimental (spectroscopic and thermogravimetric data) and DFT studies pointed out that such decomposition reaction in solution followed second order kinetics in AB, and that the stability of the AB solution is highly concentration dependent. A more detailed reviewing of data and kinetics of the pyrolysis processes was provided by Manners group.[6] Compared with pyrolysis, solvolysis can release a large amount of hydrogen under much milder conditions. The solvolysis of AB distinguishes to date hydrolysis and alcoholysis. This latter is mainly achieved by consuming methanol as reagent. Aqueous AB rapidly release hydrogen at room temperature in the presence of an acid or metal catalyst. Kinetic studies identified generally reaction order of 0 or 1 regarding [AB] and in the papers reviewed herein the concentration of [AB] in water is ranging between 0.001 and 2.0 M. During the hydrolysis of AB, H_2O and $NH_3 \rightarrow BH_3$ molecules react on or near the surfaces of the metal catalyst, producing and decomposing various intermediate products that were identified experimentally or postulated from DFT,[48] like hydride M–H (M = metal) precursors, or activated complexes which may dissociate and releases H_2 when H_2O and/or OH^- operate.[48] However, the specific hydrolytic mechanism remains unclear and is probably very dependent on the various conditions for each systems. Accordingly, in the following, the mechanistic advances attached to a specific system are briefly discussed when available from in depth studies.

3. NANOPARTICLE CATALYSTS FOR AB DESHYDROGENATION

Until the period 2016-2018, Xu[15] and Özkar[18] independently compiled and compared the performances of heterogeneous and nanoparticle catalysts for AB dehydrogenation: *i*) in terms of turnover frequency (TOF), the selected values ranging between 1 to 2000 mol_{H2} min^{-1} mol^{-1}_{catal}, also denoted min^{-1}, *ii*) regarding the metallic or multimetallic nature of the catalyst, *iii*) their NPs size (*ca.* 1 to 20 nm –while older reports specified bigger sizes up to 100 nm that are less pertinent for achieving NPs with high surface/volume ratio–[8,11]), *iv*) as well as apparent activation energy in the corresponding dehydrogenation reaction (E_a about 12.0 to 80.0 kJ mol^{-1}). Concerning these collected data, ones must keep in mind the corrections made (or not) for the initial TOF values by the estimation of the fraction of active surface sites and sometimes the normalization to a specific metal for multimetallic species. Notably, the performance in catalyst robustness is also assessed by the easiness of recycling, the total cycling runs and activity conservation, related sometimes to the total turnover numbers (TTOs). Besides the most prominent results that we remind herein as state-of-the art standards, the reader is invited to refer to valuable reviews (Table 1). Our discussion focus on the progress achieved in the last three years, with the highly efficient new systems, and innovative concepts ordered along the nature of the metal used. Multimetallic nanoparticle catalysts are also treated in the section of the transition metal considered as chiefly responsible for the activity or being present in superior amount in the alloy.

3.1. Advances in rhodium-based and alloys nanoparticle catalysts

The market price for rhodium in June 2020 was 270,000 USD kg^{-1},[65] compared to 22,000 USD kg^{-1} in 2016 (+1000%),[66] and 41,000 USD kg^{-1} in 2012 (–50%). The high activity of rhodium catalysts in AB dehydrogenation was early on recognized.

The dehydrocoupling of dimethylamine borane (DMAB, $Me_2NH \rightarrow BH_3$, >99% pure) was found to be catalyzed by 0.5 mol % $[Rh(1,5\text{-cod})(\mu\text{-}Cl)]_2$ (cod = 1,5-cyclooctadiene) in toluene solution at 25 °C to give the cyclic aminoborane dimer $[Me_2N\text{–}BH_2]_2$ quantitatively after 8 h of reaction.[25] TEM analysis of the contents of the reaction solution, Hg poisoning experiments and successful multiple recycling, suggested a heterogeneous catalytic process involving Rh(0) colloids formed from the molecular complex. Notably, under these conditions $[Ir(1,5\text{-cod})(\mu\text{-}Cl)]_2$, *trans*-$RuMe_2(PMe_3)_4$, *trans*-$PdCl_2[P(o\text{-tolyl})_3]_2$ where found less active, while Cp_2TiMe_2 and $B(C_6F_5)_3$ did not promoted H_2 evolution. Catalytic dehydrocoupling of AB $NH_3 \rightarrow BH_3$, in diglyme or tetraglyme at 45 °C, was achieved with the formation of the borazine $[HB{=}NH]_3$.

A next important step was the preparation of active supported noble transition metal nanoparticle catalysts. The processing was achieved by a conventional salts impregnation method (5 h calcination at 300 °C / 5 h H_2 reduction at 250 °C). It includes the preparation of rhodium over alumina Rh/γ-Al_2O_3 from $Rh(NO_3)_3$.[31] This rhodium catalyst (2 wt%) composed of 2.5 nm spherical metal particles embedded on the edges of the crystalline γ-Al_2O_3 was highly active for the hydrolysis of AB. A H_2 release ratio of $H_2/NH_3BH_3 = 3.0$ in 1.3 min from aqueous diluted AB (1 wt%) was reported while γ-Al_2O_3 by itself was inactive. Catalytic activity of rhodium was clearly improved by supporting the Rh nanoparticles when compared to the rhodium molecular pre-catalyst.

The preparation of water soluble Rh(0) nanoparticles stabilized by laurate(dodecanoate) anion –and characterized after ethanol precipitation as particles sizing 5.2 ± 2.7 nm– was achieved for exploring Rh-catalyzed hydrolysis of AB. Such nanoparticles were prepared at RT from the mild reduction of $Rh^{III}Cl_3$ by DMAB in aqueous solution in the presence of laurate anion (Rh:laurate molar ratio = 1:25).[33] Nanoparticles in 0.25 mM Rh concentration (substrate/catalyst ratio = 400) leads to a complete hydrolysis of AB yielding 3.0 mol H_2 mol^{-1} within 6 min in air at 25.0 °C (turnover frequency = 200 min^{-1}). Upon recycling, the Rh catalyst conserved 44% of its catalytic activity in the hydrolysis of AB in the 5th run, for an 80,000 TTO over 117 h.

In the following search for recyclable systems of high catalytic efficiency, some noticeable works were reported. On carbon supports for instance, ultrafine Rh NPs of about 1.1 to 3.4 nm were dispersed on carbon nanotubes (CNTs), showing catalytic activity for the hydrolysis of NH_3BH_3 marked with a turnover frequency up to 706 mol H_2 (mol Rh $min)^{-1}$ (TOF = 706 min^{-1}) and retaining 61% of their initial catalytic activity after 5th runs.[55] Dispersed 2.4 nm Rh nanoparticles supported on graphene have been synthesized via a one-step *in situ* procedure by using methylamine borane (MeAB, $H_3CNH_2 \rightarrow BH_3$) as the reducing agent. Such Rh nanoparticles exhibited a 325 min^{-1} TOF toward hydrolysis of AB.[56] Rhodium(0) nanoparticles sizing 1.8–5.3 nm (average diameter of 3.2 ± 0.8 nm) were supported on nanoceria (25 nm) by impregnation of [$RhCl_3 \cdot 3H_2O$] on the support, followed by a mild RT reduction with $NaBH_4$ in aqueous solution.[36] Rh(0)/CeO_2 show a catalytic activity in hydrogen production from the hydrolysis of AB with a TOF of 2010 min^{-1} at 25.0 °C. This activity is preserved at 67% after the 5th run. While the reasons for CeO_2 to be a superior support to any other oxide support tested (Al_2O_3, SiO_2, TiO_2, HfO_2, ZrO_2) are unclear, the authors proposed that a reduction of Ce(IV) to Ce(III) led to a build-up of negative charge on the oxide surface (in a so-called cycling redox process under catalytic conditions), which may favor both the bonding of Rh(0) nanoparticles on the surface and stronger substrate/metal interaction.

Alloying rhodium within bimetallic nanoparticles was also explored with quite success. Poly(N-vinyl-2-pyrrolidone) (PVP) protected rhodium–palladium nanoparticles (Rh–Pd@PVP, sizing 2.5 ± 1.1 nm) were prepared from co-reduction of K_2PdCl_4 and $[RhCl_3{\cdot}3H_2O]$ (1:1) in the presence of PVP (as stabilizer and reducing agent) in ethanol-water mixture at reflux.[45] While the intimate structure of the nanocatalyst[67] was not known (core-shell, mixed, multilayered, core-satellite, *etc.*) –which is often an issue in multimetallic catalysts–, alloy type Rh–Pd@PVP nanoparticles rather than mixtures of monometallic nanoparticles was suggested based on the comparison of the catalytic activities of several samples in the hydrolysis of AB.[45] For Pd@PVP this resulted in a TOF = 182 min^{-1}, for Rh@PVP 228 min^{-1}, for 1:1 physical mixture of [Pd@PVP + Rh@PVP] 430 min^{-1}, and for Rh–Pd@PVP bimetallic 1333 min^{-1}. The Rh–Pd@PVP bimetallic nanoparticles catalyst conserved 78% of its initial catalytic activity in the hydrolysis of AB at the 5th run and provided a TTO = 171,000 over a period of 46 h at 25 °C.

Beside these high level of activity achieved with Rh-based systems, in the most recent years several groups addressed the limitation of reusability of the systems attached to the loss of materials in the recycling processes. To overcome the issues attached to the separation of catalyst particles from the reaction medium by centrifugation, filtration, and the necessary following work-up (washing, drying, dispersion, *etc.*), magnetically separable materials were conceived.[68,69] Rh nanoparticles supported on the surface of Fe_3O_4 and $CoFe_2O_4$ magnetic powders of nanometric size was reported as the first example of magnetically separable rhodium nanocatalysts.[68] In 2020, Özkar group reported the deposition of Rh(0) nanoparticles over Co(II,III) oxide nanopowders as supporting materials, forming Rh/Co_3O_4 (0.5 wt% Rh) magnetically separable nanocatalysts. This catalyst was synthesized by Rh^{3+} deposition on Co_3O_4, followed by RT reduction with sodium borohydride in an aqueous solution.[70] No change in the crystallinity of the Co_3O_4 nanoparticles (of average size 50 nm) was observed after the impregnation and reduction by $NaBH_4$ of Rh(III) on the surface of the support. The TEM image and XPS analysis of Rh/Co_3O_4 indicated the existence of Rh^0 NPs of average 2.7 ± 0.4 nm size. The catalyst provides a TOF of 1800 min^{-1} for H_2 evolution from the hydrolysis of AB at 25.0 °C. The lifetime of Rh/Co_3O_4 nanoparticles shows that it provides a TTO = 1.02×10^6 turnovers in the release of H_2 from the hydrolysis of AB over 45 h at 25.0 °C. Catalytic activity of bare Co_3O_4 was checked as negligible. However, H_2 evolution kinetics data for the hydrolysis of AB indicated an induction period of 3.0 min and a sigmoidal curve (Figure 1, left).

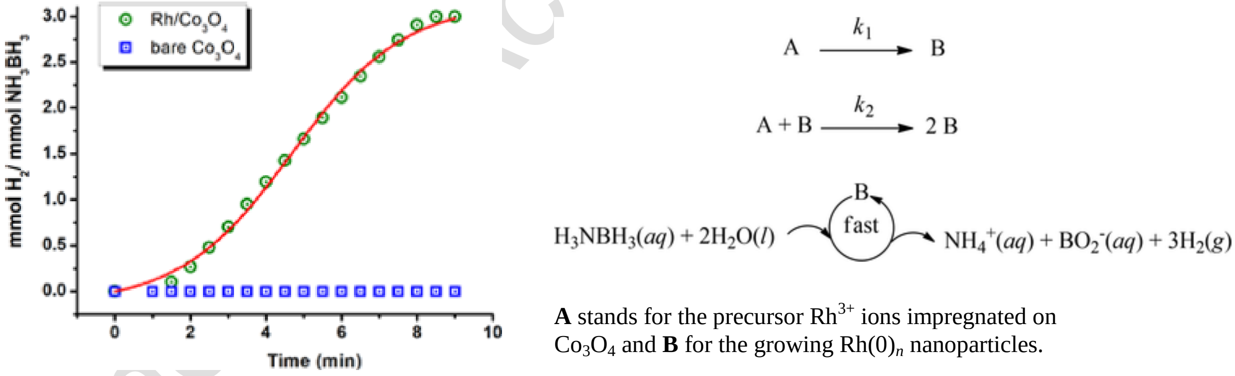

$$H_3NBH_3(aq) + 2H_2O(l) \xrightarrow[\text{fast}]{B} NH_4^+(aq) + BO_2^-(aq) + 3H_2(g)$$

A stands for the precursor Rh^{3+} ions impregnated on Co_3O_4 and **B** for the growing $Rh(0)_n$ nanoparticles.

Figure 1. Left: Kinetic monitoring of AB hydrolysis starting with 5.0 mg of Rh^0/Co_3O_4 (0.5 wt% Rh, [Rh] = 0.024 mM) and 10.0 mL of aqueous solution of AB ([AB] = 100 mM) at 25.0 ± 0.1 °C (green circle and red curve). Blue squares show the null catalytic activity of bare Co_3O_4 in the hydrolysis of AB under the same conditions. Right: Two-step mechanism proposed with slow continuous nucleation (formation of Rh(0) NPs, rate constant k_1), and autocatalytic surface growth (rate constant k_2) and classical total H_2 evolution reaction from AB hydrolysis. Reprinted with permission from ref 70. Copyright 2020 American Chemical Society.

The induction period indicated that the active form of the catalyst has to be formed. Presumably because the Rh/Co_3O_4 during the isolation process undergo partial deactivating oxidation. Therefore, Rh^0 NPs should be reformed during the AB dehydrogenation catalysis. The sigmoidal H_2 evolution kinetics data was used to fit a two-step mechanism consisting in a slow and continuous nucleation step (rate constant k_1) followed by an autocatalytic surface growth (rate constant k_2), as schematized Figure 1, right. The large value of the k_2/k_1 ratio *ca* 10^4 indicates the kinetically controlled formation of Rh(0) nanoparticles. This suggests also that the presumed "initial formation" of the catalyst is also not complete, and somewhat lack mastering. Like for ceria support, above-discussed, the high catalytic activity of Rh/Co_3O_4 nanoparticles in hydrolysis of AB was presumably attributed to the reducible nature of the support cobalt oxide.

The group of Fan reported the full elaboration of nanocatalysts comprised of Rh ultra-small nanoparticles (*ca.* 1.6 nm average size) anchored on nitrogen *N*-doped carbon nanotubes charged with 20 nm size Ni nanoparticles (Ni@NCNTs). These were fabricated by adsorption of Rh^{3+} ions from EtOH solution, followed by mild thermal treatment (vacuum, 60 °C, 8 h). Ni@NCNTs were synthesized by pyrolysis of D-glucosamine hydrochloride, melamine and $Ni(NO_3)_2.6H_2O$, uniformly grinded and heated at 800 °C for 2 h under Ar gas (Figure 2). Rh/Ni@NCNTs displayed a catalytic activity toward AB hydrolysis with a TOF = 959 min^{-1}, while Ni@NCNTs support alone has a negligible effect. Reusing of Rh/Ni@NCNTs was achieved in the hydrolysis of AB, in which fresh AB was subsequently added to the catalyst system and the next run was started. The system could be reused for nine successive runs without loss of AB conversion.

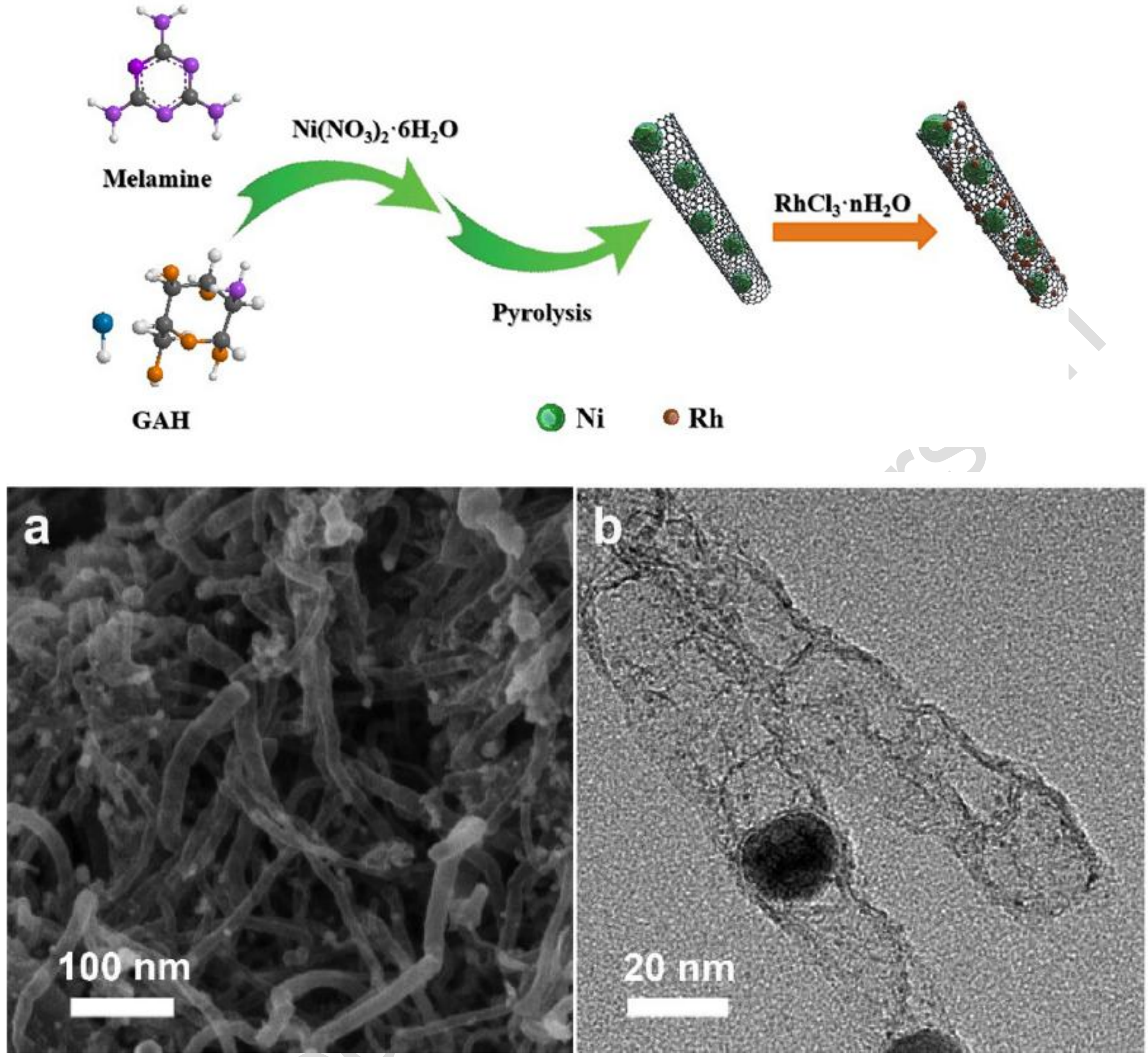

Figure 2. Top: Procedure for preparing Rh/Ni@NCNTs; Bottom: (a) SEM and (b) TEM imaging of Rh/Ni@NCNTs. Reprinted with permission from ref 69. Copyright 2019 Elsevier Ltd.

Other noticeable recent directions of researches concerned the synthetic modification achieved using various carbon-based supports. The synthesis of ultrafine rhodium nanoparticle (0.8 ± 0.4 nm) on carbon powder (Vulcan XC-72R, VC) Rh/VC was achieved from the reduction of Rh^{3+} ions absorbed on the carbon support via solution-dispersion method.[71] After solvent evaporation, the sample was annealed 2 h at 300 °C for pyrolysis of the $RhCl_3$ hydrate adsorbed on the carbon, forming an highly dispersed precursor material of rhodium-oxide type RhOx/C. Nanoparticles formation was achieved via *in situ* reduction of this precursor material in an electrolytic hydrogen-evolution process using ultra-pure water. While the carbon matrix alone displays negligible activity for AB hydrolysis, *in situ* formed Rh/C exhibits a TOF = 1246 min^{-1} at 25 °C. TOF values decreased with increasing reusing runs (*ca*. –5% each run). The Rh/C catalyst preserves a TOF of 762 min^{-1} in the 8th run, retaining 61.2% of its initial activity for AB hydrolysis. The detailed catalyst characterization after eight recycling showed that both dispersion and size of the Rh nanoparticles is unchanged, suggesting that decrease in catalytic activity along reusing processes is presumably due to the increasing concentration of metaborate waste.

With the view to keep a control on the metal nanoparticle size upon deposition on the support, sodium citrate was proposed as a transient nanoparticles stabilizing agent to be mixed with Rh^{3+} and carbon (Vulcan XC-72R) afterwards mildly reduced by $NaBH_4$ aqueous solution at 5 °C for 8 h. The Rh/VC was washed in water/EtOH cycles to remove the weakly bound sodium citrate agent.[72] As a result, rhodium nanoparticles were obtained with a particle size ranging from 2.4 to 6.7 nm (mean value of 4.1 nm), while Rh/C samples in the absence of sodium citrate exhibited a particle size ranging from 3 to 16 nm (mean value of 8.2 nm). In the catalytic dehydrogenation of AB, a TOF = 336 min^{-1} was achieved for the better dispersed nanoparticles *vs* a value of TOF = 134 min^{-1} in the systems lacking the control of sodium citrate. The most active Rh/C catalyst preserves about 50% of the initial TOF value in the fifth cycle, while its stability is limited with a growth of nanoparticle size that was observed along reusing.

In the search for developing new supports for nanoparticle catalysts from abundant and inexpensive compounds, Fan group proposed graphitic carbon nitride (g-C_3N_4) prepared through the pyrolysis of urea. This latter was treated at 500 °C for 4 h in air at ambient pressure.[73] Carbon and nitrogen were the main constituent elements (C:N molar ratio 0.78).

XRD pattern of this material showed a strong sharp diffraction peak at 2θ = 27.4° characteristic of the (002) crystal plane of g-C_3N_4 stating that interplanar stacking of conjugated aromatic structure from urea polymerization takes place. The as-prepared g-C_3N_4 was dispersed in water and impregnated with a water solution of $RhCl_3$ at 25 °C. A concomitant *in situ* synthesis of Rh/g-C_3N_4 nanoparticle materials and hydrolysis of AB for hydrogen production is then achieved. Upon the injection of AB aqueous solution, the volume of H_2 production was monitored. The Rh/g-C_3N_4 catalyst exhibited a TOF = 969 min^{-1}. Recycling of Rh/g-C_3N_4 for hydrolysis of AB was achieved by centrifugation and isolation of the solid catalyst that was washed, weighed, and re-dispersed in aqueous solution before the next run of fresh AB hydrolysis. Four recycling runs were achieved. A gradual decrease of activity (4th run TOF = 428 min^{-1}) attributed to Rh leaching (6 %) and loss of material in recycling process was observed. The size of Rh NPs, initially *ca* 3.0 nm, increases to an average size of 6.0 nm after the 4th run.

The same group has used similar procedures to develop a one-pot synthesis of Rh/(N,P)-C nanoparticle catalyst supported on (N,P)-doped porous carbon. Such catalyst were formed by pyrolysis of adenosine triphosphate considered as a low-cost and readily available resource.[74] A pore forming effect was observed depending on the temperature of calcination. Material exhibiting a surface area value of $S_{BET} = 154\ m^2\ g^{-1}$ and an average pore diameter of 6.3 nm was obtained at 800 °C (Rh/(N,P)-C_{800}). The catalytic hydrolysis of AB toward H_2 production with Rh/(N,P)-C_{800} exhibited a TOF = 566 min^{-1}. This catalyst retains 63% of its initial catalytic activity after the 8th catalytic run, while the original nanoparticles of 2.3 ± 0.4 nm size gathered to ten to several dozen nm size aggregates, reducing thus its effective active surface. A similar carbon-doping strategy allowed the production of ultrafine Rh nanoparticles sizing 2.2 ± 1.5 nm in diameter,[75] which were dispersed onto porous phosphorus-doped carbon supports. This supports were prepared by pyrolysing hyper-cross-linked networks based on triphenylphosphine and benzene copolymerization.[76] The resulting material, Rh/PPC (3.1 wt%) is characterized by $S_{BET} = 300\ m^2\ g^{-1}$, an average pore diameter of 4.0 nm, and achieved a better activity in AB hydrolysis than the Rh/(N,P)-C_x systems with a TOF = 806 min^{-1} at RT. Rh/PPC showed a recyclability (from isolation/washing process) for four cycles, with the growth of Rh nanoparticles (up to 3.2 nm) presumably causing a gradual loss of activity.

Alternative carbon-based supports appeared with the synthesis of Rh nanoparticles immobilized on nanodiamond (Rh/ND). Such material used for AB hydrolysis to produce H_2 exhibit a TOF = 729 min^{-1} at 25 °C.[59] FTIR spectra of ND evidenced surface carbonyl and hydroxyl groups presumably assisting the dispersion of Rh nanoparticles sizing 3.0 ± 1.5 nm, in a final catalytic materials of $S_{BET} = 300\ m^2\ g^{-1}$. Recycling experiments, after four runs conserved *ca* 42% of the initial catalytic activity, while the size of nanoparticles increased up to 4.0 nm. In this approach, the specific properties of ND (thermal and chemical inertness, rigidity, conductivity, catalytic activity in oxidation, *etc.*)[77] arguably remains to be further exploited.

While the intrinsic activity of rhodium nanoparticles for AB dehydrogenation is very high (probably the highest for transition metals to date), methods for their dispersion below 1.0 nm size stable nanocatalysts (approaching molecular cluster dimension), able to chemically interact with a valuable support (CeO_2 or modified-carbon) are essential for the best results. However, looking for a mainstream utilization of hydrogen energy, it seems that the rarity and high price for rhodium is currently a major obstacle to the development of something more than valuable models.

3.2. Advances in palladium-based and alloys nanoparticle catalysts

The market price for palladium in June 2020 was 62,000 USD kg^{-1}, compared to 20,000 USD kg^{-1} in 2016 (+200%), and 21,000 USD kg^{-1} in 2012 (–5%).[65]

Palladium was early on reported as useful for dehydrogenation of neat (*t*-butyl)methylamine borane using 10% Pd on charcoal under argon at 120 °C.[24] The standards for highest activity in hydrolytic dehydrogenation of AB with this transition metal was established with TOF values around 250 min^{-1},[78,15,18] about one order of magnitude lower than rhodium standard. Nevertheless, relevant research orientations have been pursued which partially compensate this apparent lack of reactivity: *i*) progress was achieved in the synthesis of recyclable systems, especially based on supports magnetically recoverable, *ii*) active metal composites or alloys based on palladium mixed with low-cost metals were developed, and *iii*) tandem reactions after AB dehydrogenation were achieved taking benefit of the versatile reactivity of palladium for hydrogenation.

Pd(0) nanoparticles supported on silica-coated cobalt ferrite, Pd/SiO_2–$CoFe_2O_4$ (Pd 1.98 wt%) were generated *in situ* during the hydrolysis of AB. As previously described for rhodium, Pd^{2+} ions could be impregnated on SiO_2–$CoFe_2O_4$ from an aqueous solution of Pd(II) nitrate and then reduced by AB at RT.[78] The size of SiO_2–$CoFe_2O_4$ nanoparticle supports was 13.0 ± 2.0 nm and of 6.0 ± 1.0 nm for Pd nanoparticles. Hydrogen production from the hydrolysis of AB was achieved with a TOF = 254 min^{-1} at 25 °C. Note that, in the presence of the SiO_2–$CoFe_2O_4$ support only, hydrolysis of AB does not occur under these conditions. The catalyst was isolated using a permanent magnet (Figure 3, left), and washed with water before every run in the recycling. Remarkably, the recycling tests indicated a TOF = 198 min^{-1} in the 10th use, retaining 78% of its initial activity.

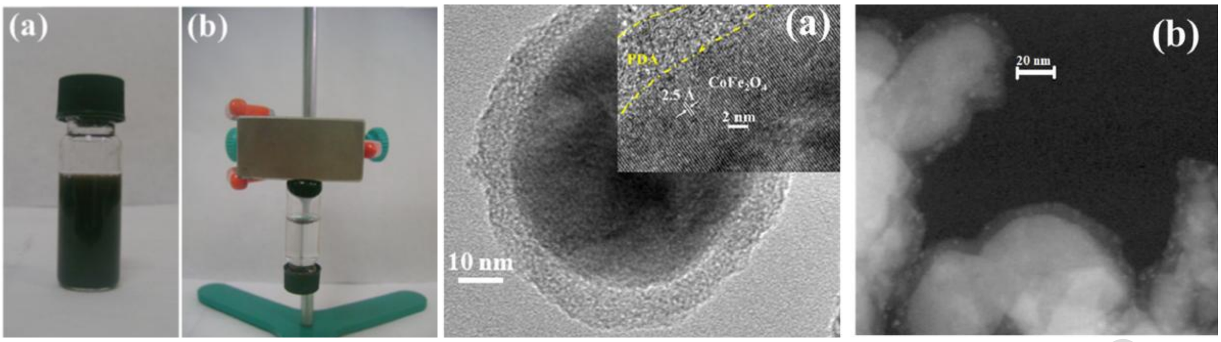

Figure 3. Left: Pictures of (a) dispersed catalyst in water; (b) isolated catalyst using a permanent magnet; Right: HAADF-STEM images of $Pd^0/PDA–CoFe_2O_4$ (1.08 wt% Pd) showing (a) dopamine layer and lattice fringes (inset), (b) Palladium NPs on the dopamine layer (right). Reprinted with permission from ref 78 and 39. Copyright 2013 and 2017 Elsevier B.V.

Pd(0) nanoparticles directly supported on cobalt ferrite, $Pd/CoFe_2O_4$, achieved a TOF = 290 min^{-1} in hydrolysis of AB at RT, but their low stability did not preserved this activity upon reuse.[39] Polydopamine (PDA) coated cobalt ferrite supports improved the stability of the catalyst. By pH-induced self-polymerization of dopamine hydrochloride at RT, the thickness of PDA could be tuned and Pd nanoparticles (average size 1.4 ± 0.3 nm) dispersed on a polydopamine layer of 8.6 ± 1.0 nm thickness on the surface of cobalt ferrite nanopowders (30 nm). $Pd/PDA–CoFe_2O_4$ (Figure 3, right, Pd 1.08 wt%) achieved a TOF = 175 min^{-1} at 25 °C that was preserved in the subsequent recycling up to 10th run. Magnetic chitosan (CS-Fe_2O_4) support was also synthesized via co-precipitation of the biopolymer and $FeCl_2/FeCl_3$ under strongly basic conditions.[79] This support was used to anchor Pd nanoparticles by chemical reduction of $PdCl_2$ with $NaBH_4$. The resulting catalyst achieved the hydrolysis of AB with a TOF = 15 min^{-1} at 30 °C, which was conserved other eight runs. Comparable activity and recycling performances had been reported for non-magnetic systems with palladium nanoparticles supported on chemically derived graphene.[57]

Beside the high activity for AB hydrolysis of Pd–Rh-PVP-protected nanoparticles (TOF = 1300 min^{-1}),[45] that is presumably attributable mostly to the presence of rhodium, catalytically active multimetallic composites with palladium allied to low-cost metals are known,[15] such as Pd–Co core-shell catalysts,[80] or Pd–Ni alloy catalysts.[81] Recent advances related to the formation of Pd–Ni catalysts reported by the group of Sun addressed a better control of the Pd–Ni catalyst structuring over 2D nitrogen-doped graphene (NG).[82] They achieved the assembly of a monolayer array of nitrogen-doped graphene and nanoparticles with the subsequent transfer of the assembled layers onto a solid substrate for on/off facile catalysis (Figure 4, top).

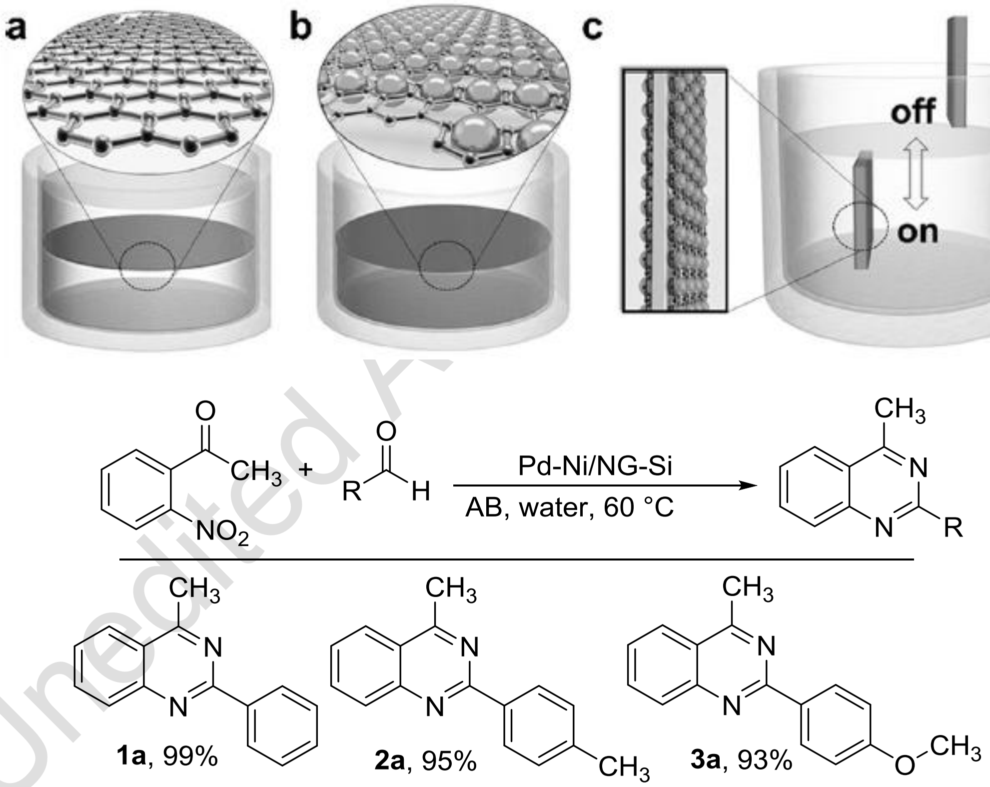

Figure 4. Top: a-b) Illustration of the interface assembly of monolayer NG and NPs/NG. c) Assembled NPs/NG on both sides of Si support for catalysis with "on/off" insertion/pulling out from the solution to start/stop the reaction. Bottom: Condensation of 2-nitroacetophenone with aldehydes; Conditions: 2-nitroacetophenone (1 mmol), aldehyde (1.2 mmol), Pd-Ni/NG-Si (0.016 mol%), water (20 mL) and AB (3

mmol), 60 °C, 8 h. Reproduced with permission from ref 82. Copyright 2018 Wiley- VCH Verlag GmbH & Co. KGaA, Weinheim.

By depositing 3 nm size alloy nanoparticles $Pd_{70}Ni_{30}$ on silicon wafer,[83] these authors showed that monolayers of Pd–Ni-NG-Si exhibited an efficiency for AB hydrolysis reaching a TOF = 81.6 min^{-1}. Importantly, such material further allowed hydrogenation plus condensation of *o*-nitroacetophenone and benzaldehydes leading to one-pot synthesis of quinazolines in water (Figure 4, bottom), the AB hydrolysis providing H_2 and NH_3.

Other Pd–Ni bimetallic supported systems have been described with contrasted performances. Supported on rGO, the optimized nanoparticle composite catalyst $Pd_{80}Ni_{20}$–CeO_2/rGO, as bimetallic alloy with an average size of nanoparticles of 3.4 nm ± 0.4 nm and a ceria content of 13.9 mol%, showed an activity for H_2 evolution from AB hydrolysis with a TOF = 30.5 min^{-1} that remained unchanged within five cycling runs.[84]

Pure Pd/MCN (2.7 ± 0.4 nm) and $Pd_{74}Ni_{26}$ /MCN (2.4 ± 0.5 nm) nanocatalysts (with 3 wt% metal) supported on MCN (Figure 5) were found both active in AB hydrolysis with TOF = 125 min^{-1} and 247 min^{-1}, respectively.[85] TOF values of $Pd_{74}Co_{26}$/MCN (208 min^{-1}), $Pd_{68}Fe_{32}$/MCN (80 min^{-1}) and $Pd_{67}Cu_{33}$/MCN (63 min^{-1}) were also reported. Interestingly, $Pd_{74}Ni_{26}$/MCN nanocatalyst provided an 8778 TTO over 10 h before deactivation at RT, while monometallic Ni/MCN exhibited only a weak catalytic activity (only 2.2 equiv. H_2 released per AB in 50 min).

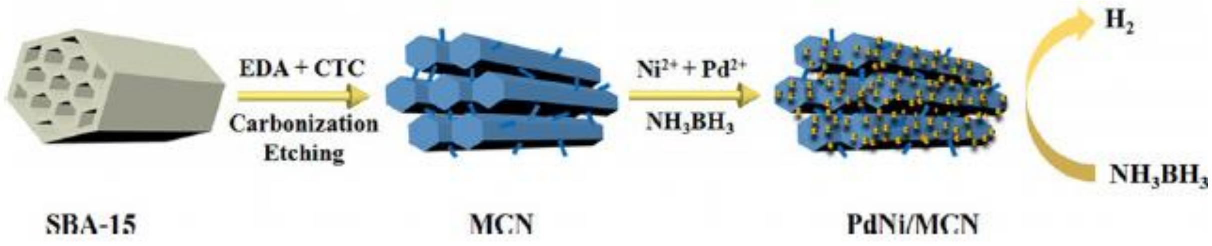

Figure 5. MCN and Pd–Ni synthesis from mesoporous SBA-15 as a sacrificial template. Reprinted with permission from ref 85. Copyright 2018 Wiley-VCH Verlag GmbH & Co. KGaA, Weinheim.

In addition to this dispersion of small nanoparticles into a mesoporous structure, comparative experiments with various supports (SBA-15, *etc*.) suggested that the better activity of $Pd_{74}Ni_{26}$/MCN resulted from a strong chemical interaction between Pd–M alloys and the MCN matrix rich in nitrogen.[85]

Another valuable metal pairing that has shown recent progress concerned the use of Pd–Ag bimetallic nanoparticles.[86,87] Pd–Ag alloy nanoparticles were synthesized using an organic-phase surfactant-assisted protocol for co-reduction of silver(I) acetate and palladium(II) acetylacetonate in the presence of oleylamine, oleic acid and 1-octadecene at 180 °C.[88] The as-obtained alloyed nanoparticles ($Pd_{75}Ag_{25}$, $Pd_{58}Ag_{42}$, $Pd_{48}Ag_{52}$, and $Pd_{40}Ag_{60}$) were assembled on graphitic carbon nitride (g-C_3N_4) or rGO by self-assembly under sonication during 2 h in hexane/ethanol mixture. Regardless of the composition, the alloyed nanoparticles were described as being spherical with a size distribution of 2.7 ± 0.3 nm. The catalytic activity towards AB hydrolysis reached a TOF = 94.2 min^{-1} using $Pd_{58}Ag_{42}$@g-C_3N_4 after a treatment with acetic acid for surfactant removal. The hydrolytic dehydrogenation of AB was performed under dark, sunlight, and halogen projector lamp (500 W, 50 Hz) conditions with the catalyst. Stoichiometric H_2 production was completed in 15 and 8 min for the catalytic hydrolysis reactions performed under dark and sunlight conditions, respectively, while the use of the halogen projector did not much affect the catalytic activity of $Pd_{58}Ag_{42}$@g-C_3N_4. The catalytic activity improvement using g-C_3N_4 as a support material under sunlight was attributed to the formation of a Mott–Schottky-type catalyst with an electronic interaction between the semiconductor support g-C_3N_4 and the Pd–Ag alloyed NPs (Figure 6). Upon irradiation, the semiconductor support generates excited electron–hole pairs;

the electrons flowed through the metal–semiconductor interface to the metal providing the work function of the alloy that was between the valence and conduction bands of the mesoporous organic semiconductor. This results in an electron-rich metal surface with a higher catalytic activity toward the hydrolytic dehydrogenation of AB. The reusability test showed that the $Pd_{58}Ag_{42}@g\text{-}C_3N_4$ catalyst preserved *ca* 70% of its initial activity after the fifth run.

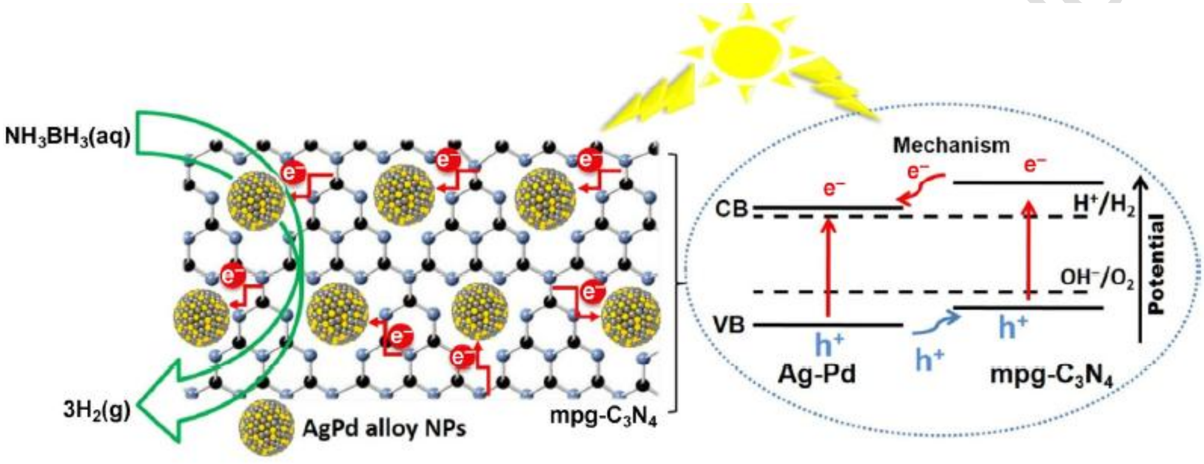

Figure 6. Mechanistic view of the activity of $Pd_{58}Ag_{42}@g\text{-}C_3N_4$for AB hydrolysis under sunlight. Reprinted with permission from ref 88. Copyright 2016 Tsinghua University Press and Springer-Verlag Berlin Heidelberg.

Activated carbon supported trimetallic $Pd_{60}Co_{20}Ag_{20}$ nanoparticles showed superior efficiency in hydrolysis of AB at 25 °C (TOF = 110 min^{-1}) over comparable monometallic Pd-based and bimetallic Pd–Co nanoparticles that showed an activity one order of magnitude lower.[89] The catalyst was prepared at RT using commercial activated carbon dispersed in an aqueous solution containing K_2PdCl_4, $CoCl_2.6H_2O$ and $AgNO_3$. $NaBH_4$ was used for reduction of the mixture, which was filtrated and the resulting solid dried in vacuum oven at 85 °C. For the $Pd_{60}Co_{20}Ag_{20}/C^*$ catalyst an average particle size of *ca* 7 nm was determined. While their exact structure is unclear, XPS data indicated Pd(0) and Ag(0) as major surface component and cobalt oxide Co_3O_4 in the core. Along eleven cycling runs for AB hydrolysis, a slow decrease of activity is noted until the 7th run showing a net degradation.

Palladium-based nanoparticle catalysts have been used for tandem reactions, in which hydrogen evolution from AB (or derivatives) solvolysis provides the source of hydrogen necessary for further organic synthesis.[90,91] Thus, colloidal $Pd_{70}Co_{30}$ alloy nanoparticles have been assembled on reduced graphene oxide (rGO) and used as catalysts in the reduction by AB of aromatic nitro, nitrile and carbonyl compounds into primary amines and alcohols.[90] To improve the process of aryl nitro compounds reduction, palladium can be dispersed into a mesoporous Cr(III)-based MOF MIL-101 via a double solvent approach (DSA)[92] followed by *in situ* reduction by NH_3BH_3 to afford 3 nm Pd nanoparticles catalyst confined inside the MIL-101 pores.[91] TOF value for the hydrogenation of nitrobenzene was measured at 97 min^{-1}.

The use of palladium catalysts in tandem reactions from AB hydrogen evolution shifted to the elaboration of more advanced systems (photocatalytic, microflow compatible, *etc.*) in which sophisticated porous supports were used. In these cases, the hydrogenation of triple and double bonds of aromatic substrates was targeted.[93, 94, 95, 96, 97, 98, 99, 100] The hybridization of MOFs and COFs material for supporting palladium nanoparticles has been achieved in view of combining photocatalytic activity from MOF on one hand and open accessible structure and dispersed strong anchoring N-sites from COF on the other hand.[93] Titanium-based MOF NH_2-MIL-125(Ti) (abbreviated TiATA) was chosen and combined with a 2D imine-based COF LZU1 to form a core-shell association. Pd^{2+} was incorporated into TiATA@LZU1 via treatment of TiATA@LZU1 with palladium acetate. Pd nanoparticles with an average diameter of 2.2 nm ± 0.5 nm attained a 3.6 wt% Pd loading. By immobilizing Pd/TiATA@LZU1 on the inner wall of a dual chamber microreactor, tandem photocatalytic dehydrogenation of AB and hydrogenation of olefins was achieved (Figure 7). *In situ* generated H_2 gas in the bottom chamber instantly passed through gas-permeable membrane to the upper chamber for consumption by hydrogenation. This process in dual-chamber microreactor prevented the product contamination and avoided the mismatching problem of different reaction conditions. After first run reaction, the steady performance of Pd/TiATA@LZU1 for hydrolytic dehydrogenation of AB corresponded to a TOF = 147 min^{-1} that could be conserved over six cycling runs.[93] Complete evolution of H_2 (H_2/AB molar ratio = 3.0) was achieved in 55 min in the dark, while visible light promotes the reaction to be completed in 8 min –note that TiATA@LZU1 support is inactive in itself–. In the tandem reaction, full conversion of styrene to ethylbenzene (in ethanol, >99% selectivity) was achieved in 15 min under visible light irradiation, *vs* 38% styrene conversion under the same conditions in the dark. The hydrogenation over Pd/TiATA@LZU1 can be expanded to both allyl benzene and *trans*-ß-methyl styrene to propyl benzene (>99% selectivity) within 15 min. Hydrogenation of aliphatic olefins needed longer time compared with aromatic ones, but cyclohexene is converted to cyclohexane in 90 min with a conversion of 91% (>99% selectivity). Interestingly, a complete selective conversion of 5-hexen-2-one to 2-hexanone was realized in 45 min, preserving the carbonyl group.[93]

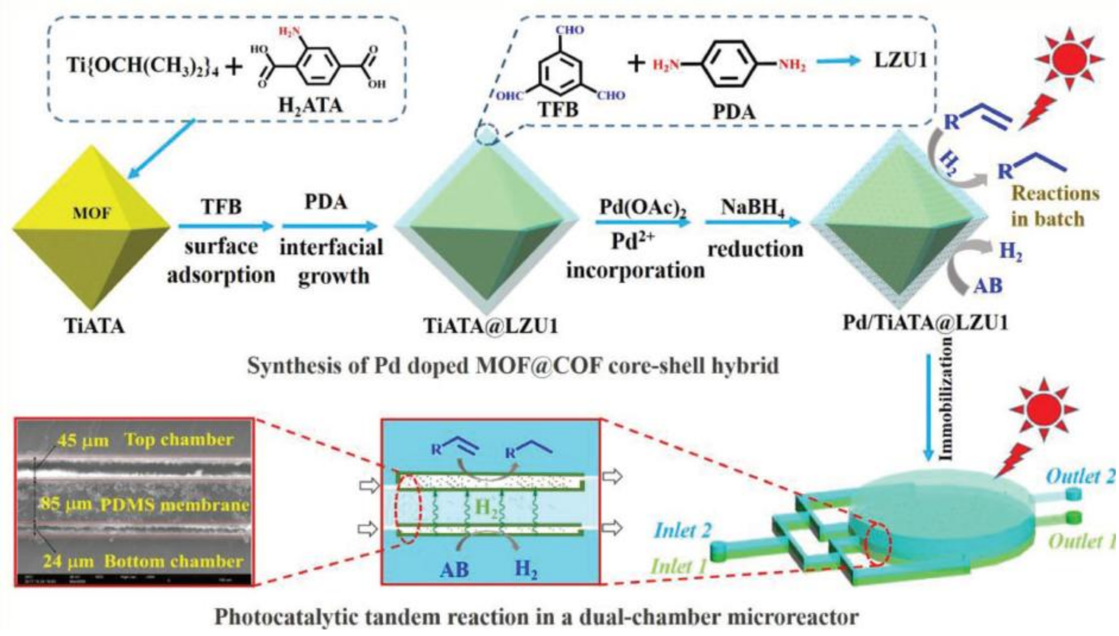

Figure 7. Schematic scope of the preparation of Pd doped TiATA@LZU1 core–shell and their photocatalytic applications in batch and dual-chamber microreactor. Reprinted with permission from ref 93. Copyright 2018 WILEY-VCH Verlag GmbH & Co. KGaA, Weinheim.

Palladium nanocomposites were also investigated from the MOF UiO-66(Hf) possessing Brönsted acidic sites on secondary building units. Both Pd@UiO-66(Hf) core–shell and Pd/UiO-66(Hf) supported catalysts were synthesized (Figure 8, top).[94] These composites both catalyzed dehydrogenation of AB in organic solvent (1,4-dioxane, DMF, hexane, CH_3CN, *etc.*). The "core–shell" catalyst in dioxane exhibited the best activity (TOF = 3.9 min^{-1}) towards H_2 production from AB, owing to greater contact interface between Pd and MOF (Pd particle size being 7.6 ± 0.5 nm for core–shell structure and 7.6 ± 0.7 nm for supported structure, for 5.2 and 4.7 Pd wt%, respectively). Further, tandem phenylacetylene selective hydrogenation to styrene (with >99% selectivity) with AB was achieved using Pd@UiO-66(Hf) (Figure 8, bottom).

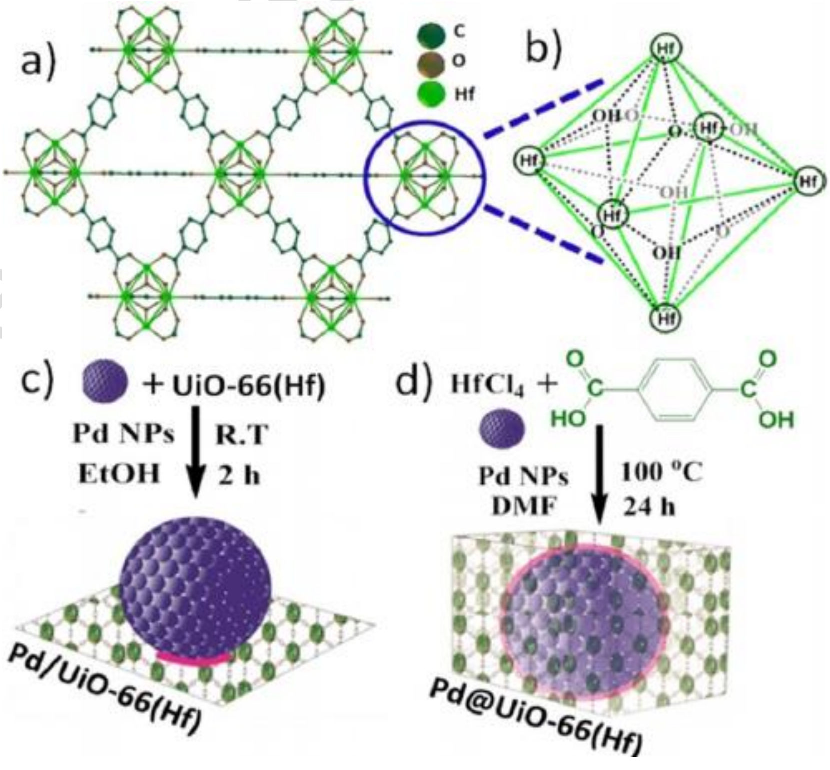

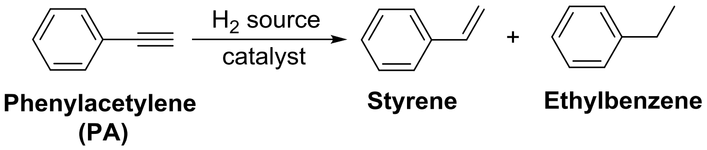

Catalyst	H_2 Source	Conv. (%) of PA	Selectivity (%)	
			Styrene	Ethylbenzene
Pd@UiO-66(Hf)	$H_3N{\rightarrow}BH_3$	100	93.2	6.7
Pd@UiO-66(Hf)	H_2, 1 bar	100	0.1	99.9

Figure 8. Top: a) UiO-66(Hf) framework. b) Secondary building unit (SBU) of UiO-66(Hf) with Brönsted acidic (–OH) sites. c) Representation of the Pd/UIO-66(Hf) support. d) Pd@UiO-66(Hf) core-shell materials and their synthetic protocols. The pink trace indicates that contact interface (in 2D) between Pd and UiO-66(Hf). Core-shell structure exhibits greater interface. Bottom: e) Hydrogenation of phenylacetylene (PA) and effect of H_2 source on products selectivity. Reprinted and reproduced with permission from ref 94 and 95. Copyright 2018 and 2020 Wiley- VCH Verlag GmbH & Co. KGaA, Weinheim.

The selectivity of this reaction using AB is notable since, in contrast, phenylacetylene hydrogenation with 1 bar molecular H_2 under identical conditions yielded fully hydrogenated ethyl benzene.[94] This highlights the singularity of AB as a transfer hydrogenation agent. Compared to hydrolysis and methanolysis, H_2 release from AB in organic medium opens up further possibility for regeneration of the starting material from BNHx polymers byproducts.

Tandem catalytic dehydrogenation of AB and hydrogenation of phenylacetylene was also achieved with 100% conversion of phenylacetylene and a selectivity of 96% in styrene from a MOF-based composite CeO_2 nanotube–Pd@MIL-53(Al). This material is a sandwich-structured catalyst in which the MIL-53(Al) porous shell stabilized the Pd nanoparticles (S_{BET} = 354.2 m^2 g^{-1}, ill-defined Pd nanoparticles).[95] A TOF values equaled to 16.2 min^{-1} using CeO_2 nanotube–Pd@MIL-53(Al) for the alkyne hydrogenation, reduced at 50% of its activity at the 5th cycling run.

The use of palladium-containing bimetallic nanoparticles in such tandem processes is also a recent achievement. A synthesis of core-shell $Au_{50}Pd_{50}@CeO_2$ composite with an external shell of ceria was achieved by involving an autoredox reaction process. In this case, the easier reduction ability of $HAuBr_4$ over K_2PdBr_4 was taken into benefit in the presence of PVP and KBr (Figure 9).[96] The Au core was proposed to form first followed by Pd overgrowth. Then CeO_2 auto-assembly encapsulates the bimetallic core. The particle size distribution implies an average particle size of 33 nm with uniform distribution of elemental Au, Pd, Ce and O. Au and Pd elements are mainly dispersed in the core which is surrounded by outside Ce and O elements (Figure 9).[96] Etching results suggested that Pd was distributed mostly between the Au core and CeO_2 shell. With different amounts of Au and Pd precursors added, the composition of Au:Pd was tuned from 1:2 to 2:1. The 1:1 $Au_{50}Pd_{50}@CeO_2$ (23.8 wt% Au, 6.3 wt% Pd) material showed activity to catalyze the selective hydrogenation of phenylacetylene into styrene using AB as the hydrogen source. A conversion of phenylacetylene reaching 100% at 28 min and a 94% yield of styrene was reported that changes to 92 % conversion and 93% yield of styrene over four cycling runs, while the morphology of the catalyst remains unchanged, suggesting a fair stability.

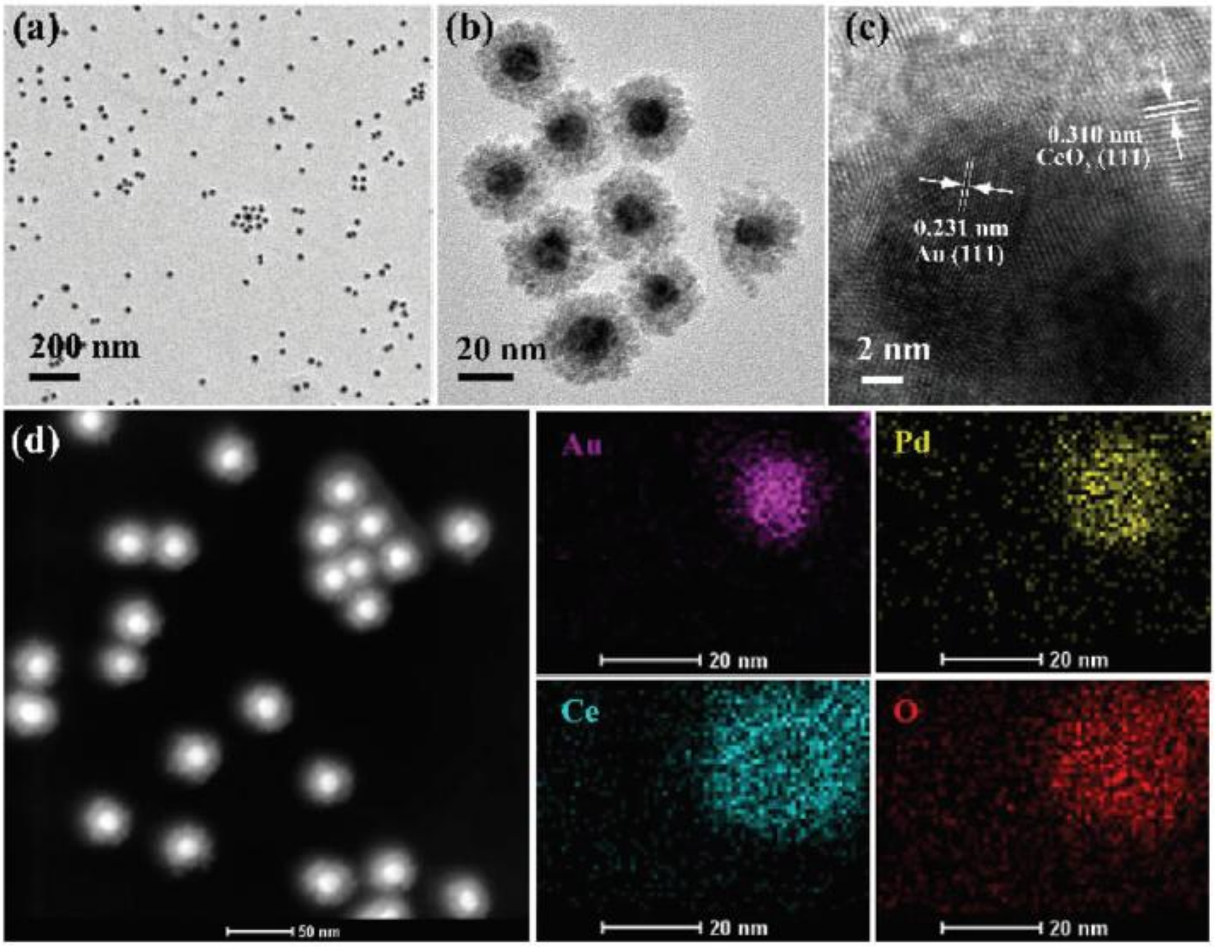

Figure 9. (a) TEM image, (b) enlarged TEM image, (c) high-magnification TEM image, and (d) STEM image and STEM-EDX mapping analysis of gold, palladium, cerium, and oxygen of Au–Pd@CeO_2-1. Reprinted with permission from ref 96. Copyright 2019 Royal Society of Chemistry.

Bimetallic core-shell silver-palladium composite nanoparticles have also been recently designed, in which a plasmonic silver nanocube core acts as a light absorber while an ultrathin palladium shell as the actively catalytic external layer for AB hydrolysis (Figure 10).[97] The Ag nanocubes core with an average edge length of 45 nm were prepared as seeds and the Pd shells were coated on them in the presence of polyvinylpyrrolidone by reducing Na_2PdCl_4 with ascorbic acid in alkaline condition (NaOH, pH 12). During the synthesis, the light yellow color of Ag nanocubes solution gradually turns to brown when the Ag@Pd hybrid nanostructure formed. This change was monitored by UV−vis spectra (Figure 10a).

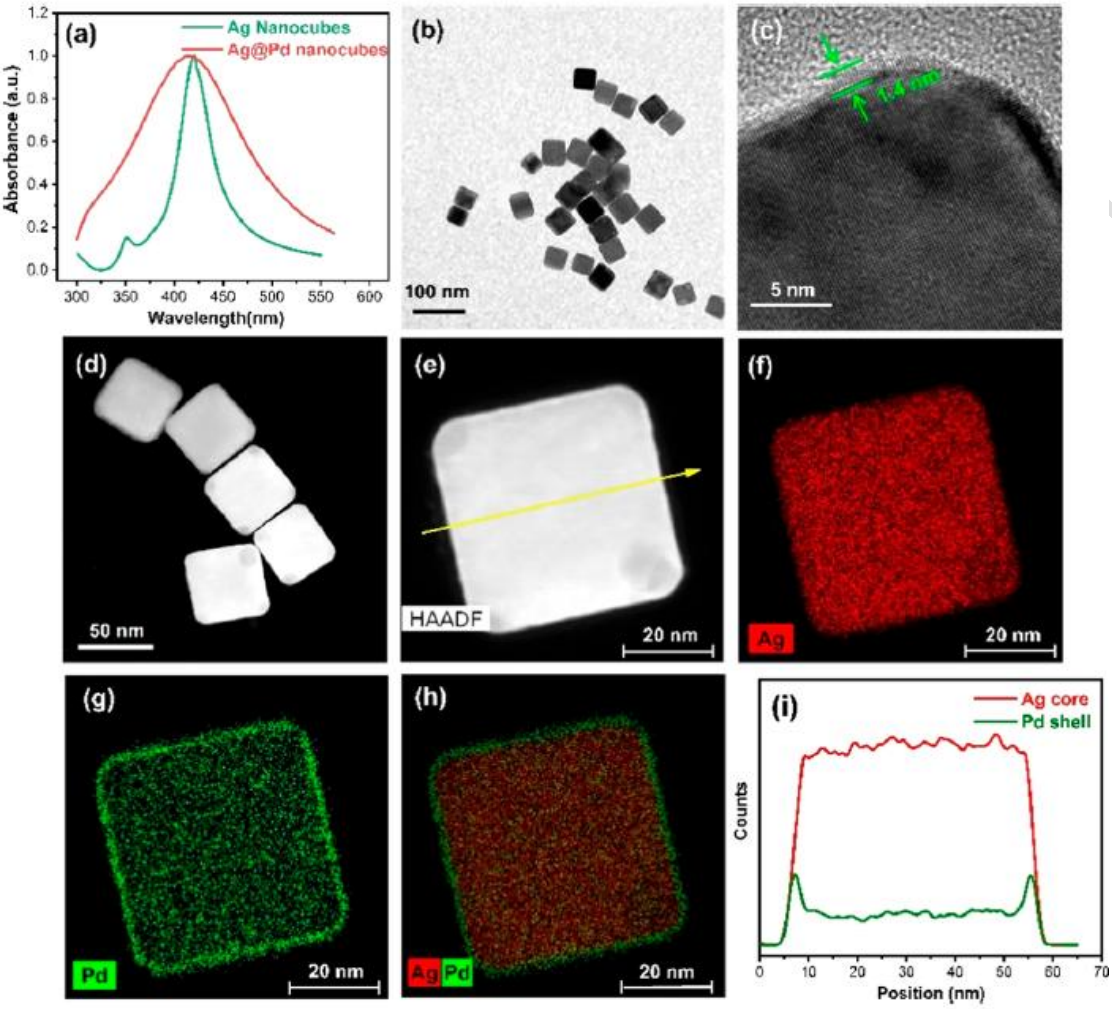

Figure 10. (a) Normalized UV−vis spectra of an aqueous solution of Ag and Ag@Pd nanocubes. (b) TEM image of an ensemble of the prepared Ag@Pd nanostructures. (c) HRTEM lattice fringe image of an Ag@Pd nanocube. (d) STEM-HAADF image of the prepared Ag@Pd core−shell nanocubes. (e) STEM-HAADF image of a representative Ag@Pd nanocube. STEM-EDS element map of Ag (f), Pd (g), and their overlay map (h). (i) EDS elemental scanning line profile along the yellow arrow line in panel e. Reprinted with permission from ref 97. Copyright 2020 American Chemical Society.

The Ag@Pd core-shell nanocubes with different Pd shell thicknesses (Figure 11, top) were prepared using a similar procedure at various Na_2PdCl_4 concentration. HRTEM indicated that the ultrathin Pd shell of *ca* 1.4 nm in thickness (epitaxially formed onto the Ag nanocube) corresponded to six atomic layers with lattice spacing of 0.23 nm. Under dark conditions, the Ag@Pd nanocubes exhibit a catalytic activity with a H_2 evolution rate of 0.11 mmol min^{-1}, similar to pure Pd analogues, and higher activity than naked Ag nanocubes (0.07 mmol min^{-1}).

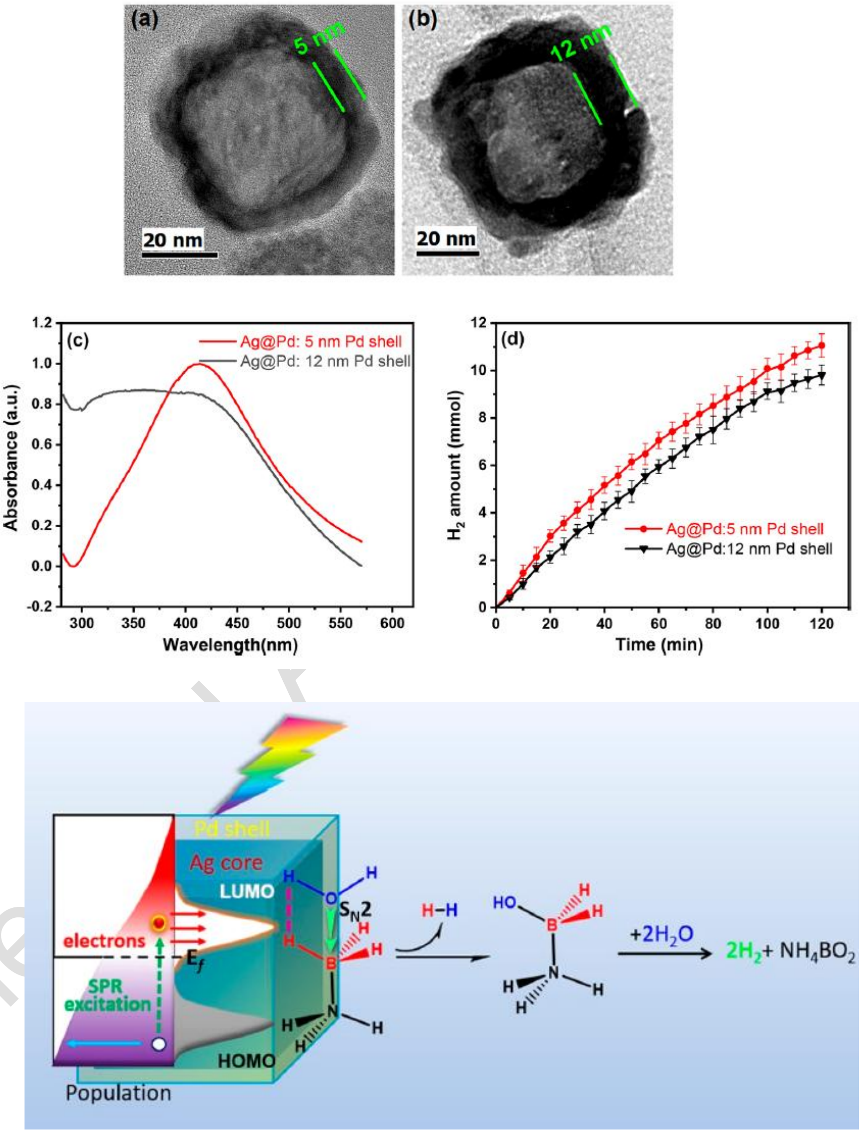

Figure 11. Top: Representative TEM images of Ag@Pd core−shell nanocubes with Pd shell of 5 (a) and 12 nm (b). The UV−vis spectra (c) and the H_2 evolution profile (d) of these two samples with different Pd shell thickness. Bottom: Proposed mechanism for the enhanced catalytic activity of Ag@Pd core−shell catalyst for

AB hydrolysis under light illumination. Reprinted with permission from ref 97. Copyright 2020 American Chemical Society.

Under light illumination, the Ag@Pd and Ag catalysts displayed enhanced activity, with a H_2 evolution rate of 0.21 mmol min^{-1} (+91%, for a TOF = 103 min^{-1}) and 0.09 mmol min^{-1} (+29%), respectively.[97] Conversely, pristine Pd nanocubes exhibited no improved activity for promoting H_2 evolution. Under light illumination, a "synergy" effect was thus evidenced between the plasmonic silver core and the catalytic palladium shell. The mechanistic assumptions (Figure 11, bottom) specified that core-shell Ag@Pd catalysts under light illumination have strong photon energy that dissipates into the Pd shell. This presumably leads to concentration of energetic charge carriers on the Pd shell with a strong heterogeneity of surface charge. This heterogeneity of charge distribution might favor the enhanced binding of AB through both hydrogen atoms of $-BH_3$ and $-NH_3$ groups. Similarly, water could also bind the Pd surface. Thus, plasmon-induced energetic electrons in the Pd shell may immediately transfer and accumulate to the lowest unoccupied molecular orbital (LUMO) of the Pd–AB association formed at surface, and further activates H_2O that can attack the weakened $-BH_3$ intermediate through a SN_2-type addition. The subsequent elimination reaction would result in production of H_2 and NH_3BH_2OH. Compared with that of 1.4 nm Pd-shelled nanoparticles, lower plasmon-driven H_2 evolution rate were found with Pd-shelled Ag@Pd nanocubes having 5 nm Pd (0.14 mmol min^{-1}) and 12 nm Pd (0.12 mmol min^{-1}), Figure 11, top.[97] When the thickness of the Pd shell reaches 12 nm, there is no distinct surface plasmon resonance (SPR) peak distinguishable in the visible region. The decreased catalytic performance with thickening the Pd shell was clearly attributable to the fade of plasmon effect from silver core when the palladium shell gets too thick to let the light go through. This demonstrates the fine synthetic control in these plasmon composites.

Palladium-based bimetallic nanoparticles were used in tandem AB dehydrogenation and dehydrohalogenation of mono- and polyhalogenated aromatics (PHAs).[98,99] These works established AB as a valuable alternative to the use of pressurized H_2 in the conversion of such persistent chemical pollutants that are generally difficult to degrade in the natural environment, and may accumulate to pass from one organism to another through the nutriment chain. $Pd_{70}Ni_{30}$ nanoparticles, supported on nitrogen-doped graphene, catalyzed the hydrodehalogenation of PHAs of mono- and dichloroarene type (Table 2).[98]

Table 2. Tandem AB dehydrogenation and mono- and polyhalogenated aromatics dehydrohalogenation

(1)[a]

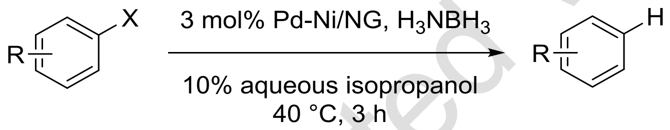

entry	ArX	yield[b]	entry	ArX	yield[b]	entry	ArX	yield[b]
1	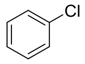	99[c]	2	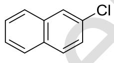	94[c]	3	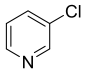	98[c]
4	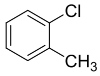	98[c]	5	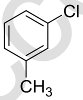	99[c]	6	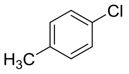	99[c]

[a] Conditions: halide (1 mmol), AB (2 mmol), 10% aqueous isopropanol (3.0 mL), NiPd/NG (3 mol%). [b] Yields for isolated product if not noted otherwise. [c] GC-MS yield.

(2)[a]

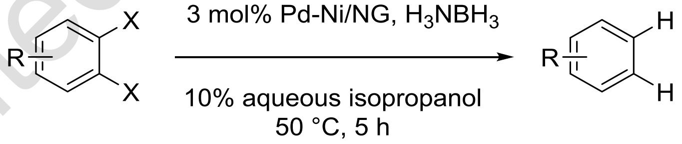

entry	ArX	yield[b]	entry	ArX	yield[b]	entry	ArX	yield[b]
1	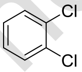	98[c]	2	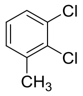	97[c]	3	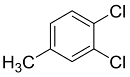	98[c]
4	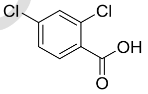	97	5	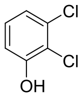	90	6	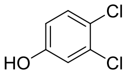	93
7	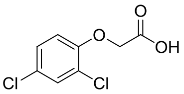	90	8	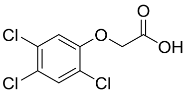	87	9	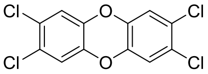	92[c,d]
10	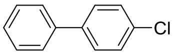	99[c]	11	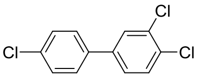	99[c]	12	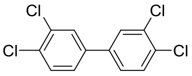	98[c]

13	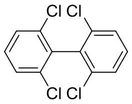	97[c,e]	14	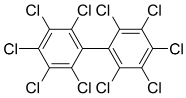	94[c,e,f]	15	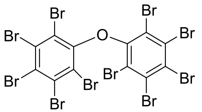	97[c,e]

[a] Conditions: halide (1 mmol), AB (3.0 equiv with respect to X content), 10% aqueous isopropanol (3.0 mL), NiPd/NG (3 mol%). [b] Yields for isolated product if not noted otherwise. [c] GC-MS yield. [d] 0.003 mmol (1 mg) of dioxin was used in the reaction. [e] Reaction run 12 h. [f] 0.04 mmol of decachlorobiphenyl.

These Pd–Ni/NG nanoparticles (3.0 ± 0.1 nm), deposited on nitrogen-doped graphene (NG) for preventing aggregation by pyridinic-N coordination, were found to be the most active among other bimetallic Pd–Co/NG, Pd–Fe/NG and bigger nanocomposites [Pd_XNi_y] also deposited over NG ($Pd_{100}Ni_0$/NG = 4.0 ± 0.2 nm; $Pd_{46}Ni_{54}$/NG = 3.4 ± 0.3 nm; $Pd_{33}Ni_{67}$/NG = 3.8 ± 0.2 nm). Pd–Ni/NG were prepared by mixing hexane dispersions of preformed nanoparticles (from reduction of $Pd^{II}(acac)_2$ and $Ni^{II}(acac)_2$ mixtures using borane-*tert*-butylamine in the presence of oleylamine and 1-octadecen) and NG in a 1:1 mass ratio. While the $Pd_{70}Ni_{30}$ nanoparticle intimate structure is not described, they were successfully used in a large range of hydrodehalogenation, the dehydrogenation of AB being the source of H_2 (Table 2). Notably, 0.35 M model solutions of mono- and polyhalogenated benzenes, dioxins, polychlorinated biphenyls, chloroaromatic constituents of the defoliant agent orange, and polybrominated diphenyl ethers were hydrodehalogenated in 3 to 12 h (Table 2).

Monodisperse bimetallic Pd–Au alloy nanoparticles,[101] loaded on a carbon support (Ketjen carbon), were also used for the catalytic study of AB dehydrogenation from methanolysis or hydrolysis.[99] A composition-dependent activity was observed – like for above-mentioned Pd–Ni nanocomposites[98]–, in which $Pd_{34}Au_{66}$/C was the most active for AB methanolysis with a TOF = 160 min^{-1} using a catalyst loading of 0.7 mol % total in metal (TOF = 122 min^{-1} at 0.5 mol% total metal, and 360 min^{-1} when normalized to Pd content only). Notably, the catalyst was used ten times for AB methanolysis dehydrogenation without apparent changes in catalyst morphology and structure (Figure 12). $Pd_{34}Au_{66}/C$ was active in the reduction of nitro groups to amines using AB source, as well as in the tandem dehydrogenation of AB and hydrodehalogenation of simple mono-, di- and trichlorinated aromatics.[99]

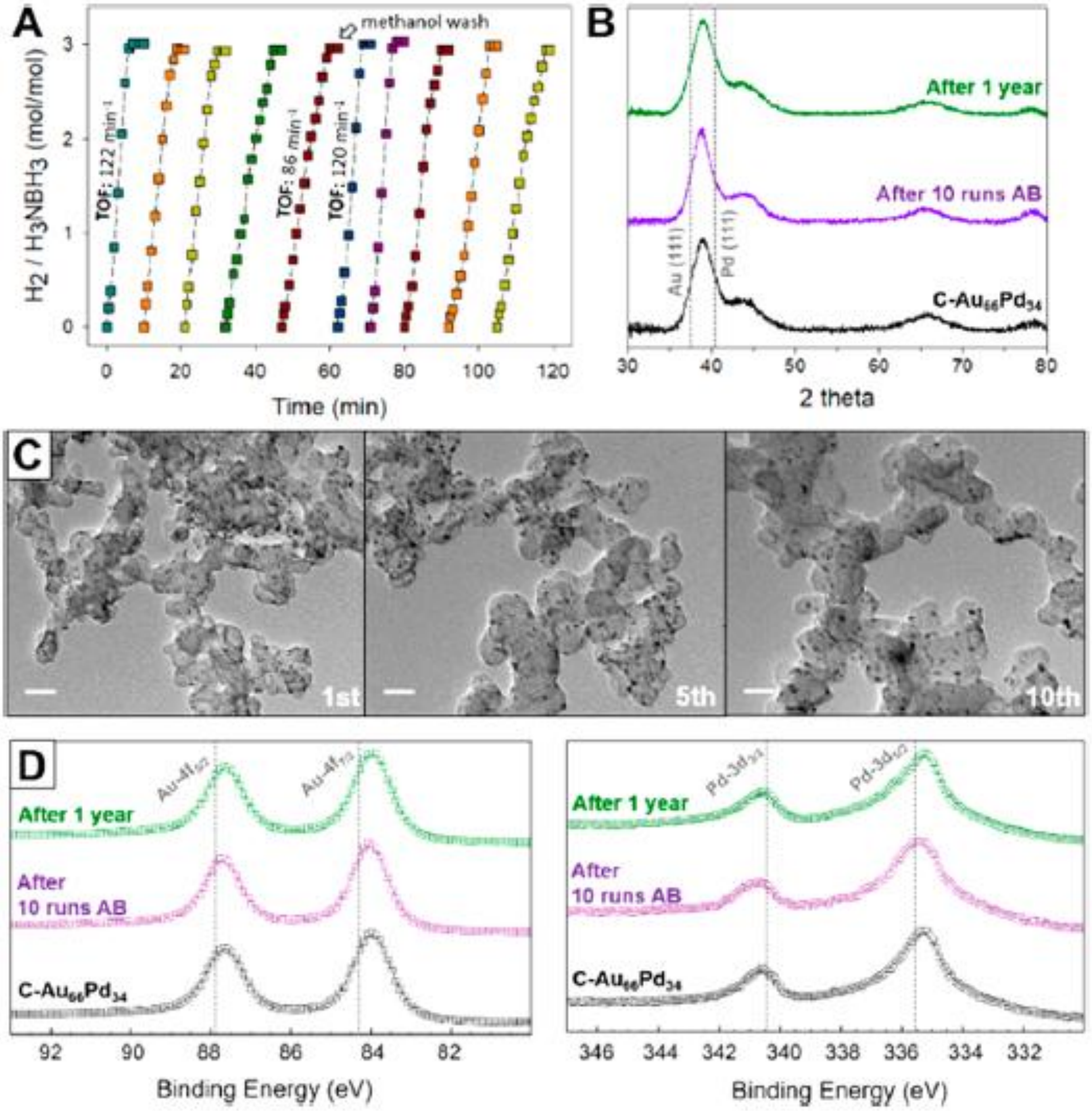

Figure 12. (A) Stability of $C-Au_{66}Pd_{34}$ for ten cycles of AB methanolysis in which in-between each catalytic run, another equivalent of AB was added to the solution. The catalyst was washed with methanol after the fifth catalytic cycle to wash away excess salt byproduct (3 mmol AB, 0.5 mol % metal, 25 °C, 10 mL methanol solvent), (B) XRD of $C-Au_{66}Pd_{34}$ as-prepared, after ten catalytic cycles, and after storage in air for one year overlaid with the position of the (111) peak of fcc Au (ICSD 52249) and fcc Pd (ICSD 52251), (C) TEM images

of C−$Au_{66}Pd_{34}$ after the first, fifth, and tenth catalytic cycles of AB methanolysis (scale bars are 50 nm in length), and (D, left) Au 4f XPS spectra and (D, right) Pd 3d XPS of C−$Au_{66}Pd_{34}$ as-prepared, after ten catalytic cycles, and after storage in air for one year overlaid with pure metal signal. Reprinted with permission from ref 99. Copyright 2020 American Chemical Society.

The stability of $Pd_{34}Au_{66}$/C was explained through gold presence in the alloy matrix. Au may stabilize Pd, even in nanoparticles of diameter below 5 nm, by decreasing its ability to form oxides. Thus, stabilizing palladium through alloying and using simple supports might be a potential access to up-scaling those processes for industrial applications.[99]

The palladium-catalyzed methanolysis of AB benefited also recently of the formation of ultra small Pd nanoparticles encapsulated within the open cavities of soluble cages of the 1,3,5-tri(methylamino)aryl-based porous organic framework (POF) RCC3,[100] formed by a reverse-double solvent approach (R-DSA).[92] Different from classical impregnation method, R-DSA involved the use of a tiny amount of organic solution (CH_2Cl_2) of metal precursor ($Pd(OAc)_2$), with excess of an aqueous solution, to encapsulate the metal NPs inside the hydrophobic pores of the porous organic cages. The hydrophobic solvent contained the metal precursor, the absorption of which was driven by the strong interaction between the hydrophobic molecules and the hydrophobic cavities of the organic cage suspended in water. Adding a concentrated aqueous solution of reducing $NaBH_4$ yielded Pd@RCC3 with a dispersion of sub-nanometer Pd particles of average diameter about 0.7 ± 0.3 nm, which corresponds to the pore size of the POF *ca* 0.7 nm (as evidenced from high-angle annular dark-field scanning transmission electron microscopy (HAADF-STEM) and EDS mapping). The Pd@RCC3 catalyst (Pd 1.23 wt%) exhibited a catalytic activity for the methanolysis of AB with a TOF = 176 min^{-1}, conserved over five runs upon recycling. Notably, the Pd/RCC3 counterpart prepared by a conventional impregnation process on the POF, led to nonuniformly dispersed Pd nanoparticles of *ca* 2.2 nm average diameter. The catalytic methanolysis of AB was achieved with a lower TOF = 37 min^{-1}. Advances in the synthesis of palladium-based nanocatalyst for their use in the more sluggish hydrolytic dehydrogenation of DMAB at RT have also been reported,[102,103] with progresses like TOF passing above 45 min^{-1},[104] and tandem reaction development including nitroarene reduction.[105]

In AB dehydrogenative solvolysis the reactivity of palladium compared to rhodium performances is at least one order of magnitude lower, its cost being also considerably lower, but still quite high currently. Nevertheless, the development of *i*) alloys with low cost metal (Co, Ni) and plasmonic metals for light-promoted catalysis which kept the level of Pd-activity, *ii*) the development of methods for high dispersion of ultra small NPs below 1 nm conserved upon recycling (using structured supports), and *iii*) the tandem processes in which the versatile reactivity of palladium with H_2 was taken into benefit –like in selective olefins and alkynes hydrogenation and hydrodehalogenation of polluting organic aromatics– are very promising pathway for promoting a smart use of multitask palladium catalysts for dehydrogenation of amine-boranes.

3.3. Advances in platinum-based and alloys nanoparticle catalysts

The market price for platinum in June 2020 was 26,000 USD kg^{-1}, compared to 32,000 USD kg^{-1} in 2016 (–20%), and 50,000 USD kg^{-1} in 2012 (–36%).[65]

Chandra and Xu early on reported the dissociation and hydrolysis of AB complex at room temperature,[106] in a study where notably the performances of several different platinum, palladium and rhodium catalysts where comparatively established. In this pioneering work, various form of metallic materials including bulk metal, organometallic complexes, salts, supported or unsupported metal nanoparticles, were studied and their activity compared: for instance, 20 wt% Pt/C > 40 wt% Pt/C > $[Rh(1,5\text{-cod})(\mu\text{-}Cl)]_2$ > PtO_2 > Pt black > K_2PtCl_4, *etc*. This study established the great potential activity of platinum in AB hydrolysis, specially using highly dispersed small nanoparticles of less than 10 nm. Afterwards, platinum nanocatalysts immobilized on defect-rich oxidized CNTs supports were found to be active in the hydrolytic dehydrogenation of AB. The optimum sized Pt catalyst (*ca* 1.3 nm, 0.5 Pt wt%) showed an H_2 production activity up to TOF = 567 min^{-1} at 30 °C.[38] While pure Pt supported nanoparticles have confirmed the degree of activity accessible with platinum (Pt@MIL-10, TOF = 414 min^{-1};[107] Pt@TiO_2, TOF = 311 min^{-1}),[108] the recent studies have notably shifted towards the synthesis and application of innovative multimetallic platinum-based nanocomposites.[109,110,111,112,113]

The approach of single-atom heterogeneous catalysis has been implemented to single-atom alloy (SAA) made of atomically dispersed platinum on a surface of nickel particles.[109] Ni nanoparticles (5 to 10 nm size) supported on CNTs (5 wt% Ni), or covalent triazine frameworks (CTFs) and activated carbon C*, were synthesized as the parent catalysts. Then, different amounts of platinum in initial Pt:Ni molar ratios from 1:2 to 1:1000 were introduced to the parent catalysts by a galvanic reduction method. A water solution of H_2PtCl_6 was added slowly to the 5% Ni-based catalysts with a reduction-replacement process starting from the outer surface, the deposited Pt atoms being thus mostly integrated at the Ni surface (Figure 13, high-angle annular dark-field imaging–scanning transmission electron microscopy HAADF-STEM). In the resulting 1:1000 Pt–Ni/CNT in which 160 ppm of Pt substituted surface nickel, hydrogen evolution from aqueous AB showed a *ca* 3-fold activity improvement (TOF = 17.8 min^{-1}) in comparison to that of neat Ni catalyst (TOF = 5.8 min^{-1}).

Note that the pure 0.16% Pt/CNT catalyst showed a TOF = 448 min^{-1}. For higher Pt loading and activated carbon C* as support, 1:100 Pt–Ni/C*, a TOF = 57.1 min^{-1} *ca* 9-fold improved in comparison to that of pristine 5% Ni/C* counterpart is obtained.

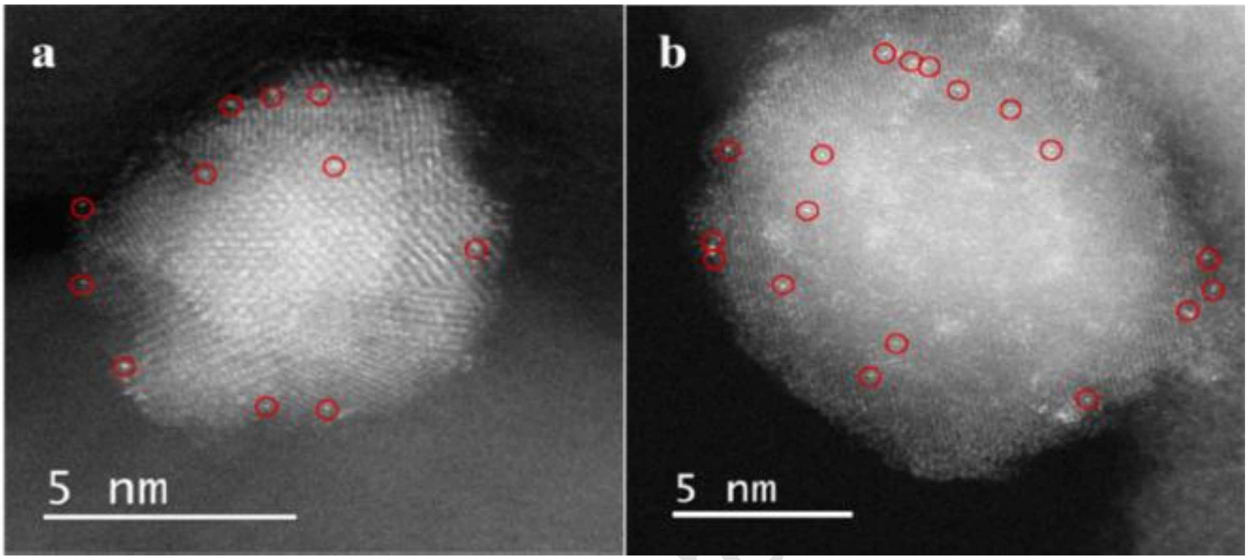

Figure 13. HAADF-STEM images of (a) 1/500Pt+Ni/CNT and (b) 1/1000Pt+Ni/CTF. The atomically dispersed Pt atoms (red circles) are contrasted on the Ni surface. Reprinted with permission from ref 109. Copyright 2017 American Chemical Society.

Pt atoms surrounded by Ni atoms were identified experimentally and theoretically as the most active center for H_2O activation. A calculation of TOF limited to an isolated platinum center gives a record apparent value of 12,000 min^{-1}. Simulation on such surface bimetallic alloys indicated that the activity enhancement might be explained by the negatively charged Pt ($Pt^{\delta-}$) surrounded by positively charged Ni ($Ni^{\delta+}$) in the Pt–Ni surface alloy (Bader charges), which would interact with $H^{\delta+}$ and $OH^{\delta-}$, respectively, for activating water molecules. It leads to an energetically favorable reaction pathway where the largest kinetic barrier involved the dissociation of an O−H bond to form the limiting transition state where the Pt atom capture an H atom from H_2O.

A somewhat related surface metal-atoms redox-replacement approach was used over cobalt nanoparticles (8-10 nm average sized) supported on fluffy N-doped mesoporous carbon (Co/mCN). By using Co/mCN composite dispersed into an aqueous solution of H_2PtCl_6 by ultra-sonication and 10 h stirring, a complete reduction of the oxidized Pt to metallic Pt(0) by metallic Co (releasing Co^{2+}) at the surface of the Co nanoparticles is assumed. While the existence of isolated platinum atoms or partial surface Pt coverage remains uncertain, the resulting Pt@Co/mCN nanocatalyst (3.34 wt% Pt and 10.12 wt% Co) was used in the catalytic hydrolytic dehydrogenation of AB at 35 °C giving a TOF = 118 min^{-1}. Magnetic recovering could be achieved over ten runs conserving the same volume of H_2 production and losing overall 1.5% of Pt loading (3.29 wt%).[110]

Beside such Pt–Co satellite-core association,[114] bimetallic $Pt_{50}Co_{50}$ nanoparticle alloys stabilized by triethylene glycol-terminated dendrimers (TGD) were recently reported (Figure 14).[111] PtCo@TGD were prepared by mixing dendrimer containing coordinating triazoles with two metal salts (Pt^{4+}, Co^{2+}) in water before addition of sodium borohydride for metals reduction. The 2.0 nm particles in $Pt_{50}Co_{50}$@TGD achieved a TOF = 164 min^{-1} at 20 ± 1 °C. This latter may be boosted by NaOH reaching a TOF = 257 min^{-1} (recalculated per surface atom TOF = 303 min^{-1}, and 476 min^{-1}, respectively). In comparison, monometallic analogs Pt@TGD and Co@TGD gave TOF = 120 min^{-1} and 8.8 min^{-1}, respectively. A notable "alloy composition effect" is observed since TOF of $Pt_{25}Co_{75}$@TGD = 138.5 min^{-1} and $Pt_{33}Co_{66}$@TGD = 150 min^{-1} were measured, respectively. The durability of the catalyst upon successive cycling (via reagent refilling) indicated a decrease of activity at the 5th run with nanoparticles strong aggregation (25 nm) and sodium and ammonium reaction products adsorbed on catalysts. For mechanistic purpose, cascade reactions were carried out for the hydrogenation of styrene with H_2 generated from AB hydrolysis with D_2O.[111] In a sealed system consisting of two communicating chambers, the hydrogen was produced from AB hydrolysis with D_2O, the reaction being catalyzed by $Pt_{50}Co_{50}$@TGD in a first tube. This hydrogen was used for the hydrogenation of styrene catalyzed by Ni_2Pt@ZIF-818 in a second tube. Styrene hydrogenation was achieved at 50 °C for 12 h, giving three hydrogenation products containing zero, one, or two D atoms in the ethyl substituent. The deuteration of the ethylbenzene products confirms H/D exchange after O−D cleavage in AB hydrolysis, and H/D scrambling on the PtCo bimetallic nanoparticle surfaces.

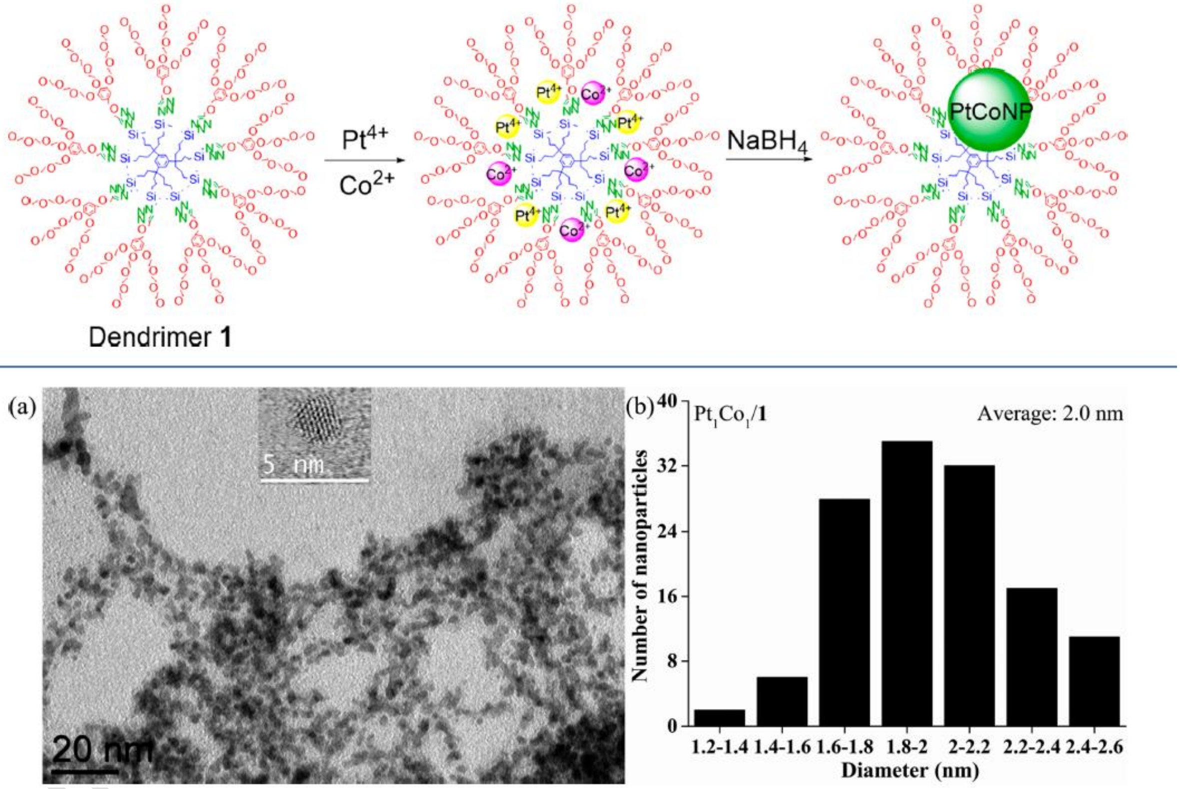

Figure 14. Top: Synthesis of the Pt−Co/1 NPs; Bottom: (a) TEM image (inset is the HRTEM image) and (b) size distribution of $Pt_1Co_1/1$. Reprinted with permission from ref 111. Copyright 2017 American Chemical Society.

Bimetallic Pt–Pd alloy nanoparticles stabilized by hydroxyl-terminated sixth-generation polyamidoamine dendrimer (G6-OH) have also been studied.[112] Aqueous solutions of K_2PtCl_4 and K_2PdCl_4 were sequentially added to an aqueous G6-OH solution. The molar ratio of the precursor Pt and Pd salts was adjusted, the mixture stirred three days to ensure complexation of the ions with the interior amines of G6-OH, and an excess of $NaBH_4$ was added for full metal reduction. The resulting Pt_nPd_{180-n}@G6-OH were dialyzed for 24 h using a cellulose dialysis sack to remove impurities. The TEM images indicated that the composites were mostly not aggregated and fairly monodisperse with stabilization of the metal particles via their encapsulation inside the dendrimers with quite uniform size *c. a.* 1.7 nm, a value in agreement with the theoretical value 1.72 and 1.73 nm calculated by assuming a spherical geometry of nanoparticles containing 180 platinum or palladium atoms, respectively. The single-particle elemental mapping measurement of $Pt_{90}Pd_{90}$@G6-OH confirmed that both Pt and Pd were alloyed within the single nanoparticles. HRTEM image indicated from fringes that some bimetallic nanoparticles were crystalline. In hydrolytic dehydrogenation of AB, the $Pt_{90}Pd_{90}$@G6-OH exhibited the highest catalytic activity with a TOF = 108 ± 16 min^{-1}. Comparatively, monometallic counterpart Pt_{180}@G6-OH and Pd_{180}@G6-OH showed an activity with TOF = 33 ± 8 and 21 ± 2 min^{-1}, respectively. Puzzlingly, a value of TOF = 79 ± 7 min^{-1} was found from a physical mixture of monometallic Pt_{90}@G6-OH and Pd_{90}@G6-OH, less efficient than the bimetallic, but significantly higher than with pure monometallic samples. A redistribution of the nanoparticles might be plausible correlating their apparent poor stability under electron beam irradiation in STEM-EDS measurement.

Pt–Pd nanoparticles supported on amino-functionalized and N-doped reduced graphene oxide (NH_2-N-rGO) were prepared by sonication of (3-aminopropyl)triethoxysilane (APTS) into a GO aqueous suspension, followed by the addition of K_2PtCl_6 plus Na_2PdCl_4 solution, stirring and reduction with $NaBH_4$.[113] $Pt_{50}Pd_{50}/NH_2$-N-rGO bimetallic composite displayed nanoparticles size distributed around 1.9 ± 0.4 nm, from which alloy formation is suggested by HRTEM analysis. Using those mild preparation conditions, the introduction of NH_2 group into N-doped rGO seems to be crucial to prepare dispersed Pt–Pd nanoparticles of small size, since otherwise agglomerated composites were obtained from pure rGO or N-doped rGO. Among pure Pt, Pd and Pt_xPd_x composite catalysts supported over various substrates (rGO, N-rGo), $Pt_{50}Pd_{50}/NH_2$-N-rGO exhibited the highest activity for the catalytic hydrolytic dehydrogenation of AB, with a reported TOF around 699 min^{-1} while the catalyst metal loading was not reported. Four recycling runs were achieved with a low degradation of activity.

Photo-assisted catalytic use of platinum nanoparticles for AB dehydrogenation were also recently reported.[115,116] Platinum nanoparticles were supported on visible-light active semiconductor mesoporous graphitic carbon nitride (mpg-CN), via the *in situ* reduction of preformed Pt^{IV}@mpg-CN composites in the catalytic hydrolysis of AB under white-light irradiation.[115] Functional groups at mpg-CN surface include pyridinic, pyrrolic, and amino groups which coordinates transition metal ions in the impregnation step, favoring nanoparticles dispersion during their nucleation/growth process. In addition, mpg-CN as a semiconductor polymeric material with a band gap of 2.7 eV (454 nm) exhibits visible-light photocatalytic activity. However, mpg-CN suffers from the rapid recombination of the excited charges upon the light irradiation. This drawback might be overcome through the construction of a Mott−Schottky catalyst by loading Pt on mpg-CN. Accordingly, the catalytic hydrolysis of AB by Pt@mpg-CN under white-light illumination increased the TOF value by 2.2-fold compared to that of in-dark conditions, confirming that Pt@mpg-CN nanocatalysts behave as a heterojunction photocatalyst. With 5.94 wt% Pt loading (nanoparticle average size *c. a.* 6

nm) the hydrolysis of AB achieved a highest TOF = 274 min^{-1} that is preserved at 78% after 10th consecutive runs. While the *in situ* synthesis protocol might be convenient, curiously, agglomerated particles and clumps are observed for 5.94 wt% Pt loading samples, somewhat inducing platinum waste. Conversely, no agglomerates or large particles are observed for Pt@mpg-CN nanocatalysts (of lower efficiency) with 3.82, 2.08, and 1.16 wt% Pt loadings. The enhancement in catalytic activity under white light irradiation was suggested by regarding the valence band (VB) and conduction band (CB) energies of mpg-CN, calculated as 1.75 and −1.05 eV, respectively (Figure 15), and the work function of Pt located between the VB and CB of mpg-CN.[115] Upon the irradiation of mpg-CN, electron−hole pairs are generated in the CB and VB of mpg-CN, respectively. The photo-excited electrons flow from the CB of mpg-CN to the d-band of Pt which is lower than CB of mpg-CN through the interface formed between mpg-CN and Pt nanoparticles. This give rise to the formation of Schottky barrier at the interface. The Schottky barrier induces delay of electron−hole recombination and promotes charge separation. Consequently, electron-enriched active platinum sites favoring the hydrolytic dehydrogenation of AB are formed.

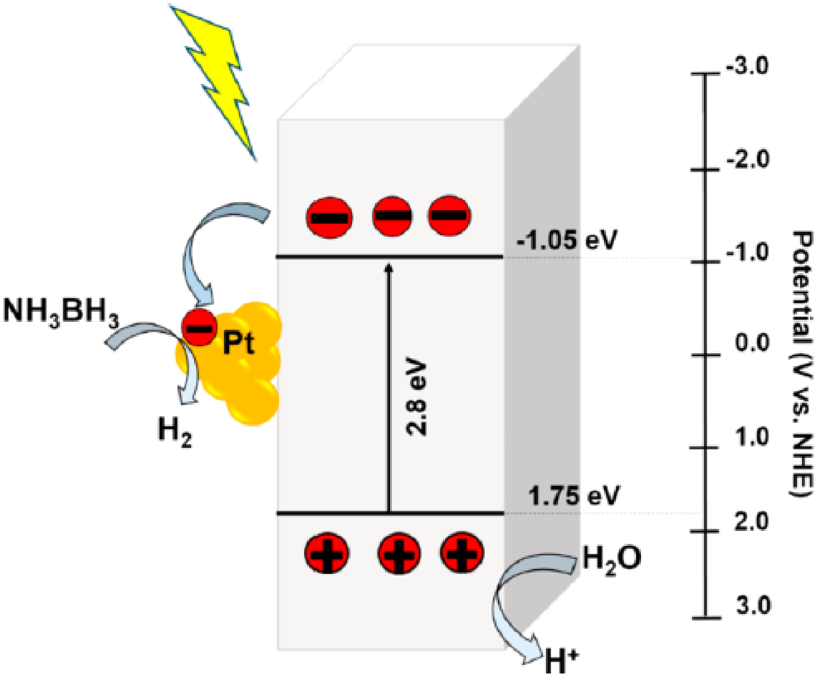

Figure 15. Proposed mechanism for the photocatalytic AB hydrolysis in the presence of mpg-CN/Pt nanocatalysts under white light irradiation. Reprinted with permission from ref 115. Copyright 2020 American Chemical Society.

Another photo-assistance to platinum catalyzed hydrolytic dehydrogenation of AB was achieved from plasmonic titanium nitride support.[116] Upon light illumination, plasmonic photocatalysts support the collective oscillations of free carriers as localized surface plasmon resonance (LSPR). This latter concentrates light at the nanoscale and produces very intense electric fields. LSPR undergo nonradiative decay, which generates highly energetic electron−hole pairs (called hot carriers) with capability to boost chemical reactions. Accordingly, titanium nitride nanocubes (TiN-nano^3, average size 41 ± 10 nm) were decorated with 3.3 ± 0.3 nm platinum nanoparticles on their surface (Figure 16). With the view to insure the binding of platinum nanocrystals onto the surface of the plasmonic core, commercial TiN nanocubes were treated with concentrated HCl and reacted with K_2PtCl_4 in the presence of formaldehyde as a mild reducing agent. NaOH achieved the formation of dispersed platinum particles and neutralized the HCl evolved during the reduction of the platinum precursor at the surface of TiN nanocubes. A final reduction step under H_2 flow at 200 °C for 2 h was applied to clean up the nanoparticle surface and increase the catalytic activity of plasmonic nanohybrides.

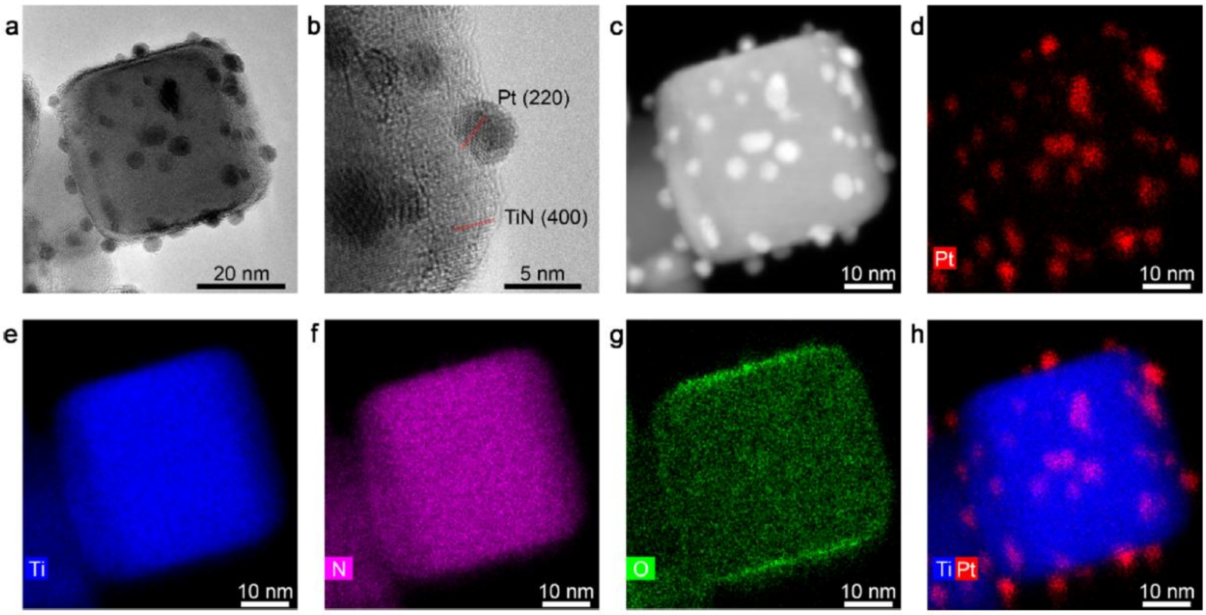

Figure 16. (a) Representative TEM image of a single TiN−Pt system where Pt nanocrystals are uniformly distributed over a TiN nanocube. (b) Magnified high-resolution TEM image showing lattice fringes of TiN and Pt. (c−h) Dark-field STEM image of a representative TiN−Pt nanohybrid and EDS elemental maps of Pt (d), Ti (e), N (f), O (g), and an overlay of Ti and Pt (h) showing the spatial distribution of Pt nanocrystals over TiN nanocubes. Reprinted with permission from ref 116. Copyright 2020 American Chemical Society.

Dark-field scanning TEM image and EDS elemental mapping highlighted that platinum nanoparticles arranged homogenously around the TiN core. Oxygen elemental mapping showed the presence of a 1.5 nm thick passivation layer. This latter usually formed in TiN nanostructures as TiON/TiO_2 mixture upon exposure to air or chemicals is rich in oxygen and acts as a protective shell towards further in-deep oxidation. The Pt@TiN nanocube hybrids showed under resonant conditions at 700 nm, hot electron-driven hydrogen evolution from AB at an apparent quantum yield of 120% (calculated under monochromatic light by using the reaction rate difference between light and dark conditions).[116] Thus, irradiation enhanced the activity of Pt@TiN hybrids by one order of magnitude. The photocatalytic performance of these nanohybrides at RT was analyzed by distinguishing TOF into two parts: TOF_{photo} (H) =

TOF_{therm} (H) + $TOF_{hot\ -e}$ (H), where TOF_{photo} is the overall photothermal H_2 evolution rate, TOF_{therm} is the thermal contribution, and TOF_{hot-e} is the contribution coming from non-thermalized energetic electrons (hot electrons) at a given light intensity (H). Since TOF_{photo} and TOF_{therm} can be experimentally determined, the contribution of hot electrons can be estimated. At 10 suns illumination, TOF_{photo} reached 346 min^{-1} with Pt@TiN showing a *c. a.* 10-fold enhancement in catalytic activity with respect to dark conditions (TOF = 32 min^{-1}). The combined effect of photothermal heating and hot electrons is responsible for this order of magnitude difference. However, the heating contribution is prominent at low intensity light irradiation, while it becomes less than 50% of the TOF_{photo} value at 10 suns; the hot electron effect being thus prominent at increasing light intensity. The catalytic performance of the nanohybrides remained comparable after three consecutive catalytic cycles. Tandem hydrogenation of 4-nitrophenoxide anion using *in situ* generated H_2 gas evolved from plasmon-enhanced NH_3BH_3 dehydrogenation using Pt@TiN was achieved. The hydrogenation rate in the dark and under illumination being respectively 0.17 and 0.42 min^{-1}, suggested that plasmonic effects can also produce a 2.5-fold rate enhancement in this hydrogenation.[116]

Progress was also achieved from platinum unsupported nanoparticles for dehydrogenative methanolysis of AB, including in its use for tandem hydrogenation of unsaturated substrates.[117] Platinum colloidal nanoparticles were synthesized under mild conditions by decomposing a THF solution of zerovalent bis(dibenzylideneacetone)platinum, [Pt(dba)$_2$], at RT under H_2 pressure in the presence of a bulky phosphane bearing terphenyl group that serves as surface stabilizing ligand (Figure 17, left). Using as catalyst the resulting Pt@LPMe$_2^{i\text{-Pr}}$ (L/Pt = 0.2 mol, Pt 0.19%, average size 1.2-2.5 nm, Figure 17, middle), the production of H_2 from methanol solutions of H_3NBH_3 was performed at 30 °C giving a TOF = 284 min^{-1}.

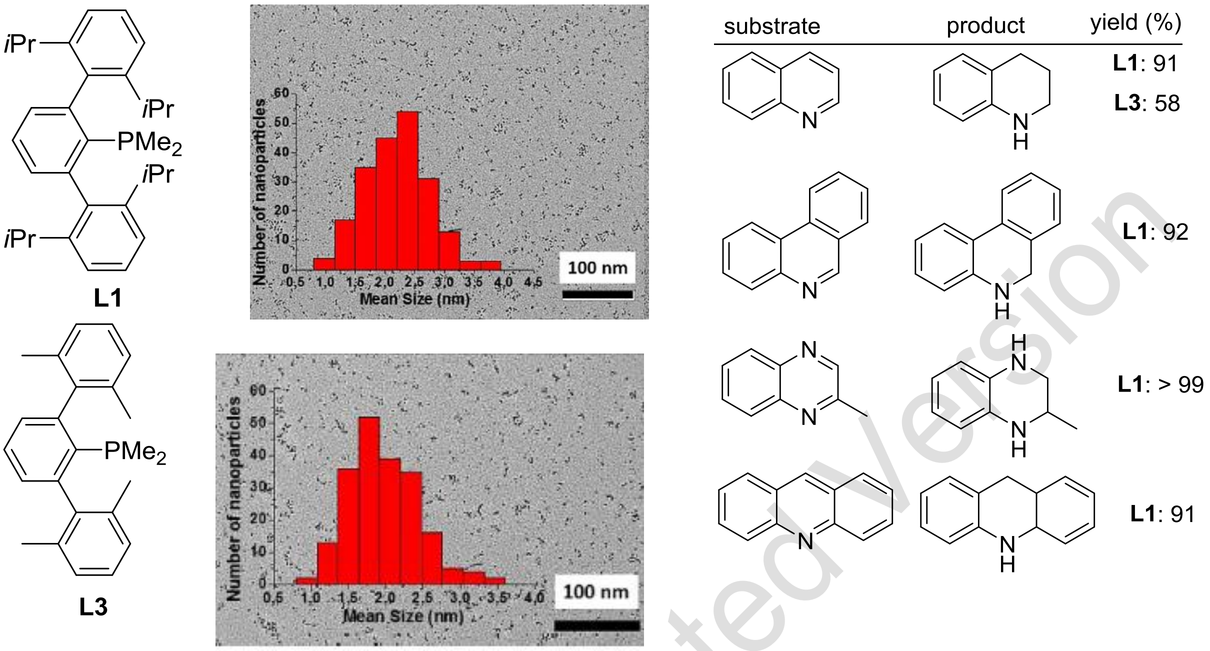

Figure 17. Left: terphenylphosphanes L used to stabilize platinum NPs; Middle: TEM imaging and size histograms of PtL1 (top) and PtL3. Right: tandem $H_3N.BH_3$ methanolysis/*N*-heterocycle hydrogenation with Pt NPs. Reprinted and reproduced with permission from ref 117. Copyright 2019 Wiley-VCH Verlag GmbH & Co. KGaA, Weinheim.

The catalyst separation for three runs recycling was achieved after distillation of the H_2-depleted ammonium tetramethoxyborate, $NH_4B(OMe)_4$, that is deemed easy to sublimate and regenerate using $LiAlH_4/NH_4Cl$.[117] Additionally, such colloidal systems, which uses 1 wt% Pt, achieved one-pot dehydrogenation of AB and *N*-heterocycles reduction of quinoline, phenanthridine, 2-methylquinoxaline and acridine in 58-99% yields at 60 °C in 21 h in methanol (products shown in Figure 17, right).

Dehydrogenation of DMAB, as more demanding reaction, has also been recently achieved by using platinum bimetallic alloying with iridium.[118] Composites of Pt-Ir alloy nanoparticles and GO were prepared by reducing Pt(IV) and Ir(III) chlorine salts in a THF solution using super hydride ethanol reduction method at RT. The average particle size was 4.3 ± 0.4 nm. The atomic lattice fringe portion of $Pt_{50}Ir_{50}$@GO nanoparticles measured at 0.23 nm is characteristic of the alloy formation, which was further supported by TEM-electron energy loss spectroscopy (EELS) analysis showing a 1:1 Pt-Ir in the alloy (Figure 18).

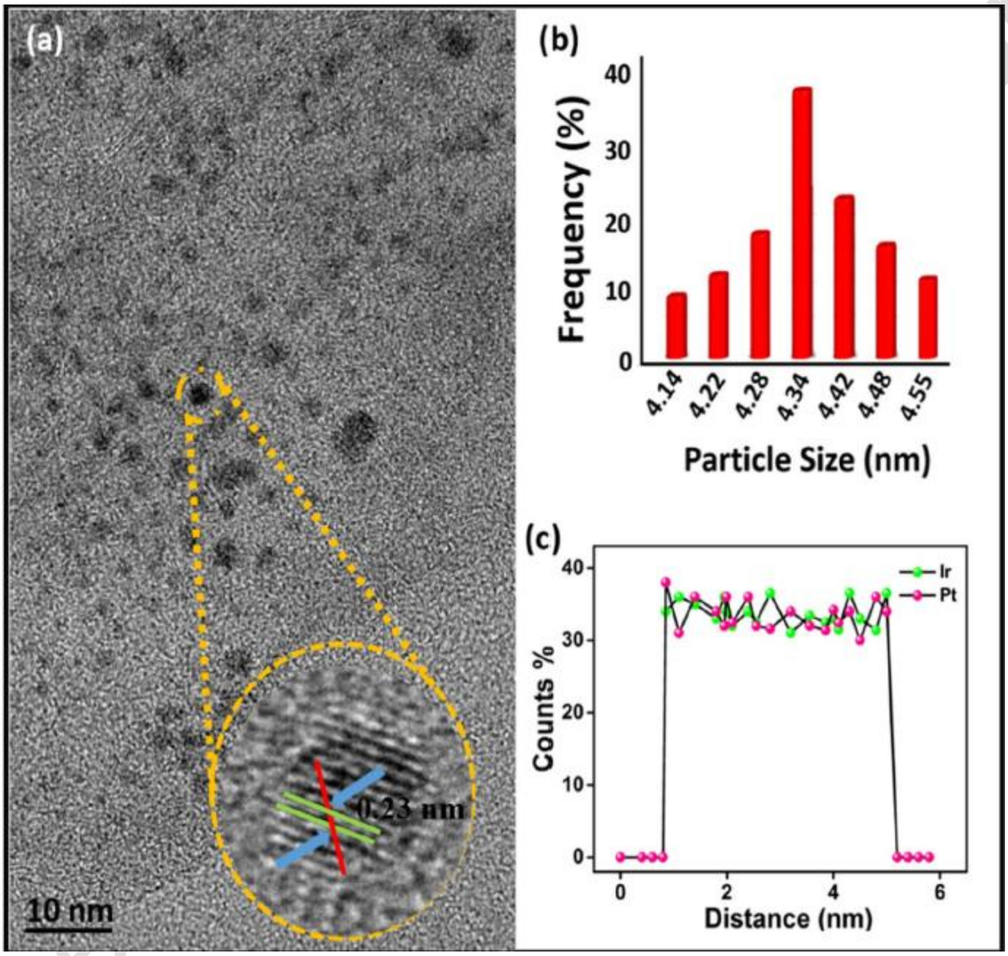

Figure 18. (a) TEM analyses patterns (b) particle size histogram (c) The EELS analyses of PtIr@GO nanoparticles. Reprinted with permission from ref 118. Copyright 2019 Springer Nature.

$Pt_{50}Ir_{50}$@GO exhibited catalytic activity in the dehydrogenation of DMAB in THF solution, and release of H_2 gas without induction time with a TOF = 3.8 min^{-1} was achieved. The same catalytic reaction with Pt(IV) and Ir(III) salts used as pre-catalysts in the absence of GO exhibited a 7 min induction time and only a 10–15% conversion. In this case, only chloride anions poorly stabilized Pt-Ir metal nanoparticles that aggregated and precipitated within 10 min. The catalytic activity and reusability experiment were carried out for four runs where $Pt_{50}Ir_{50}$@GO maintained its starting catalytic activity up to 77% at ambient conditions. The agglomeration of NPs, occurring upon recycling, highlighted the weak interaction between the support and the alloy nanoparticles. The excellent activity of platinum in AB hydrolytic dehydrogenation gave systems with TOF slightly superior to palladium, in general, for a current price of the metal about 3-fold lower. However, the market volatility is noticeable for these metals that are also highly used resource in automobile post-combustion, especially platinum.

3.4. Advances in ruthenium-based and alloys nanoparticle catalysts

The market price for ruthenium in June 2020 was 9,000 USD kg^{-1}, compared to 1,350 USD kg^{-1} in 2016 (+600%), and 3,600 USD kg^{-1} in 2012 (–60%).[65]

Ruthenium nanoparticle catalysts having activities in the hydrolytic dehydrogenation of AB are considered as competitive with platinum and palladium nanocatalysts.[15,18] For instance monodisperse small ruthenium nanoparticles supported on graphene (mean size 1.9 nm),[37] or TiO_2 supports (mean size 1.7 nm),[52] achieved the highest reported TOF around 600 min^{-1}. The recent studies oriented the research towards carbon supports of varied nature with contrasted results. Mori and Yamashita reported carbon-supported Ru nanoparticles (Ru/C) based on the impregnation of the $[Ru^{II}(bpy)_3]^{2+}$ on carbon support (Shirasagi M, powdered average pore diameter 2.0 nm) and subsequent precursor decomposition by heat treatment at temperatures ranging between 600 to 1000 °C. This parameter had an impact on the features of the catalysts and its performance in H_2 production from AB hydrolysis.[119] While, Ru (0.5 wt%)

nanoparticle size increased with increasing the temperature (Ru/C formed at 1000 °C gave up to 50 nm size), the optimum catalyst was shown to be the sample Ru/C formed at 800° C, with nanoparticles size averaging 7 nm, for a TOF number of 670 min^{-1} in hydrolytic dehydrogenation of AB at 30 °C (retaining 60% of the initial TOF in the fifth run of recycling). The presence of geometric B5-type sites[119] at edges of Ru nanoparticles was hypothesized for accounting its specific activity. Interestingly, the effect of Ru crystal phase on the catalytic activity in hydrolytic dehydrogenation of AB has also been addressed using fcc-structured and hexagonal close packed structured Ru nanoparticles supported on γ-Al_2O_3, including DFT approaches.[120] The results showed that the catalytic activity is different even if these two kinds of Ru nanoparticles hold similar range of sizes. From a catalyst preparation perspective, and conversely to Mori and Yamashita results above-described,[119] lower temperature pyrolysis method for preparing dispersed Ru nanoparticles on carbon (Vulcan XC-72) Ru/C was achieved by calcination at 300 °C using Ru^0 precursor $Ru_3(CO)_{12}$. This led to activity for H_2 evolution from AB hydrolysis with TOF = 643 min^{-1} (retaining 50% of the initial TOF in the eighth run of recycling).[121] For the Ru/C formed at 300 °C (Ru wt% not given), TEM showed that the carbon matrix is covered with dispersed metal nanoparticles with a diameter of *ca* 1.5 nm.

The catalytic activity of Ru/nanodiamond was also studied for hydrogen production from AB hydrolysis at 25 °C. Nanodiamond supported ruthenium nanoparticles (6.21 wt%), with a mean particle size of 3.7 nm exhibited catalytic activity for AB hydrolysis with a TOF = 229 min^{-1}.[122] Upon recycling, gradual decrease in the catalytic activity was significant with a 40% of the initial TOF retained in the fourth run. The same range of activity was achieved from MOF supported ruthenium catalysts Ru/MIL-53(Al)-NH_2 (Ru 18.10 wt%), which exhibited a TOF = 287 min^{-1} in hydrolytic AB dehydrogenation.[123,64] The MOF was believed to insure the formation and stabilization of ultra-small Ru NPs by preventing their aggregation (with a mean diameter of 1.2 and a size distribution ranging from 0.3 nm to 2.4 nm). The Ru/MIL-53(Al)-NH_2 retained *ca* 80% of its initial catalytic activity in fifth successive cycles of the hydrolytic dehydrogenation of AB.

For ruthenium supported nanoparticles, a gap of activity for hydrolytic H_2 evolution from AB was leapt over in 2019 by several groups, specifically using various porous carbon supports.[124,125,126,127] Ultra-small Ru nanoparticles (diameter 1.3 nm) were synthesized by dispersion and pyrolysis between 300-700 ^{o} C of $RuCl_3$ over 3D nanoporous sheets of N-doped carbon (3DPC) –itself achieved by calcination at 800 °C of a mixture of macroporous acrylic resin and urea–.[124] The 3DPC substrate achieved specific surface area and pore volume of 1138 m^2 g^{-1} and 0.44 cm^3 g^{-1} with hierarchical nanopores centered at *c. a.* 2.6 nm. Upon the anchoring of Ru nanoparticles, the specific surface area of Ru/3DNPC-500 (formed at 500 °C) decreased to 1097 m^2 g^{-1} without obvious changes of pore size and volume. Ru/3DNPC-500 achieved a TOF = 584 min^{-1} for hydrolytic decomposition of AB at 25 °C, and suffered a 50% decrease of its initial activity along seven recycling runs.

In a bio-resource utilization approach, Sun group experimented with success the deposition of poly(N-vinyl-2-pyrrolidone)-stabilized ruthenium nanoparticles on bamboo leaf-derived porous carbon (Ru/BC).[125] BC supports were obtained by calcination at 800 °C of a 2:1:6 wt% mixture of dried bamboo leaves, hydrochloride semicarbazide, and potassium hydroxide. Ru/BC catalysts were synthesized via *in situ* reduction by AB of aqueous solution of $RuCl_3$ in the presence of PVP (1 to 10 mg). Ru/BC-1 (stabilized by 1 mg PVP), while rather ill-defined (NPs of less than 10 nm without precise size distribution, no detailed structure and porosity of support), achieved a TOF = 718 min^{-1} for hydrolytic AB decomposition, retaining 55 % of the initial catalytic activity after ten cycling runs. Similarly, N-doped porous carbon (NPC, Figure 19) was used as support for *in situ* reduction of $RuCl_3$ by aqueous solution of AB.[126]

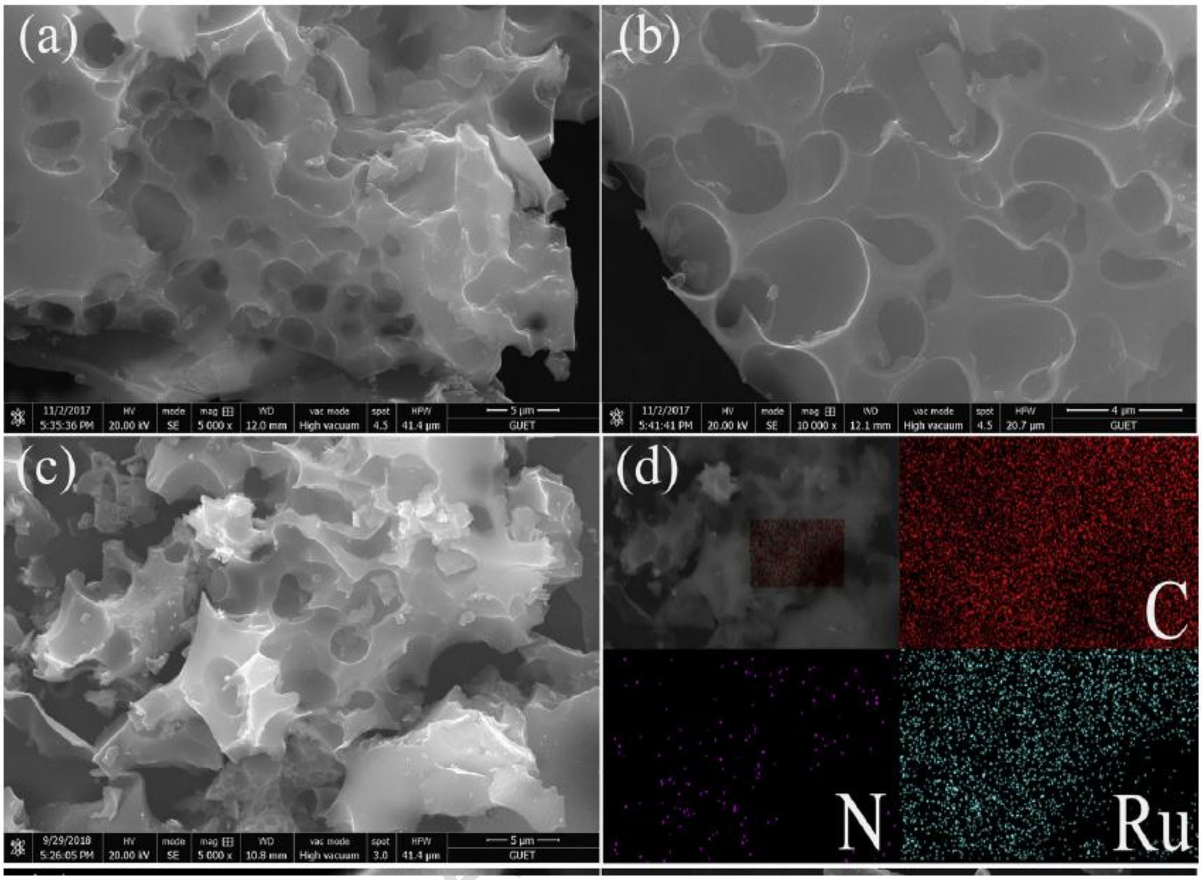

Figure 19. SEM images of NPC (a and b) and Ru/NPC catalyst (c and d). Reprinted with permission from ref 126. Copyright 2018 Hydrogen Energy Publications LLC, Elsevier Ltd.

NPC support was synthesized by hydrothermal method. Hydrochloride semicarbazide and glucose were mixed and treated at 180 °C and further calcinated with potassium hydroxide at 700 °C.[126] For NPC support, BET surface area and micropore specific surface area were measured respectively at 1976 m^2 g^{-1} and 1037 m^2 g^{-1} with an average pore sizes about 2.0 nm with both micropores and mesopores. Nitrogen content was measured respectively at 2.98 wt% and 3.06 wt% for NPC and Ru/NPC, with 9.98 wt% Ru for the Ru/NPC composites. While nanoparticles size and size distribution were ill-defined (several dozens of nm), a TOF

= 813 min^{-1} for hydrogen production from AB hydrolysis was reported, and 67% of the initial catalytic activity was retained after five cycling runs. Regarding bio-resources utilization for generating carbonized support towards the formation of Ru/C catalysts able to AB hydrolysis, a two-step synthesis strategy based on hydrothermal synthesis and solid-phase carbonization to fabricate N-doped bagasse-derived carbon materials as been reported,[128] as well as the utilization of ginkgo leaf,[129] from a tree used in traditional Chinese medicine.

The most advanced works on porous carbon supports for Ru nanoparticles active in AB hydrolysis described a one-step pyrolysis method towards hybrid catalysts comprising uniform hollow porous carbon spheres (HPCS) loaded with ruthenium nanoparticles (Ru@HPCS).[127] Nitrogen-doped hollow porous carbon spheres were obtained by removing the template spherical SiO_2 core (using aqueous HF) of a carbonized preformed raspberry-like composite material polystyrene/silica. This templating method conserved the raspberry-like structure for the porous carbon and globally generated hollow spheres. Microscopy images of a typical HPCS sample (Figure 20a,b) show the as-prepared HPCS as possessing a uniform size around 200 nm with similarly proportioned and well-distributed porosity. Ru@HPCS from the hydrothermal reaction of $RuCl_3$ and HPCS at 160 °C for 8 h led to dispersed Ru NPs of *c. a.* 2.2 nm, homogeneously anchored on the outside and inside of the HPCS. The intensity profile of the high-angle annular dark-field (HAADF)-STEM image (Figure 20c) indicates the formation of crystalline sub-2 nm Ru nanoparticles. High-resolution TEM (HRTEM) image reveals the lattice fringes with d-spacing of 2.1 Å, corresponding to plane Ru(002) (Figure 20d). Elemental mapping suggested the well-defined spatial distribution of C, N, and Ru in the Ru@HPCS (Figure 20e). ICP–AES indicated a total Ru content about 4.9 wt%.[127] Ru@HPCS achieved BET specific surface area of 413 $m^2\ g^{-1}$ (compared to 516 m^2

g^{-1} for HPCS support), with mesopores mainly around 9 nm in size which is smaller than the size of the pure HPCS support (30 nm), indicating that Ru nanoparticles were encapsulated in hollow porous carbon shells. Multiscale porosity as such was favorable for increased specific surface area and fast charge transfer, which may benefit electrochemical processes.

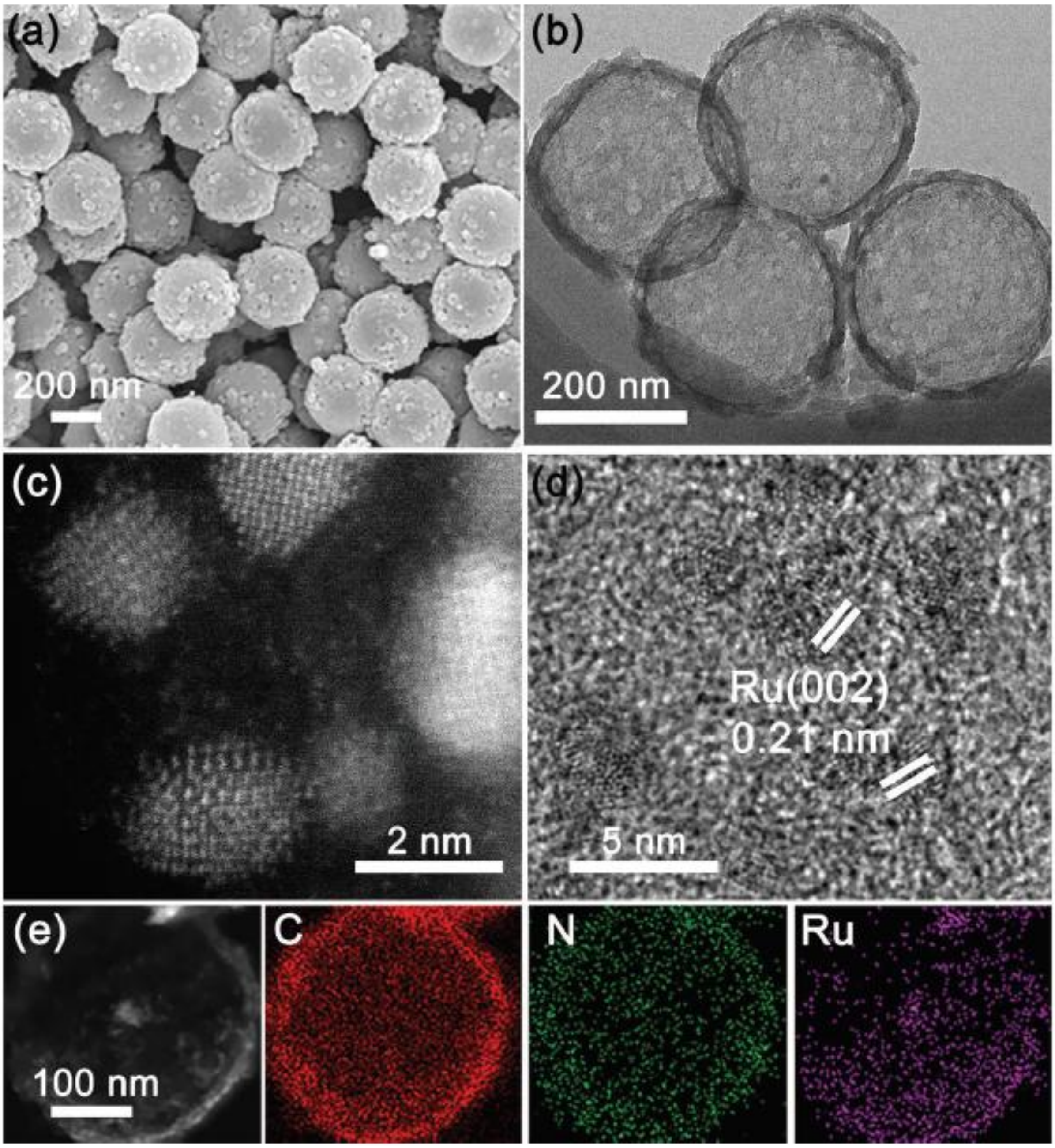

Figure 20. a) SEM and b) TEM images of Ru@HPCS. c) Atomic-resolution HAADF-STEM of Ru nanoparticles in Ru@HPCS. d) HRTEM image of Ru@HPCS. e) HAADF-STEM image of Ru@HPCS and

corresponding EDX mapping of Ru@HPCS for C, N, and Ru elements. Reprinted with permission from ref 127. Copyright 2019 WILEY-VCH Verlag GmbH & Co. KGaA, Weinheim.

Accordingly, this Ru@HPCS nanocatalyst presented a catalytic activity both for the electrolysis of water, and the hydrolysis of AB with a reported TOF = 706 min^{-1} at 25 °C for the latter.[127] Catalyst durability was tested over six cycles by achieving one hydrolysis of AB reaction plus one electrolysis of water as a cycle (apparently retaining at the 6th run *c. a.* 67% of its initial TOF for complete conversion in AB dehydrogenation at 25 °C). Such material may be thus used for both electrochemical and chemical hydrogen generation, providing a multitask catalyst for hydrogen production.

Carbon-based magnetic supports were also employed from their formation as carbon-coated iron particles (C-Fe) by co-processing of iron powders with methane in a radio frequency thermal plasma reactor.[130] This allowed the comparisons of metal(0) nanocatalysts activity. The samples were prepared by impregnation of Ru(III), Rh(III) and Pd(II) on the C–Fe supports followed by reduction from an aqueous solution of sodium borohydride at RT. The resulting catalytic materials (0.45 wt% Rh, 1.59 wt% Ru, and 2.0 wt% Pd) were tested for hydrolysis of AB at 25 °C, and achieved TOF = 83, 93, and 29 min^{-1}, respectively; the performance of the ruthenium NPs being superior. The TOF somewhat lower than standard with carbon supports, was attributed to the fairly small surface area of the support (34.8 $\text{m}^2\ \text{g}^{-1}$) and to the low dispersion of large metallic aggregates. As expected, these nanocatalysts could be magnetically separated, rinsed and reused in five cycles with a conservation of their original TOF activity.

Bimetallic nanocatalysts based on ruthenium and alloyed with less expensive metals have been proved efficient for hydrolytic AB dehydrogenation. For example, Mori and Yamashita studied both the effect of inorganic oxide support on ruthenium NPs, and alloying of Ru with nickel.[52] Ru/MgO, Ru/Al_2O_3, Ru/ZrO_2, and Ru/SiO_2 nanocatalysts showed catalytic activity for hydrogen evolution from AB hydrolysis with TOF ranging between 100 and 200 min^{-1}. In contrast, Ru/TiO_2 P25 (anatase + rutile), Ru/TiO_2 (rutile), and Ru/TiO_2 (anatase) exhibited at Ru 2.0 wt% enhanced TOF = 558, 510, and 455 min^{-1}, respectively. No direct relationship could be established between these catalytic activities and brut BET surface areas of the materials. The BET surface area of TiO_2 P25 (anatase + rutile) and TiO_2-rutile were 39.7 and 40.0 m^2 g^{-1}, respectively, which was much lower than the 338 m^2 g^{-1} measured for TiO_2-anatase. Ru NPs supported on ZrO_2 or Al_2O_3 also showed lower activity, despite surface areas of the supports around 70 m^2 g^{-1}. However, smaller sizes of Ru nanoparticles with a mean diameter of 1.7 nm could be achieved on TiO_2 by H_2 reduction at 200-300 °C. The size of the Ru NPs rather than the surface area of the support was assumed to be the crucial parameter to achieve further optimized catalytic activity. In this perspective, the reduction conditions were found to be determining (Figure 21). Reduction by H_2 was the best method to achieve high catalytic activity in comparison to chemical methods using $NaBH_4$, NH_3BH_3, or HCOONa.[52]

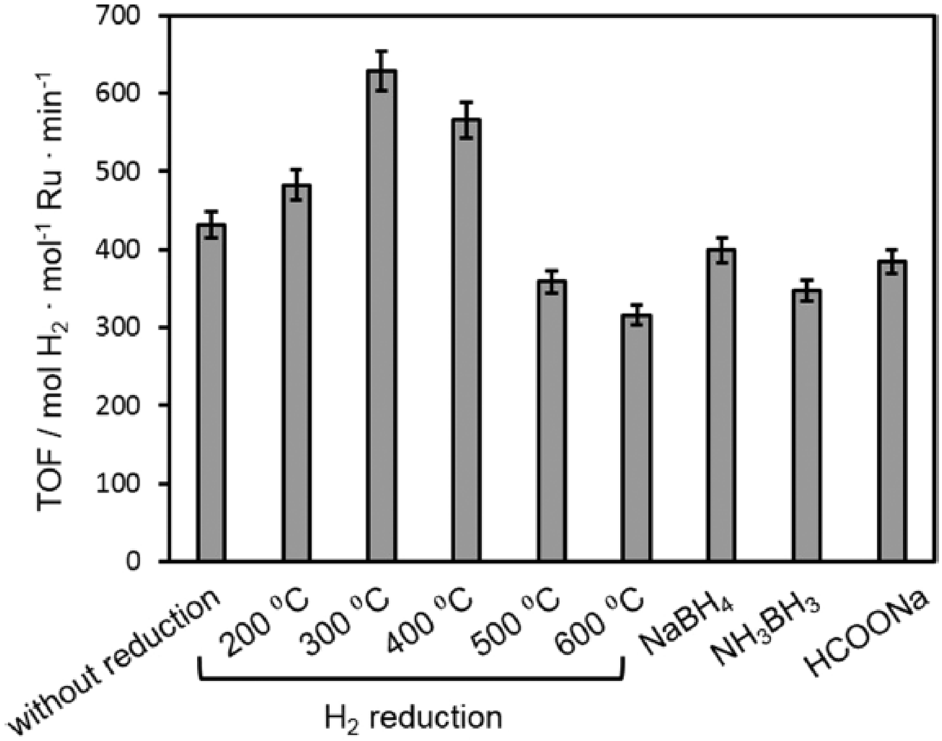

(Figure 21). Catalytic activity for hydrogen production from AB for Ru/TiO_2 P_{25} prepared under various reducing conditions. Reprinted with permission from ref 52. Copyright 2016 American Chemical Society.

The H_2 reduction temperature also apparently influenced the catalytic activity. A maximum activity was obtained for H_2 reduction achieved in the range of 200-300 °C. From TEM imaging the average diameter of the Ru NPs reduced at 600 °C was found at 3.1 nm.

In addition, Ru nanoparticles activity can be significantly enhanced by alloying with Ni atoms, whereby a TOF = 914 min^{-1} was achieved (based on Ru content only from $Ru_{75}Ni_{25}$, Ru 1.0 wt%) with a total turnover number (TTO) of *c. a.* 153,000 over 8 h. The reactions using pure Ni/TiO_2 were sluggish, whereas strong enhancement was observed with the Ru-Ni alloy nanocatalysts with a maximum obtained from $Ru_{77}Ni_{23}$ (2.3 nm average size).

Bimetallic nanocatalysts active for hydrolytic dehydrogenation of AB and incorporating Ru were also formed with high molar content of copper ($Cu_{92}Ru_8$@PC),[131] and cobalt

($Co_{90}Ru_{10}/TiO_2$ and $Co_{95}Ru_5$/PVA-foam, polyvinyl alcohol),[132,133] and for which TOF = 97, 141 min^{-1} and 169 min^{-1} were achieved, respectively (related bimetallic associations are discussed in more details in the corresponding section 3.8 (Cu) and 3.6 (Co), respectively).

Another important application of Ru-based nanocatalysts concerned the hydrogen production from more challenging substrates like MeAB (methylamine borane, $H_3CNH_2 \rightarrow BH_3$) and DMAB, substrates that are notoriously more reluctant to hydrolysis than AB.[25] Early on works providing the first reusable systems were reported by Philippot and coworkers.[134] Ru^0 colloidal nanoparticles with a mean size of 1.7 nm and a size distribution ranging from 0.8 to 2.8 nm were stabilized by APTS ligated by the amino group (Figure 22), in the absence of further support. Ru/APTS were synthesized by the mild decomposition of the organometallic precursor [Ru(cod)(cot)] (cot = 1,3,5-cyclooctatriene) in THF under 3 bar H_2 at RT in the presence of 1 equiv of 3-APTS per mole of Ru. Ru(0)/APTS achieved a TOF = 0.9 min^{-1} (53 h^{-1}) in dehydrogenation of DMAB at 25 °C and retained 90% of their initial catalytic activity at the third run; the NPs grown up to 2.9 ± 0.6 nm.

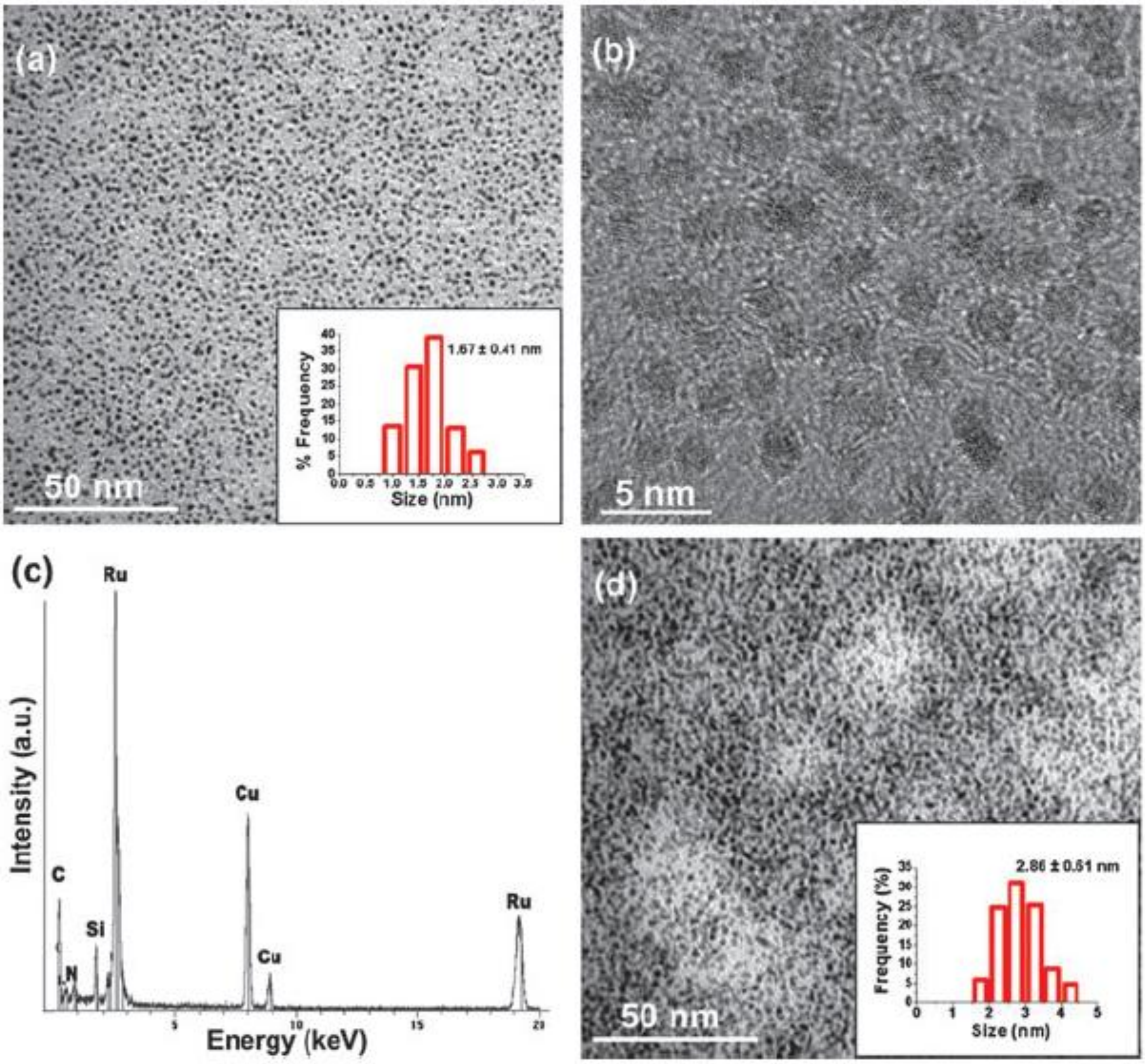

Figure 22. (a) TEM image and corresponding size histogram (inset), (b) high resolution-TEM image and (c) EDS of Ru(0)/APTS, (d) TEM image and corresponding size histogram (inset) of Ru(0)/APTS harvested after the third run of dehydrogenation of DMAB. Reprinted with permission from ref 134. Copyright 2010 Royal Society of Chemistry.

Interestingly, a follow-up works recalculated TOF and TTO values per surface active site on a modified Ru(0)/APTS (1:1) from carbon disulfide CS_2 surface poisoning experiment. The correct values per surface active site were TOF = 11.5 min^{-1} and TTO = 15,500 in the dehydrogenation of DMAB.[28]

More recently, the performances of Ru-based catalysts for hydrolytic DMAB dehydrogenation at RT has been investigated with various supported systems, –with contrasted activity results–, including Ru/graphite, Ru@GO and Ru@GO-PVP in one hand,[135,136] and Ru@Al_2O_3 and Ru/CeO_2 from the other hand[137,138] reporting TOF ranging from 15.0 to 0.8 min^{-1}.

The dehydrogenation of DMAB by using bimetallic systems $Ru_{50}Ni_{50}$@PVP,[139] and $Ru_{60}Pt_{40}$@VC[140] (Vulcan carbon, VC) indicated the superior activity of the alloy incorporating platinum (reported TOF = 7.6 and 249 min^{-1}, respectively). This latter level of activity is notably higher than any other reported systems of this type, and remains to be explained. The fabrication of RuPt NPs supported on VC was carried out using an alcohol reduction process using K_2PtCl_4 and $RuCl_3{\cdot}3H_2O$ mixed with Vulcan carbon and refluxed at 90 °C. The reduction of dispersed Pt(II) and Ru(III) ions into Pt(0) and Ru(0) metallic states was achieved by using DMAB. Spherical nanoparticles of 3.2 ± 0.8 nm were observed. $Ru_{60}Pt_{40}$@VC alloy nanocatalyst provided a better activity than those of Pt and Ru monometallic nanocatalysts prepared by the same method, and retained 64% of its original TOF after the 10th run.

The more rarely investigated hydrolytic dehydrogenation of MeAB,[141] was also reported at RT using a bimetallic $Ru_{50}Rh_{50}$@PVP catalyst prepared following the same alcohol reduction method from a mixture of Rh(III)/Ru(III) salts in the presence of PVP.[142] With an average size of alloyed particles of 3.4 ± 0.3 nm, the nanocatalyst achieved a TOF = 206 min^{-1}, which remained lower than the activity obtained from monometallic Ru nanoparticles prepared by atomic layer deposition on electrospun carbon nanofibers (Ru@CNF, TOF = 563 min^{-1}, Figure 23).[141] Polyacrylonitrile (PAN) was electrospun into bead-free 1D nanofibers by electrospinning. The nanofibers undertaken a carbonization process, and an ozone-assisted ALD technique was employed to grow Ru NPs of 3.4 ± 0.4 nm average size on the CNF support.

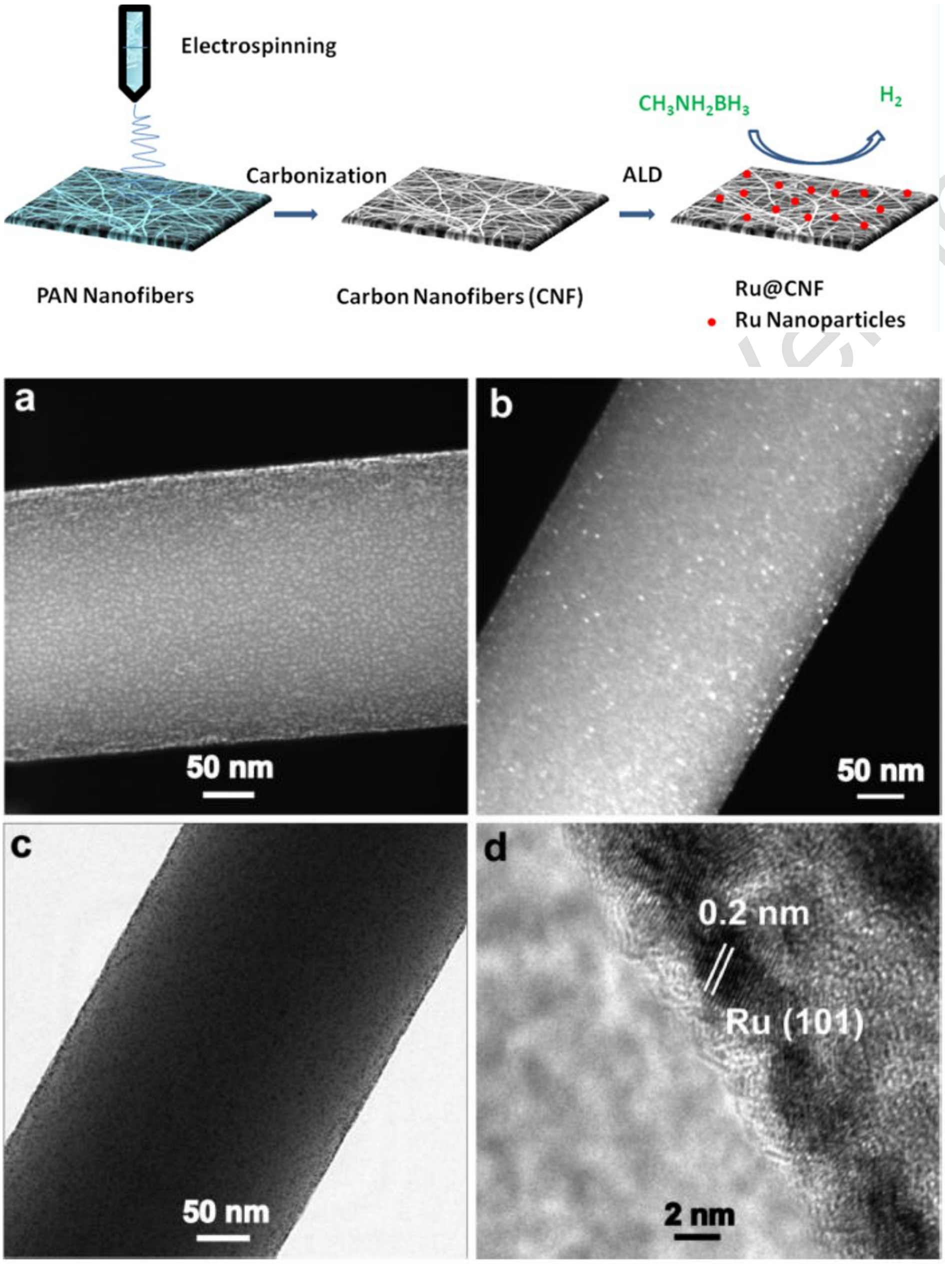

Figure 23. Top: Fabrication of nanocatalysts comprising electrospun carbon nanofiber (CNF) supported ruthenium nanoparticles (Ru@CNF). Bottom: HAADF−STEM (a,b), bright-field TEM (c), and HRTEM (d) images of Ru@CNF. Reprinted with permission from ref 141. Copyright 2018 American Chemical Society.

The ALD reaction chamber was kept at 290 °C with CNFs, and [Ru(EtCp)$_2$] preheated to 100 °C was introduced with reactive O_3 for processing ALD of Ru over a 150 cycles procedure. The BET surface area of 63.4 m^2 g^{-1} for CNF was reduced to 24.5 m^2 g^{-1} for Ru@CNF catalytic material (Ru 0.4% wt%). After achievement of >90% conversion in the first dehydrogenation run, another equiv of MeAB was added to the mixture. The Ru@CNF nanocatalyst conserved 72% of its original catalytic activity at the 5th recycling run. The morphological investigation of the recovered catalyst showed that the fiber morphology was preserved for Ru@CNF while a clumping of the supported Ru NPs was noticed.[141]

Recent extent in the hydrolytic dehydrogenation of DMAB was its utilization in tandem reactions with CO_2 using a Ru-based nanocatalyst (Figure 24) for the *N*-formylation of various amines, and the synthesis of benzimidazoles from aromatic 1,2-diamines (or 2-nitroanilines).[143]

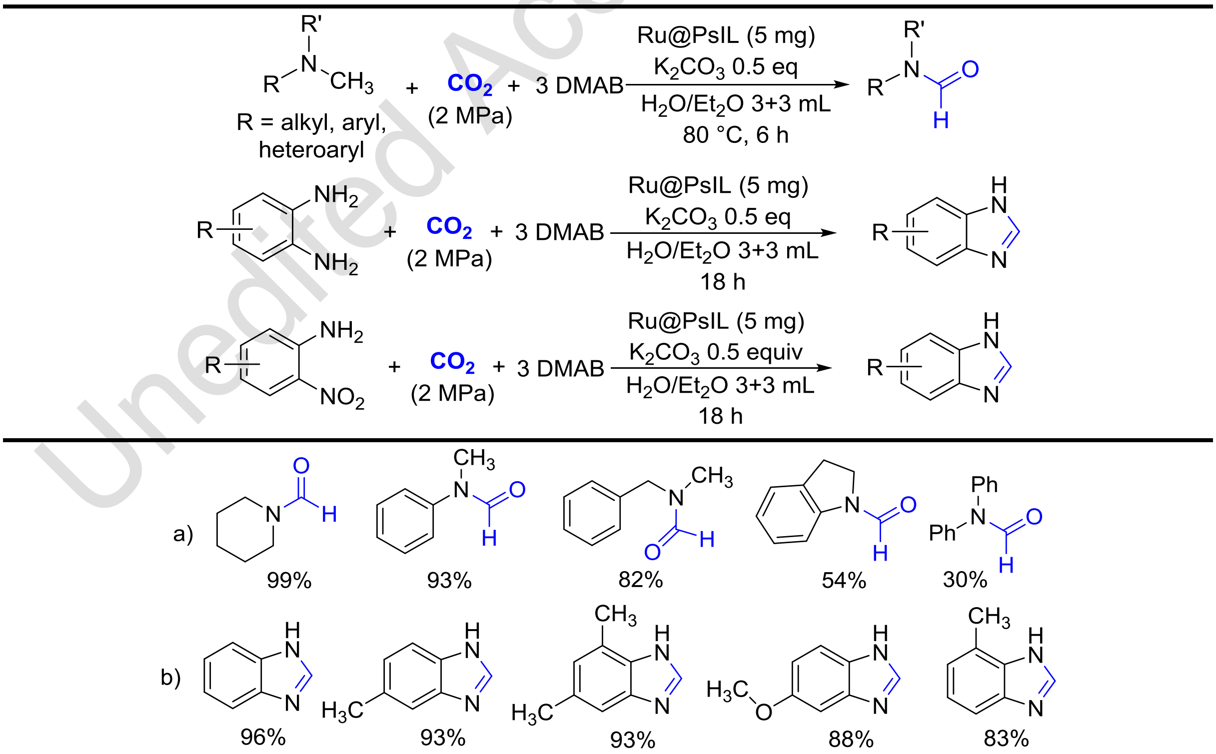

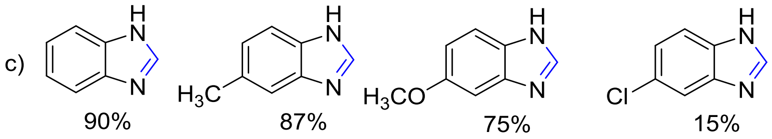

Figure 24. Ru@PsIL catalyzed synthesis of a) *N*-formamides and b), c) benzimidazole by using DMAB and CO_2. Reproduced with permission from ref 143. Copyright 2018 Wiley-VCH Verlag GmbH & Co. KGaA, Weinheim.

For such tandem approach, Ru NPs on a supported ionic liquid phase (Ru@PsIL) were synthesized (Figure 25), with the hypothesis that ionic functional moieties on the solid polymer backbone may enhance the dispersion and stabilization of NPs by providing an electronic environment similar to ILs@NPs.[143] Indeed, ionic liquids (ILs) are known for enhancing stabilization of metal NPs by surface electrostatic interaction.

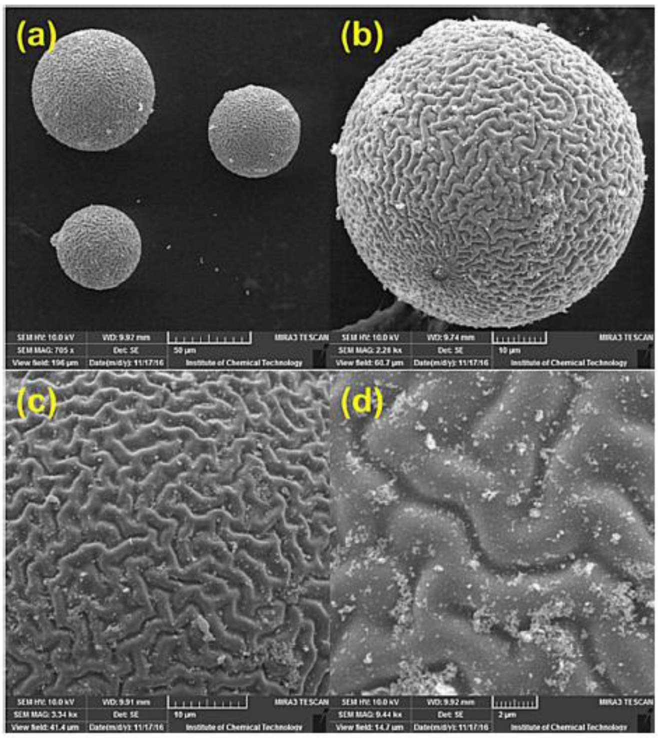

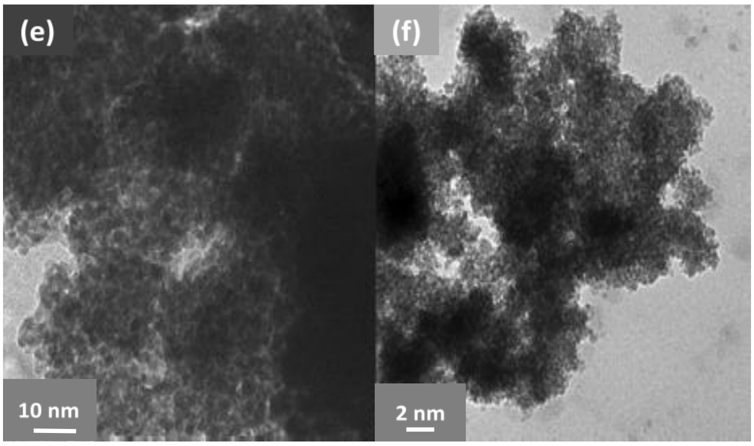

Figure 25. Top: SEM images of Ru@PsIL (a) and (b) showing the spherical morphology with the wrinkled surface of Ru@PsIL, (b) and (c) show the well-stabilized Ru NPs on the wrinkled surface of the PsIL. Bottom: (e) and (f) TEM images of the Ru@PsIL showing the very small Ru NPs stabilized on the support of PsIL. Reprinted with permission from ref 143. Copyright 2018 Wiley-VCH Verlag GmbH & Co. KGaA, Weinheim.

SEM and TEM images of Ru@PsIL showed roughly spherical Ru particle sizing 3-6 nm and dispersed over the spherical wrinkled polymer support surface (Figure 25). Thermogravimetric analysis indicated that as-prepared Ru@PsIL has a thermal stability up to 350 °C. The Ru@PsIL catalyst achieved five recycling run in the formylation of *N*-methyl aniline to *N*-methyl-*N*-phenylformamide with a maximum TOF = 0.9 min^{-1} and a conversion loss from 93% to *ca* 85%. This method using borane constitute a pertinent alternative to CO_2 formylation using pressurized H_2 and silanes.

Similarly to what was investigated with the Pd@RCC3 catalyst (see section 3.2),[100] the methanolysis of AB (see also section 4.1 for related studies) was used as a test reaction for evaluating the catalytic activity of Ru NPs encapsulated in a crystalline porous coordination cage (PCC) as Ru@PCC-2 (NPs average size 2.5 nm, Figure 26, bottom).[144]. PCC-2 cage molecule comprises six tetranuclear cobalt clusters $[Co_4(\mu_4\text{-}OH)]$, six vertex ligands V as vertices, and eight panel ligands L as the faces of an octahedral cage, giving rise to an anionic host $\{[Co_4(\mu_4\text{-}OH)V]_6L_8\}^{30-}$ where each cobalt atom coordinates one sulfonic oxygen, two phenolate oxygen atoms from V, two carboxylate oxygen from L, and a μ_4-OH, leading to a local octahedral coordination environment. On the basis of the crystal structure, the inner cavity dimension of PCC-2 is 2.51 nm at longest, and the diameter of the sphere in which the octahedral cage is inscribed is *ca* 4.2 nm. Hydrogen evolution was initiated by injection of a DMF/MeOH solution of Ru@PCC-2 into a reaction flask containing AB powder at 25 °C. The Ru@PCC-2 (molar ratio 2:1) gave a TOF = 304 min^{-1} that was attributed to the specific fcc crystal faces of particles (presumably exposing more of active sites), and the anionic and soluble nature of PCC-2 that regulates the size and atomic arrangement of the encapsulated NPs (the match between the size of Ru NPs and porosity of PCC-2 suggested a growth regulating action). The catalyst Ru@PCC-2 was reused five times retaining 95% of its initial activity.

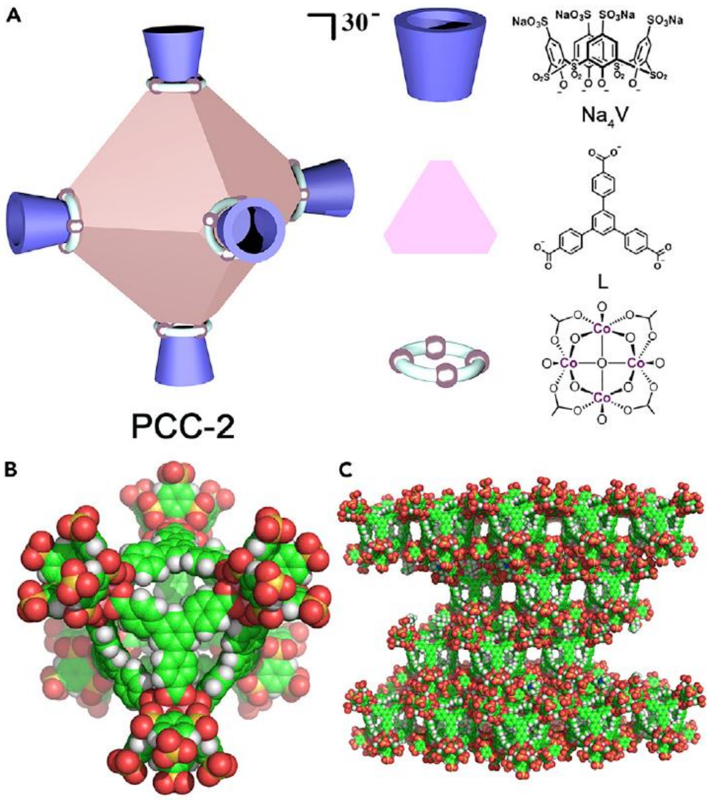

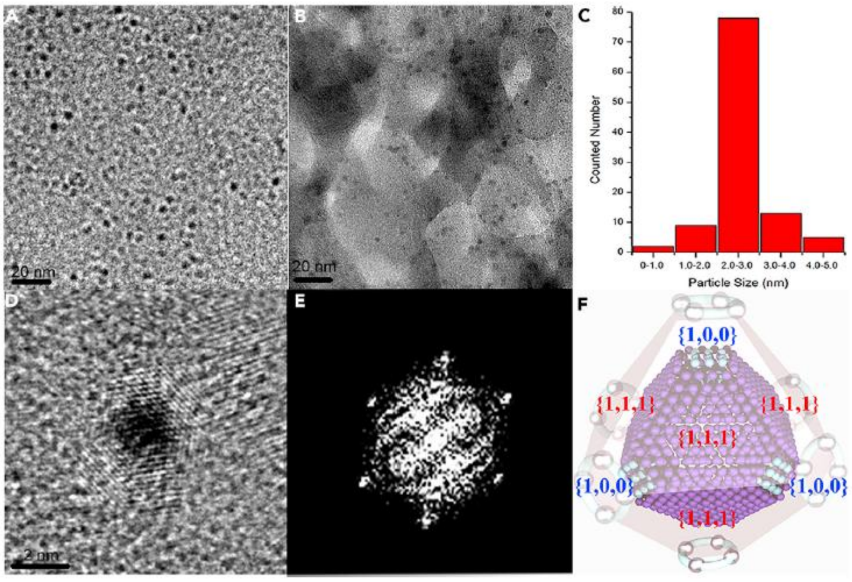

Figure 26. Top: Structure of PCC-2 and its components (A), crystal structure of PCC-2 (B), packing diagram of PCC-2 (C), Bottom: TEM Characterization of Ru@PCC-2: TEM images of Ru NPs@PCC-2 in both solution (A) and solid state (B), size distribution of Ru NPs@PCC-2 (C), HRTEM image of an individual Ru NPs@PCC-2 (D), FFT of d (view direction [110]) (E), and truncated octahedral fcc Ru NPs encapsulated within PCC-2 (V of PCC-2 was omitted for clarity) (F). Scale bars: 20 nm (A and B) and 2 nm (D). Reprinted with permission from ref 144. Copyright 2018 Elsevier Inc.

These results were confirmed by a follow-up work, in which a series of ultra-small sub-2 nm Ru fcc NPs were synthesized via the pyrolysis at 700 °C of a Ru-loaded MOF, using various concentration in Ru.[145] Fcc Ru NPs sizing 1.3 nm exhibited a highest catalytic activity for the methanolysis of AB with a TOF = 336 min^{-1} at 25 °C. The Zr-based multivariate metal-organic frameworks (MTV MOFs) were directly synthesized by a one pot reaction mixing $ZrCl_4$, 2,2′-bipyridine-5,5′-dicarboxylic acid (H_2bpdc), and Ru(bpy)$_2$(H_2bpydc). During the crystallization process, the Ru cations were dispersed over the crystalline UiO-67 framework. In this MTV MOF, the concentration of Ru metal centers was adjusted by tuning the loading molar ratio of H_2bpdc/Ru(bpy)$_2$(H_2bpydc). After a 3 h pyrolysis at 700 °C, the skeleton of the Ru–MOFs was *in situ* transformed into N-doped porous carbon, decorated by ZrO_2 nanocrystals and Ru NPs. By this synthetic method of solid solution pyrolysis, the best catalytic system was formed with a 2.40 mol% in Ru (3.26 wt%) and exhibited a TOF = 336 min^{-1}, while when the Ru content was increased to 4.01 mol% (4.79 wt%) the fcc Ru NPs transformed into hcp phase with a greater size of 2.2 nm, giving a notably lower catalytic activity (TOF = 188 min^{-1}).[145] Besides their size, the structure and geometric effects of the NPs play important roles in improving the catalytic activity. Ru atoms on the NP surface with higher lattice index (fcc) have lower coordination number, which lead to a stronger affinity for binding AB with lower energy needed. The fcc Ru NCs showed accordingly an improved performance in the methanolysis reaction of AB than that of hcp Ru analogs.

The intrinsic degree of activity exhibited by ruthenium, its relative cheapness, and the very diverse methods to disperse it as small and ultra-small (sub-2 nm) nanoparticles, make this metal a particularly attractive option for building mono- and multimetallic systems devoted to dehydrogenation of amine-boranes, both by hydrolysis and alcohol solvolysis. Tandem with organic synthesis taking benefit from ruthenium reactivity with H_2 (hydride formation for instance) are particularly attracting, and should be much further developed in the near future.

3.5. Advances in silver-based and alloys nanoparticle catalysts

The market price for silver in June 2020 was 570 USD kg^{-1}, compared to 550 USD kg^{-1} in 2016 (+3.5%), and 1,000 USD kg^{-1} in 2012 (–50%).[146]

While silver is cheaper than other noble metals, until the report of Ag(0) NPs supported on magnetic SiO_2–$CoFe_2O_4$ *in situ* formed during the hydrolytic dehydrogenation of AB catalysts,[40] the catalysts based on Ag had been found only modestly active for hydrogen production from amine-borane substrates, with TOF below 1.0 min^{-1}.[147,148] The synthesis of various multimetallic composites –including cobalt, nickel and iron– in which either silver or another metal could be dominant, allowed to report TOF below or *ca* 100 min^{-1}.[149,150,151,152,153] The nanocomposite Ag/SiO_2–$CoFe_2O_4$ was synthesized via impregnation-reduction method in water using silver(I) nitrate, $AgNO_3$, and preformed SiO_2–$CoFe_2O_4$, with AB as a reductant.[40] Silver loadings between 0.70 and 3.0 wt% were achieved. The TEM images of the samples showed an aggregation of the 15 nm ill-defined SiO_2–$CoFe_2O_4$/silver nanocomposites, suggesting a dispersion of Ag in the porous crystalline support (BET surface area and total pore volume 138 $m^2\ g^{-1}$ and 0.52 $cm^3\ g^{-1}$ for the support and 135 $m^2\ g^{-1}$ and 0.35 $cm^3\ g^{-1}$ for the composite, respectively). The Ag/SiO_2–$CoFe_2O_4$ composite with Ag loading of 0.98 wt% displayed the best catalytic performance amongst the related systems (Figure 27) with a TOF = 264 min^{-1} for the production of hydrogen from AB hydrolysis. Interestingly, after the hydrolysis process was completed, the catalysts were magnetically separated from the mixture and washed with deionized water for reuse. They retained 100% of their initial catalytic activity in the hydrolysis of AB along seven cycling runs.

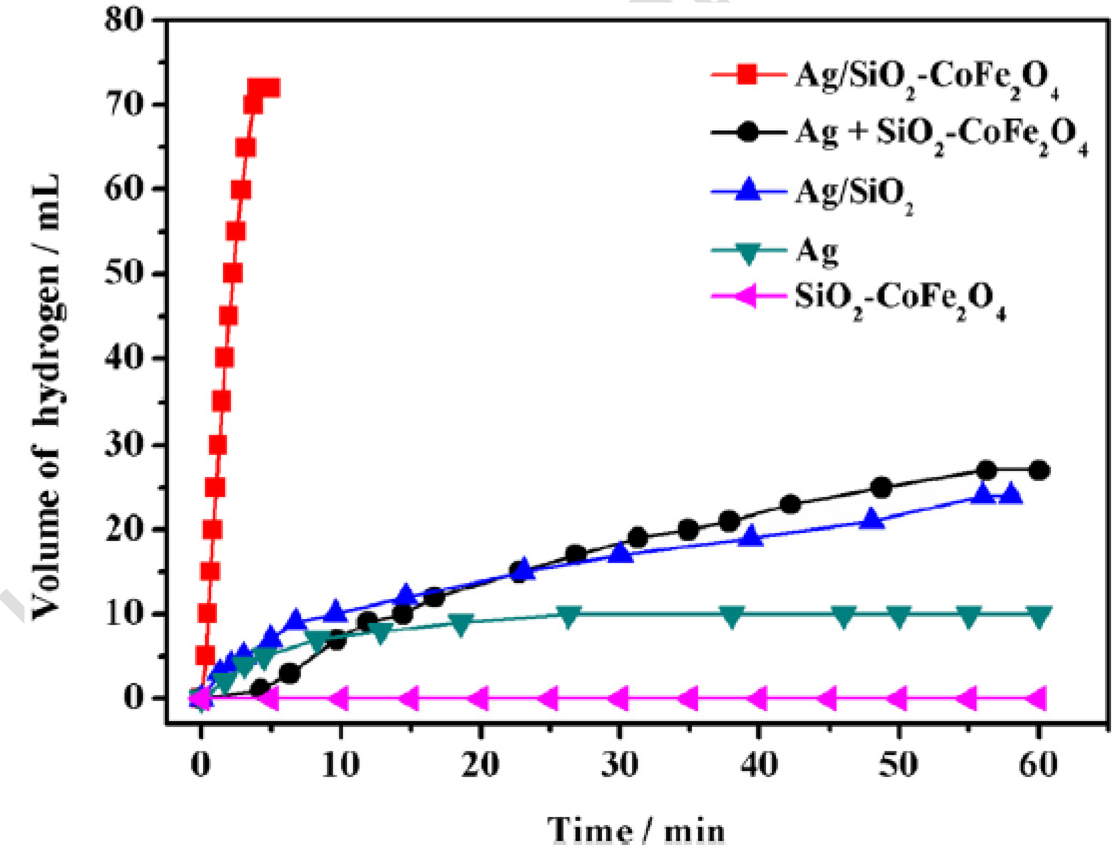

Figure 27. H_2 production from the hydrolysis of AB ([AB] = 100 mM, T = 298 K) in the presence of Ag(0)/SiO_2-$CoFe_2O_4$ NCs, Ag(0), SiO_2-$CoFe_2O_4$, Ag + SiO_2-$CoFe_2O_4$ and Ag/SiO_2 (Ag/AB = 0.0028). Reprinted with permission from ref 40. Copyright 2015 Hydrogen Energy Publications, LLC, Elsevier Ltd.

From an assisted-catalysis perspective, silver nanoparticles gained attention due to their plasmonic properties and catalytic features enhanced under visible-light irradiation.[148,154] In such plasmonic nanocatalysts, silver NPs serve as sensitive optical antennas that may lead to the transformation of solar energy by LSPR where collective oscillations of free-electrons in metal NPs are driven by the electromagnetic field of incident light. Thus, visible-light-responsive plasmonic photocatalysts can combine the deposition of metallic NPs onto suitable semiconductors. Accordingly, Yamashita group described size- and color-controlled Ag NPs (from yellow spherical 4 nm NPs, to blue 9 nm nanorods) that were synthesized within the silica mesopore structure of SBA-15 by microwave-assisted alcohol reduction.[148] The Ag NPs, when used for H_2 production from AB, exhibited the highest catalytic activities (TOF = 0.2 min^{-1}) in the light than in the dark for the smaller Ag NPs. The catalytic performance of Ag/SBA-15 was enhanced by light irradiation in close agreement with the order of absorption intensity of the irradiated light by Ag LSPR. Investigations focused on the thermal effect in catalysis, wavelength dependence, and the effect of a charge scavenger evidenced that the H_2 evolution was assisted by the positive charge generated by charge separation due to Ag LSPR.

Follow-up studies developed Ag-based plasmonic catalyst supported on mesoporous silica with isolated and tetrahedral coordinated single-site Ti-oxide moieties, Ag/Ti-SBA-15, aiming at utilizing the broad spectral range of the solar energy.[154] The catalytic activity of Ag/Ti-SBA-15 in hydrogen production from AB by hydrolysis was twice higher than Ag/SBA-15 without Ti-oxide moieties, both in the dark and under light irradiation. This because of improved electron transfer under light irradiation caused by the creation of heterojunctions between Ag NPs and Ti-oxide moieties. This photocatalytic system, by introducing titanium oxide moieties and plasmonic Ag NPs into the framework of silica, links together Vis-active plasmonic and UV-active single-site photocatalysts (Figure 28).

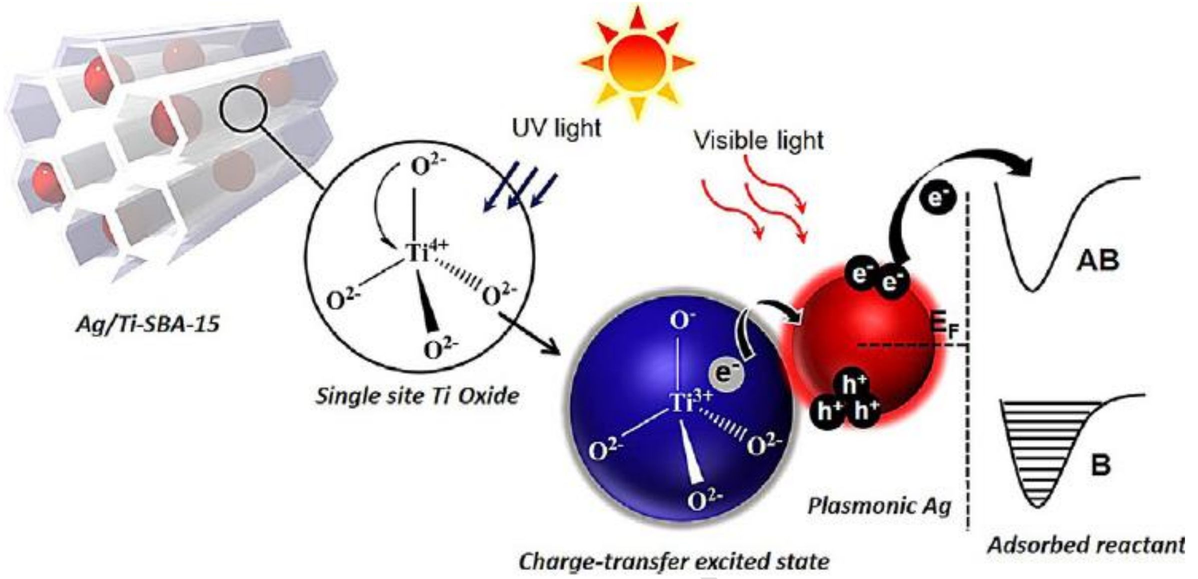

Figure 28. Light-induced charge-transfer pathway on Ag/Ti-SBA-15 under UV and visible-light irradiation (B: bonding AB: antibonding). Reprinted with permission from ref 154. Copyright 2017 Wiley-VCH Verlag GmbH & Co. KGaA, Weinheim.

Interesting fundamental approaches addressed the properties of well-defined ultra small size-selected Ag clusters.[155] A general synthetic method involves the thermal removal of thiolate (RS) or phosphine (R_3P) ligands from ligand-protected size-selected metal clusters. For coinage metals a strong concern is that sulfur remain an impurity after heat treatment forming catalytically inactive nanoparticles. Sulfur-free Ag_{44} clusters were immobilized on mesoporous carbon (MPC) by the calcination of $(Ph_4P)_4[Ag_{44}(SPhF)_{30}]$ at 300 °C for 2 h, 4-(fluorophenyl)thiolate, FC_6H_4S, ligands desorbed in the form of thiol or disulfide upon heating. The $(Ph_4P)_4[Ag_{44}(SPhF)_{30}]$ clusters at a 0.2 wt% Ag loading on MPC (specific surface area of 2300 m^2 g^{-1}) were characterized by X-ray absorption near-edge structure (XANES) and Fourier transformed extended X-ray absorption fine structure (FT-EXAFS) methods. TEM indicated ultra small Ag NPs with a diameter of 1-2 nm dispersed on MPC support. As catalyst, almost no H_2 was produced under a N_2 atmosphere. This low production was caused by the MPC support. Besides the absence of catalytic activity of Ag_{44}/MPC under an inert atmosphere the production of H_2 proceeded conversely in air or under pure O_2. In addition, the reaction was terminated after the production of 1 equiv. of H_2 (Eq. 1), while optimal hydrolytic dehydrogenation of AB commonly proceeds with the formation of 3 equiv. of H_2 (Eq. 2). The decreased production of H_2 is obviously detrimental from the viewpoint of utilizing AB as a full H_2 production storage material, but this result suggests that the dehydrogenation mechanism with Ag_{44}/MPC is different from other current metal nanoparticle systems. A mechanism explaining O_2 involvement was proposed following the water-free route.

$$H_3N.BH_3 + O_2 \longrightarrow NH_4^+ + BO_2^- + H_2 \qquad \text{(Eq. 1)}$$

$$H_3N.BH_3 + 2H_2O \longrightarrow NH_4^+ + BO_2^- + 3H_2 \qquad \text{(Eq. 2)}$$

Recent studies addressed the use of an Ag(0) nanocatalyst stabilized within hydrogel networks of *p*-sulfopropyl acrylate potassium-co-2-acrylamido-2-methylpropansulfonic acid sodium salts, Ag@SPA-co-AMPS, which was used for H_2 production from ethylenediamine bisborane (EDAB, $H_3B \leftarrow NH_2(CH_2)_2NH_2 \rightarrow BH_3$) (see also section 4.2 for EDAB as H_2 storage material).[156] Ag(I) ions were adsorbed into the networks of the SPA-co-AMPS using dry SPA-co- AMPS left into $AgNO_3$ solution in deionized water at RT in the dark for 24 h. After hydrogel filtration, Ag(I) adsorbed on SPA-co-AMPS were reduced into Ag(0) NPs from $NaBH_4$ addition. Ag@SPA-co-AMPS for use in catalytic experiments was used by fragmenting without drying. The Ag(0) nanoparticles supported by the SPA-co-AMPS have a large distribution of spherical form in the 20 to 100 nm range. Hydrogen production from EDAB was achieved at a TOF = 0.56 min^{-1} at 30 °C, and conserved 95% of its catalytic activity during the 5th use.

Overall, the catalytic activity for H_2 production from amine-boranes of silver-based nanoparticle systems still need to be exalted, especially in comparison with the existing best active systems. Nevertheless, the plasmonic properties of the NPs of this element, possibly combined with other metal or pertinent support, may lead to valuable photocatalytically assisted-dehydrogenation systems and the conception of alternatives to mainstream approaches.

3.6. Advances in cobalt-based and alloys nanoparticle catalysts

The market price for cobalt with >99.8% purity was 33 USD kg^{-1} in June 2020,[157] compared to *ca* 25 USD kg^{-1} in 2016 (+32%) and 30 USD kg^{-1} in 2012 (–16%).[158] In the forthcoming years demand for refined cobalt is expected to increase from 50,000 t a^{-1} (tons per annum, 2007) to 110,000 t a^{-1} in 2030 and 190,000 t a^{-1} in 2050.[158]

Supported cobalt nanocatalysts, among other non-noble metal-based dispersed nanoparticles, were early on detected by Xu group as a possible choice for total hydrolysis of AB towards H_2 evolution at RT with reasonably fast kinetics.[30] The hydrogen production rates from aqueous AB were found to be almost the same in the presence of 10 wt% metal Co/γ-Al_2O_3 and Co/SiO_2, whereas the Co/C catalyst exhibited higher catalytic activity because of smaller particle size (2.5 nm *vs.* 12.0-13.0 nm for Co on oxide supports) and a larger surface area (270 m^2 g^{-1} *vs.* 52-57 for oxide supports). Conversely, commercial Co powders with micrometric particle sizes were found to be inactive for AB hydrolysis. A number of monometallic Co-based catalytic systems have been then reported,[15,18,64,159] from which the highest activity reached up TOF about 40-50 min^{-1}.[160,161,162,42] Based on the expected promoting role of capping ligands on metal NPs, including charge transfer, surface crowding effect, molecular recognition, chiral modification, and adsorption regulation, amine-rich polyethylenimine (PEI)-capped Co NPs (average diameter 2.6 nm) were deposited on GO.[161] The resulting Co/PEI-GO composites was used for hydrolytic dehydrogenation of AB at 25 °C, and achieved a TOF = 39.9 min^{-1}, retaining about 65% of its initial activity at a 5th recycling run. A covalent triazine framework (CTF, pore size of 1.5 nm and surface area *ca* 950 $m^2\ g^{-1}$) was used as an electron-donating porous support to favor the activation of B–H and N–H bonds in AB hydrolysis by breaking of an O–H bond in H_2O. This latter was indeed suggested as the rate determining step by kinetic isotope effect investigations.[162] CTF supported Co (Co/CTF) exhibited a mean Co nanoparticle size of 3.3 nm. Since CTF was microporous with a pore size of *ca* 1.5 nm, most of the Co nanoparticles mainly stayed on the edges of the pores and blocked some channels, consistent with a decrease of material surface from 947 to 726 $m^2\ g^{-1}$ after Co loading. The composite Co/CTF (3 wt% Co) catalyzed AB hydrolytic dehydrogenation at 25 °C with a TOF = 42.3 min^{-1}.

A gap in activity was hurdled by encapsulating cobalt small nanoparticles in soluble porous coordination cages (PCCs),[163] like it was reported for ruthenium particles (details in section 3.4)[144]. The size distribution of Co NPs in Co@PCC was *ca* 2.5 nm (crystalline fcc type, Figure 29), which indicated that the formed Co NPs were size-regulated by PCC, for which this size was established as a minimal dimension of internal cage cavity. For the hydrolytic dehydrogenation of AB, Co@PCC (7% Co) achieved a TOF = 90.1 min^{-1}.

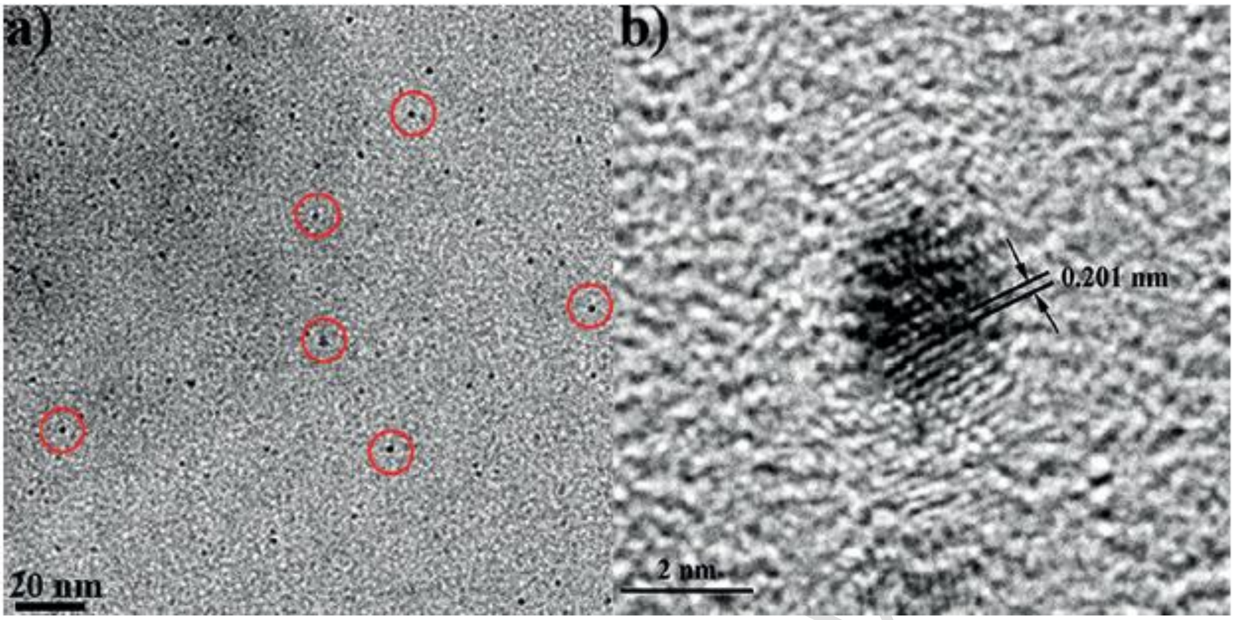

Figure 29. a) TEM images of Co NCs@PCC-2a (red cycles indicate single NCs). b) HRTEM image of single NC of Co NCs@PCC-2a showing the (1,1,1) crystal surface. Reprinted with permission from ref 163. Copyright 2018 Wiley- VCH Verlag GmbH & Co. KGaA, Weinheim.

Beside the activity progress achieved using monometallic Co NPs systems for AB hydrolytic dehydrogenation, investigation also met success with further developing magnetic,[164] tandem-reactive,[165] and photocatalytic systems.[166,167,168]

Co(0) NPs supported on ceria (Co/CeO_2) were prepared from the reduction of $CoCl_2$ previously impregnated on the surface of ceria nanopowders.[164] The Co/CeO_2 composite (2 wt% Co) incorporated cobalt nanoparticles with sizes in the 3.5-6.0 nm range, magnetically separable and reusable as catalyst in hydrogen production from the hydrolysis of AB. After the 5th use the material retained its initial catalytic activity with a TOF = 7.0 min^{-1}. Comparatively, 2 wt% non-noble metal analogs Ni(0)/CeO_2 and Cu(0)/CeO_2 achieved TOF = 1.7 min^{-1} and 1.5 min^{-1}, respectively, while Fe(0)/CeO_2 was catalytically inactive.

A functionalized microporous polymer monolith (MPM) formed by polyalkyne synthesis form Sonogashira coupling was decorated with triazole groups, which were further used as coordination sites for Co(II) ions for *in situ* further reduction to Co(0) NPs.[165] This sponge-like compressible Co-MPM consisted of fiber bundles decorated with spherical particles on the micrometer scale. Co-MPM promoted the reaction of dehydrogenation of AB in tandem with hydrogenation of nitrobenzene and 4-nitroaniline into the corresponding amine. Curiously, better results are obtained under compression/release mechanical process, presumably because of a facilitated interfacial contact between the reactants and active sites.

Co-based bimetallic photocatalysts were also studied for AB hydrolysis at RT. For controlling the visible light-driven activities of the catalysts containing metal nanoparticles, the tuning of semiconducting supports has been intensively studied. Co and Ni nanoparticles were deposited on different microstructures of carbon nitride (C_3N_4) for promoting photocatalytic H_2 evolution from AB at RT with a TOF = 93.8 min^{-1}.[166] The post-synthetic heat treatment modification approach to prepare carbon nitride C_3N_4 brought about the increased specific surface area, improved light absorption, and upgraded electron/hole separation along with electron-transfer efficiency in photocatalysts.

Semiconductors with narrow bandgaps and porous nanosheet structures have also been recently tested to support Co NPs. The purpose in this work was to tune and enhance the electron density under visible light irradiation to result in enhanced H_2 evolution rate from AB hydrolysis reaction.[167] Porous V_2O_5 nanosheets with oxygen vacancies were selected as semiconducting supports. They achieved transfer of photo-generated electrons to metal NPs with the help of a built-in electric field, allowing the electron density of Co NPs to be tuned and enhanced. Nanosheet-like V_2O_5 was prepared by calcining NH_4VO_3 at 500 °C. The thermal treatment of such nanosheets at 250-350 °C under a H_2/Ar atmosphere for O-vacancy production led to the formation of modified V_2O_5 species. As porous nanosheet structures presumably featured good carrier mobility, surface area, and abundant surface active sites, systematic investigations showed that all the catalysts formed (Co- and Ni-based) had higher activities under visible light irradiation than in the dark (TOF = 35.5–37.8 min^{-1} in the dark). Co/V_2O_5-(300 °C) exhibited the highest photocatalytic activity with a TOF = 120 min^{-1}.[167] From a catalyst structural characterization view, the morphology of Co NPs could unfortunately not be clearly distinguished, and mainly the XPS data suggested the presence of metallic Co species.

Photoactive layered double hydroxides (LDHs), as ionic layered clay compounds composed of a positively charged 2D brucite-like layer and exchangeable anions in interlayer space, were also used as support for promoting Co-photocatalyzed hydrolytic dehydrogenation of AB at 25 °C.[168] In comparison with H_2 evolution activity in the dark, a Co/CoFe–C LDH catalyst exhibited a *ca* twice improved photocatalytic H_2 evolution activity with a TOF = 77.6 min^{-1}. A TOF up to 113 min^{-1} was achieved along with enhancement of the light absorption and electron-hole separation induced by molybdate ions intercalated into LDH Co/CoFe–Mo (Figure 30, cobalt 10 wt%, NPs average size 7.3 nm, BET of LDH support increased from molybdate ions intercalation from 40-47 to 55 $m^2\ g^{-1}$).

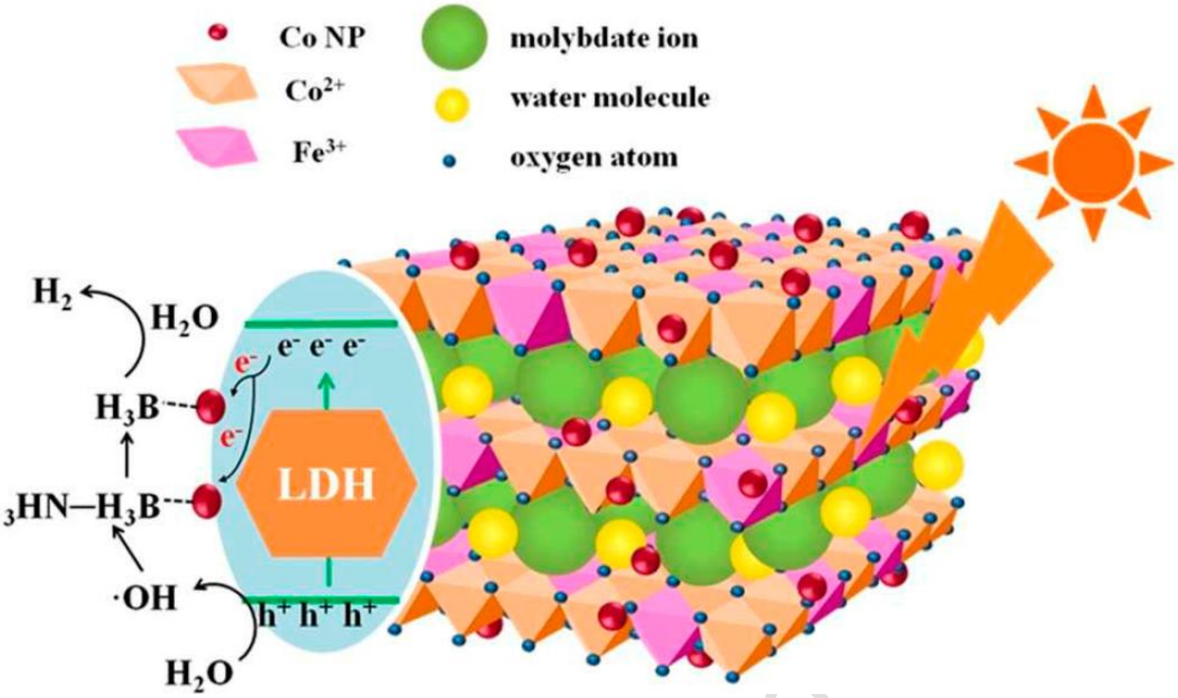

Figure 30. Proposed mechanism for photocatalytic H_2 evolution from AB over Co/CoFe-Mo under visible light irradiation. Reprinted with permission from ref 168. Copyright 2020 Wiley- VCH GmbH.

H_2 evolution rate from AB increased linearly with increased light intensity.[168] For Co/CoFe–Mo, about 46%, 56%, 63% and 69% of the photocatalytic activity contribution came from the incident light intensity increase from 200, 300, 400 to 500 mW cm^{-2} (photothermal heating effect[116] was not discussed). The photocatalysts retained TOF values of 44.1 (39%) and 27.8 min^{-1} (36%), for Co/CoFe–Mo and Co/CoFe–C in the 20th catalytic cycle, respectively. The catalytic activity decrease was ascribed to agglomeration of Co NPs and contamination with boron residue.

An ultrasound-assisted synthesis led to MOF MIL-101-supported amorphous CuCo (2.5 nm average size, and Cu 0.36 wt%, Co 5.67 wt%), FeCo and NiCo NPs with respectively TOF = 51.7, 50.8, and 44.3 min^{-1} in hydrolytic AB dehydrogenation at RT.[42] Crystalline monometallic Co NPs with size of 4.5−8.5 and 14.5−24.5 nm had lower activities with TOF = 9.9 and 4.5 min^{-1}, while amorphous Co NPs with size of 1.6−2.6 and 13.5−24.5 nm exhibited

TOF = 51.4 and 22.3 min^{-1}, respectively. These size and crystallinity important issues fully correlated a seminal report from Xu group –on unsupported amorphous Co NPs, less than 10 nm size, which achieved TOF *ca* 47 min^{-1}, approximately 15 times higher than that of the crystallized one–.[160]

For synthesizing bimetallic nanoparticles active for AB hydrolysis, the alloying of cobalt with noble metals –Ru[169] and Au[170] – or non-noble metals –Ni[171] and Cu[172]– was the subject of early on studies.

A series of surfactant-free bimetallic Co–Au nanoparticles immobilized on amine-functionalized carbon nanotubes (CNTs) have been prepared using three synthetic methods and then used as catalysts for hydrolytic dehydrogenation of AB.[170] The alloy $Co_{88}Au_{12}$@CNT catalyst prepared *in situ* from AB reduction achieved a highest TOF = 36.1 min^{-1} at 25 °C, superior to core-shell Au/CoAu@CNT catalysts and alloy *ex situ* prepared from reduction with $NaBH_4$. The association with ruthenium in a core–shell nanoparticle catalyst supported on carbon black Ru_9@Co_{91}/C, –also formed from *in situ* synthesis using AB as reductant in a one-step co-reduction at RT–, achieved a fairly similar activity with a TOF around 30 min^{-1} (assumed to be 320 min^{-1} based on Ru only).[169] This performance was recently improved by the synthesis of CoRu alloy nanoparticles supported on porous nitrogen-doped graphene layers ($Co_{80}Ru_{20}$@N-C) via pyrolysis of metallo-organic precursors N-bis(salicylidene)ethylenediaminocobalt(II) and tris(2,2′-bipyridyl)ruthenium(II) chloride hexahydrate (Figure 31).[173] $Co_{80}Ru_{20}$@N-C with highest activity contained a Ru content of 5.1 wt% and 10.3 wt% for Co. $Co_{80}Ru_{20}$@N-C catalyzed the hydrogen evolution reaction and AB hydrolysis with an initial TOF = 458 min^{-1} under ambient conditions, and retained 96% of this activity after 5 cycling runs. The activity of $Co_{80}Ru_{20}$@N-C was related to its surface area of 257.2 m^2 g^{-1} with mesopores of *ca* 4.5 nm. However, TEM analysis evidenced NPs of average size around 20 nm diameter.

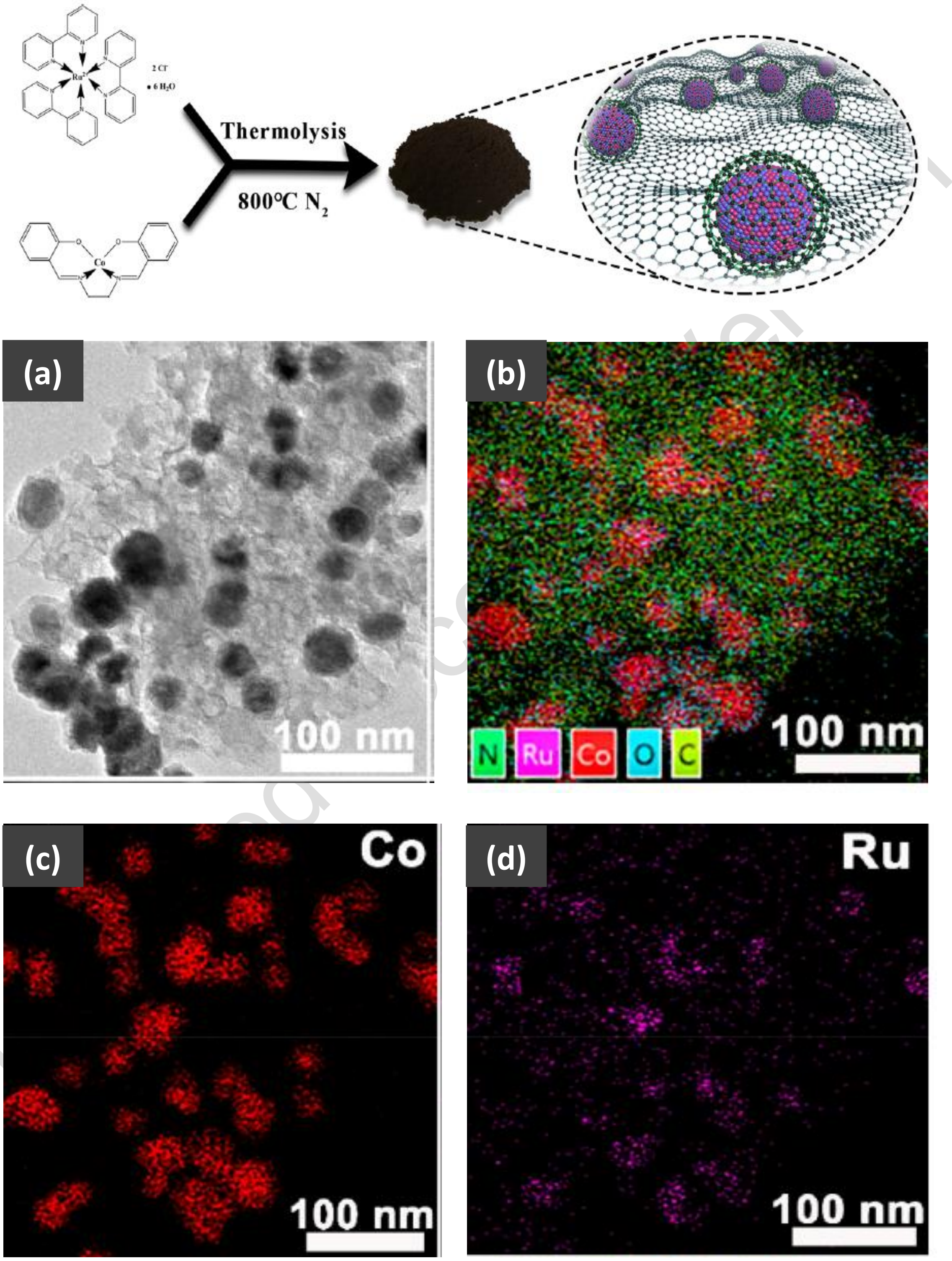

Figure 31. Top: Evolution processes from precursors to Co_xRu_y@N-C, Bottom: (a) TEM images of $Co_{80}Ru_{20}$@N-C, (b−d) HAADF-STEM and the corresponding EDS elemental mapping images of $Co_{80}Ru_{20}$@N-C. Reprinted and reproduced with permission from ref 173. Copyright 2019 American Chemical Society.

The elemental mapping images indicated a distribution of Co and Ru within the inner particles, surrounded by elemental N and C, suggesting that CoRu NP alloys were formed and encapsulated within N-doped graphene.[173] The significantly increased activity for AB dehydrogenation of $Co_{80}Ru_{20}$@N-C was attributed to synchronous activation of B−H and O−H bonds, where Ru atoms are active sites for the activation of B−H bonds. This activation provides active adsorption hydrogen atoms on the catalyst surface. The Co and O atoms nearby both are active sites via hydrogen bonding and acidic sites of Co atoms to activate O−H bonds from water promoting adsorption hydrogen atoms and OH radicals on the catalyst surface. Close contact between Ru and Co atoms in the alloy was assumed. This double activation process would take place in a very close space at catalyst surface, constituting a form of synergetic activation process.

Concerning Co association with non-noble metals, graphene support was also used early on for supporting magnetically recyclable bimetallic $Co_{100}Ni_{100-x}$ (x = 10, 30, 50, 70, 90) nanoparticles.[171] These have been produced from *in situ* one-step procedure, using the mixture $NaBH_4$ and MeAB as reducing agent at RT. The performances for catalytic hydrolysis of amine-boranes were dependent on the composition of the NPs. The bimetallic $Co_{90}Ni_{10}$/graphene alloy catalyst (NP average size 6.2 nm, 13.3 wt% metal) exhibited the highest catalytic activity toward hydrolysis of AB with a TOF = 16.4 min^{-1} at 25 °C. The as-prepared $Co_{90}Ni_{10}$/graphene catalysts retained 44% and 70% of their initial catalytic activity in the hydrolysis of AB and MeAB, respectively, in the 5th cycling run.

Consistently, the bimetallic $Co_{70}Ni_{30}$ nanoparticles that were supported on multiwall carbon nanotubes (MWCNTs) –giving smaller CoNi alloy nanoparticles (2.2 ± 0.4 nm average diameter dispersed on MWCNTs surface, Figure 32, 10.2 wt% metal)– achieved a twice higher activity with TOF = 33.0 min^{-1} at 30 °C.[174] Modification of the support for graphene-like titanium carbide [$Ti_3C_2(OH_xF_{1-x})_2$] allowed to prepare bimetallic $Co_{70}Ni_{30}$ NPs (size of 2.8 nm) catalyzing hydrolytic AB dehydrogenation with a TOF = 39.1 min^{-1} at 30 °C.[175]

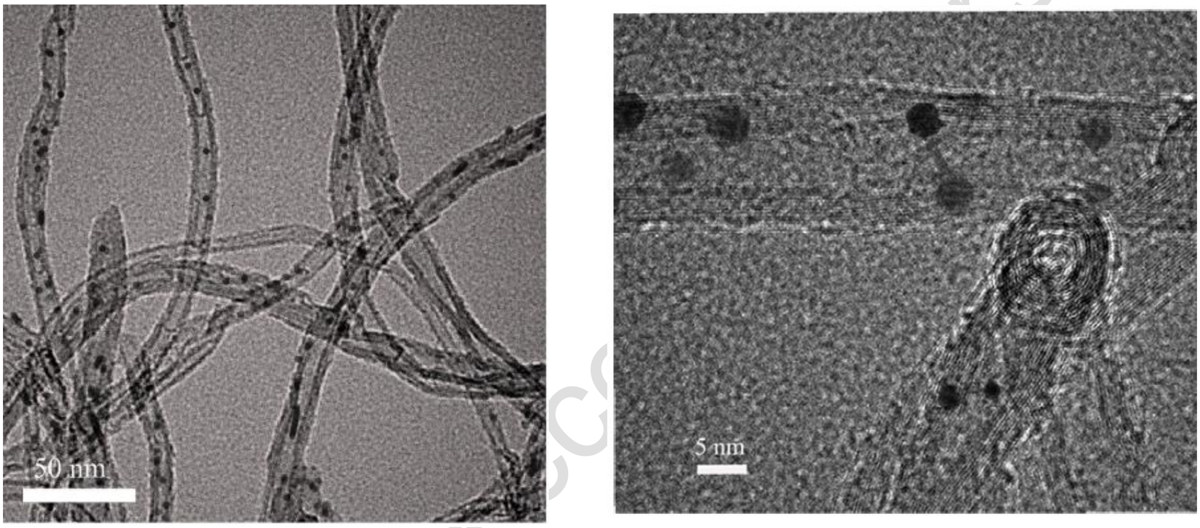

Figure 32. TEM (left) and HRTEM (right) images of CoNi NPs/MCNTs. Reprinted with permission from ref 174. Copyright 2017 Elsevier B.V.

Advances in the use of these cobalt-rich CoNi bimetallic nanoparticles were achieved with the preparation of $Co_{67}Ni_{33}$ alloy NPs embedded on Al_2O_3 nanosheets, from thermal treatment at 650 °C of preformed layered double hydroxides by Ni^{2+}, Co^{2+} ions hydrolyzed in an alkaline solution of urea, and co-precipitated with Al^{3+}.[176] The morphology of $Co_{67}Ni_{33}/Al_2O_3$ shown a 2D sheet architecture (Figure 33, SEM a) of several hundred nanometers in size, and *ca* 5.5 nm in thickness, supporting irregular CoNi alloy nanoparticles of *ca* 6 ± 1 nm (Figure 33, TEM b) and c)). $Co_{67}Ni_{33}/Al_2O_3$ catalysts exhibited a TOF = 34.5 min^{-1} at 25 °C, which was advantageously used for the subsequent tandem hydrogenation reaction of nitroaromatics to aromatic amines with fast nearly quantitative conversion and selectivity >99% (Figure 33, bottom). Notably, a variety of useful functions were tolerated on the nitroaromatic substrate. Theoretical simulations suggested that alloy CoNi structure promotes the rate-determining step of AB hydrolysis and optimizes the adsorption property for the intermediates to further promotes the selective reduction of nitroaromatics toward amines. The catalyst was magnetically recycled along 12th runs and conserved about 50% of its initial TOF at this point.

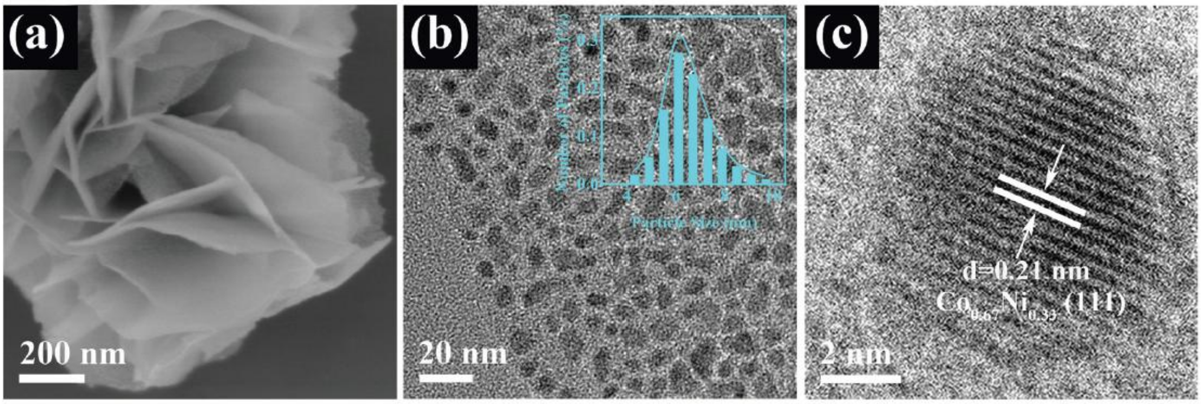

$$R-NO_2 \xrightarrow[\text{MeOH/H}_2\text{O, AB, 50 °C}]{Co_{67}Ni_{33}/Al_2O_3} R-NH_2$$

Entry	Substrate	Product	Yield (%)	Time (min)
1	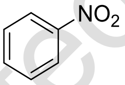	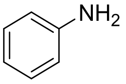	>99	15
2	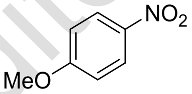	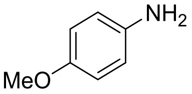	>99	5
3	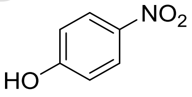	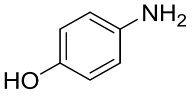	>99	6
4	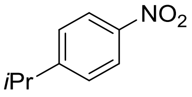	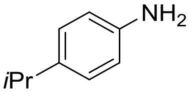	>99	6
5	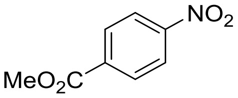	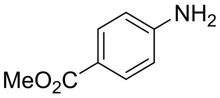	>99	15
6	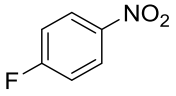	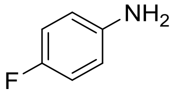	>99	20

7	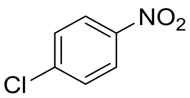	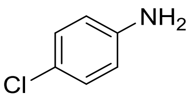	>99	25
8	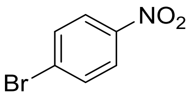	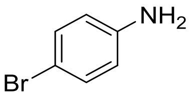	>97	30

Figure 33. Top: (a) SEM and (b) TEM images and inset image of the particles size distribution for $Co_{67}Ni_{33}/Al_2O_3$. (c) HRTEM image confirming formation of a discrete CoNi alloy NPs. Bottom (Table): $Co_{67}Ni_{33}/Al_2O_3$-catalyzed tandem reaction of various R–NO_2 compounds. Reprinted and reproduced with permission from ref 176. Copyright 2019 Royal Society of Chemistry.

A comparable range of activity for hydrolytic hydrogenation of AB was initially reported for bimetallic cobalt association with copper.[172,177] Ultra-small $Co_{70}Cu_{30}$ alloy nanoparticles were encapsulated into the pores of MIL-101 ($Co_{70}Cu_{30}$@MIL-101, mean diameter 2.0 ± 0.4 nm, specific surface 2125 m^2 g^{-1}) using impregnation of the metal precursors $CoCl_2$ and $Cu(NO_3)_2$ by the DSA (previously achieved to Pt catalysts, see section 3.3)[107,92] and further reduction. Using $Co_{70}Cu_{30}$@MIL-101, AB hydrolysis reaction was completed with a TOF = 19.6 min^{-1}.[172] The preparation of bimetallic Co/Cu nanocatalysts supported on poly(diallyldimethylammoniumchloride)-functionalized halloysite nanotubes (PDDA-HNTs, tubes refined from clay minerals) by a deposition-reduction technique allowed to form a $Co_{50}Cu_{50}$/PDDA-HNTs (2.2 nm average size) catalyst with a maximum TOF = 30.8 min^{-1} for AB hydrolysis at RT.[178]

Recent studies also addressed interesting issues, like a more systematic approach of the evaluation of performances for bimetallic alloying Co, Cu and Ni via a ternary diagram (Figure 34).[179] Dual combination of Co, Ni and Cu metals were joined to synthesize unsupported NPs as a catalyst for hydrolytic dehydrogenation of AB and H_2 production. Nine nanosized catalysts at different dual combinations were prepared by using a nitrate combustion modified sol-gel procedure. Structural characterizations were performed and activity tests were completed to compare the performances. $Co_{50}Cu_{50}$ NPs catalyst showed superior activity with TOF = 10.6 min^{-1}. Each of the three corners of the ternary diagram represented one of the three H_2 production rates over the monometallic Co, Cu and Ni NPs.[179] Dark-claret red marks on the side of the ternary diagram indicated the maximum dehydrogenation rates. Dehydrogenation rates were lower for the $Co_xNi_{(1-x)}$ and $Cu_xNi_{(1-x)}$ dual combination with increasing of the Ni content. Ni containing NPs were less reactive whereas Co-containing NPs were more. Fastest values in the ternary plots shifted to higher concentrations of Co for NPs with a Cu content below 50% molar. The hydrogen production rate stayed nearly constant for Co/Cu NPs with a cupper content ≤ 50%. Overall, the catalytic activities of all $Co_xCu_{(1-x)}$ were higher than analogous $Co_xNi_{(1-x)}$ and $Cu_xNi_{(1-x)}$. This pertinent study possibly provides a unique comparison approach of what could be the "intrinsic" activity of monometallic non-noble nanocatalysts and the effect of their alloying.

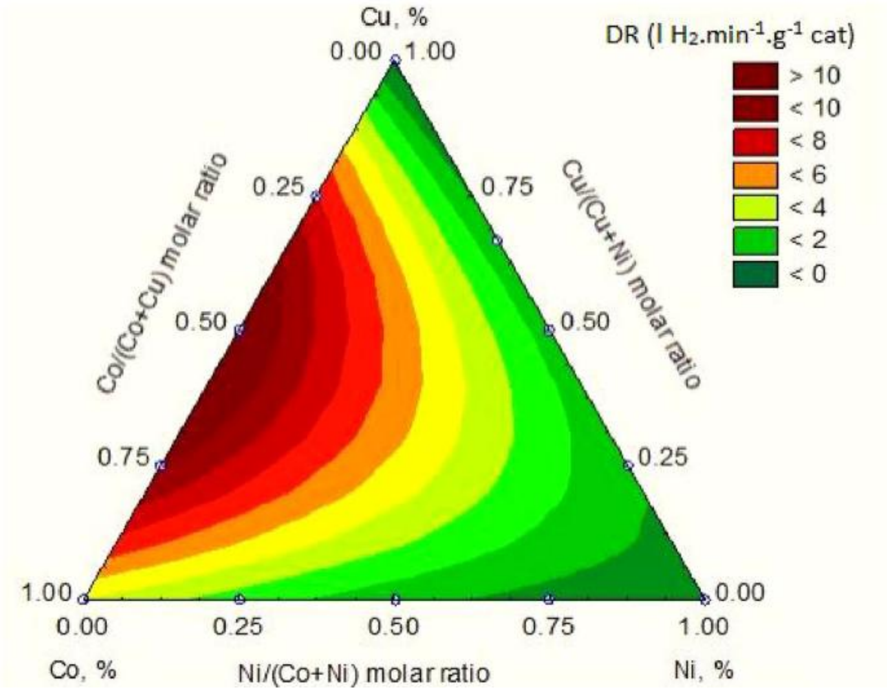

Figure 34. Ternary graph of dehydrogenation rates (DR) with the value range of volume of H_2 produced (l H_2 min^{-1} g^{-1}_{cat}) in the presence of dual combining transition metal hybrid nanoparticles (5 mg catalyst) at 60 °C. Reprinted with permission from ref 179. Copyright 2017 Elsevier B.V.

A related approach concerned the preparation of unsupported bimetallic Co_{50}/M_{50} non-noble metal alloy nanoparticles (M = Fe, Ni, Cu, and Zn, amorphous NPs about 16-20 nm) – from *in situ* reduction with $NaBH_4$ of mixture of $CoCl_2$ and MCl_2 in water– that was achieved for AB hydrolysis catalysts comparison.[180] The electronic structure were examined and compared for the various alloys –by their valence band spectrum (VBS) obtained from XPS, and theoretical calculations–. The d-band center (εd band in eV) and TOF as an activity measurement for catalytic AB hydrolysis were found to be correlated: these values for Co/Cu alloys were superior to all other alloys ($Co_{50}Cu_{50}$ measured εd value was −3.92 eV for TOF = 2.9 min^{-1}). This correlation was attributed to the electronic structure (characterized by εd) of NPs that affected the surface adsorption and desorption behavior of water in the AB hydrolysis reaction. In addition, an acid etching method helped forming new catalyst, SCo/Cu, with different Cu content (Figure 35). The existence of surface defects could moreover further modify εd and tune the rate of AB hydrolysis.[180] Thus, the specific surface area of the acid-etched catalyst increased from 72 $m^2\ g^{-1}$ (Co/Cu) to 175 $m^2\ g^{-1}$ (SCo/Cu), and the particle average size decreased from *ca* 16.2 nm to 6.7 nm, while experimental measured εd value shifted to −3.90 eV and TOF reached 5.7 min^{-1} in a 198% increase.

Figure 35. Schematic illustration of the fabrication strategy of the SCo/Cu Alloy. Reprinted with permission from ref 180. Copyright 2020 American Chemical Society.

A recent promising approach for innovative nanocomposites exploitation in hydrolytic AB dehydrogenation is the synthesis of oxides,[181,182] phosphides,[183,184] and borides,[185] bi- or monometallic cobalt catalysts. Inspired by $CuMoO_4$ and $CoMoO_4$ materials, known in the literature as supercapacitor and anode materials for lithium-ion batteries, and CoCu nanoalloys known as active catalysts for AB hydrolysis, the molybdenum oxide bimetallic $Co_xCu_{1-x}MoO_4$ microsphere catalysts were formed from hydrothermal treatment at 165 °C of dispersion of $CoCl_2$, $CuCl_2$, and molybdic acid into aqueous urea solution.[181] As-prepared, the nanocomposite $Co_xCu_{1-x}MoO_4$ consists of microspheres with diameter of 3−5 µm and BET surface area ranging from 14.5 to 36.8 $m^2\ g^{-1}$, composed of nanoplatelets with an arrangement radiating from the center of the microsphere (Figure 36 for $Co_{80}Cu_{20}MoO_4$).

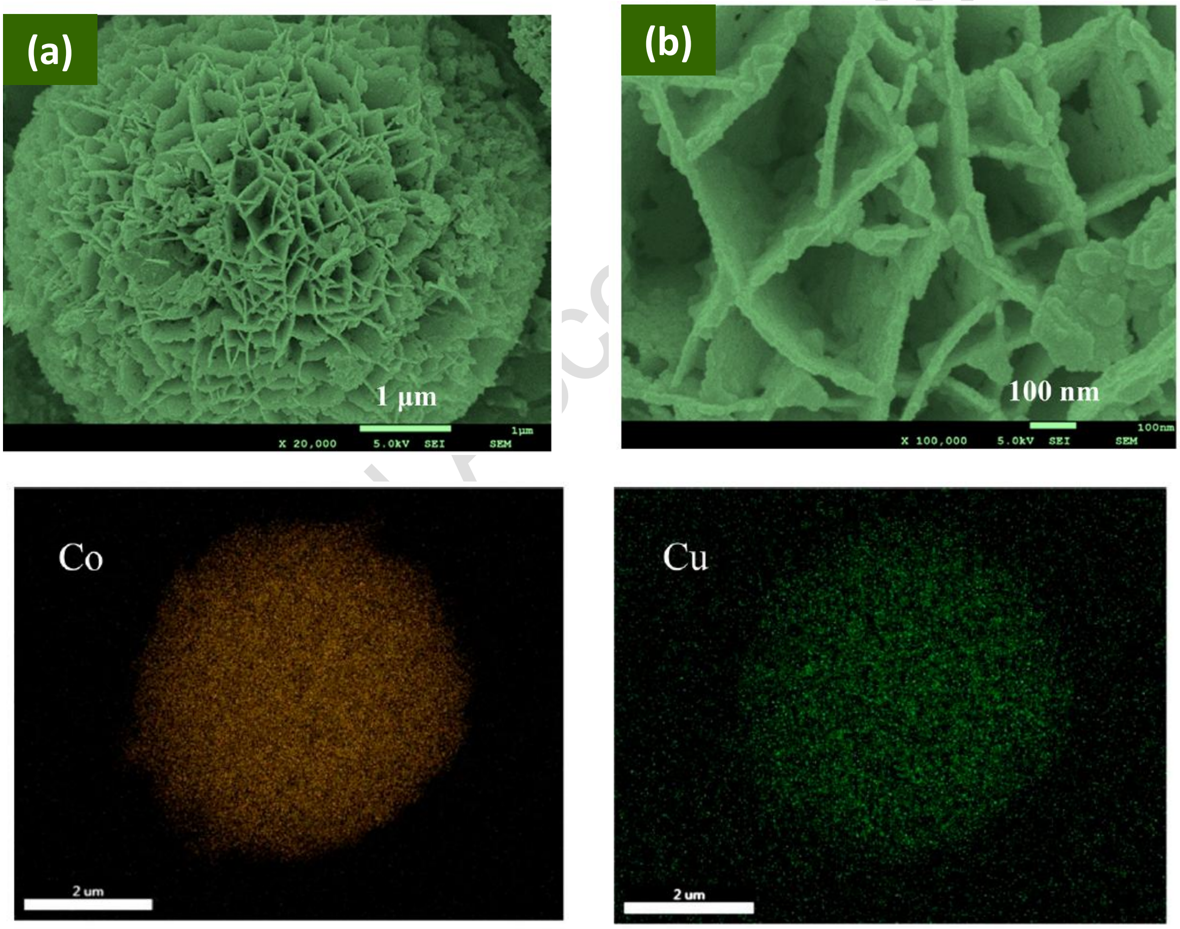

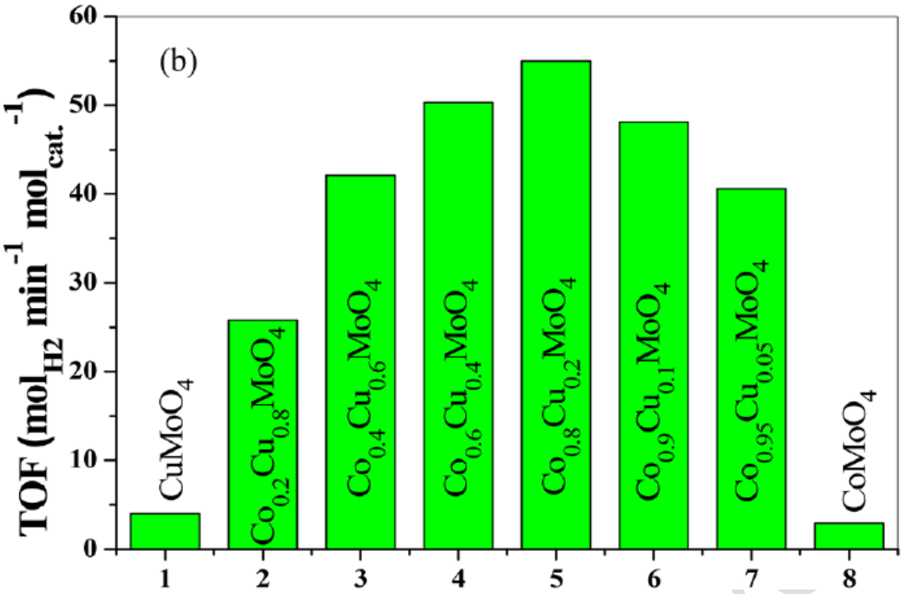

Figure 36. Top: (a) and (b) SEM images of $Co_{0.8}Cu_{0.2}MoO_4$ sample, Middle: elemental mappings of a $Co_{0.8}Cu_{0.2}MoO_4$ microsphere and Bottom: comparison of TOF values for different catalysts. Reprinted with permission from ref 181. Copyright 2018 American Chemical Society.

These nanoplatelets of approximately 20 nm are closely cross-linked to each other. XPS results indicated the coexistence of oxidized Co^{2+}, Cu^{2+}, and Mo^{6+} on the surface of $Co_{80}Cu_{20}MoO_4$ microspheres, before AB dehydrogenation reductive reaction. Post-catalysis analyses suggested that reduced $Co^0_{73}Cu^0_{27}$ alloy at the surface of the $Co_{80}Cu_{20}MoO_4$ microspheres (CoCu@$CoCuMoO_4$ composite) would be the “real” catalyst, which achieved a highest TOF = 55.0 min^{-1} for AB hydrolysis at 25 °C (Figure 36, down). The six recycling runs almost conserved this activity.

Other oxidized composites have been reported and used as nanocatalysts for AB hydrolytic dehydrogenation at 25 °C, notably defect-rich Co–CoOx@graphene (Co material was not completely oxidized),[182] and Co–Co_3O_4@carbon dots,[186] which achieved consistent TOF about 15 to 18 min^{-1} for this reaction. Other high dimension yolk-shell structured materials Co_3O_4@Co_3O_4 (and copper-doped derivatives $Co_xCu_{1-x}Co_2O_4$@$Co_yCu_{1-y}Co_2O_4$) were formed as microspheres with typical diameters between 2 to 4 μm by hydrothermal reaction followed by high temperature calcination process.[187] The shells were formed of layers of thickness approximately 200 nm where smaller microspheres are inside the larger microspheres. These structured materials of higher dimension than nanocatalysts, used as cobalt oxide composite heterogeneous catalysts achieved for AB hydrolysis at 25 °C TOFs around 19 min^{-1}, and 82 min^{-1} from Cu doping (XPS surface estimation gave a 85:15 Co:Cu molar ratio –enriched in copper– *vs* a 92:8 ratio deeper inside the shells). These authors also described hybrid $Co_3O_4/CuMoO_4$ heterogeneous catalysts formed as micrometer-sized flowers composed of nanorods of diameter of 50−100 nm.[188] These catalysts achieved for AB hydrolysis a TOF of 129 min^{-1} at room temperature. The recyclability of these system was tested over five runs with a notable progressive deactivation (25% of original activity at the 5th run).

Metal phosphide nanoparticles that show low charge transfer from the metal to P have been originally used in water splitting, as electrocatalysts or as co-catalysts in photocatalytic processes. In an extension of this reactivity, CoP were used to promote hydrolytic H_2 evolution from AB hydrolysis in the presence of a base.[183] The CoP nanoparticles were synthesized from a Co-based colloidal precursor ($CoNO_3{\cdot}6H_2O$ plus $CO(NH_2)_2$ with NH_4F and sodium citrate) treated at 300 °C by NaH_2PO_2 for reduction. EDX and elemental analysis confirmed the presence of Co and P –uniformly distributed throughout the CoP NPs of 15 nm average size– for a Co:P molar ratio 1:1. The introduction of anions (^{-}OH better than F^{-} and Cl^{-}) during AB hydrolysis was needed to reduce an induction period (of *ca* 3.5 min) observed before hydrogen evolution. This was attributed to strong interactions between water molecules and the catalyst, which impeded contact with AB reagent. Nevertheless, a TOF =

72.2 min^{-1} was achieved at a CoP catalyst:AB molar ratio of 0.04 under air. The cobalt phosphide catalyst was reused seven times, almost without loss of activity.

Another study reported CoP nanoarray *in situ* grown on titanium mesh (CoP NA/Ti, as monolithic non-dispersed catalyst with Co:P ratio 1:1) used for hydrogen production from AB hydrolysis with an initial TOF = 42.8 min^{-1} that retained more than 99% of catalytic activity after 10 cycles.[184] This study correlated the general robustness of CoP systems, including this monolith of nanosheets array grafted on macroporous Ti mesh.

A series of cobalt boride amorphous alloys Co_xB_{1-x} (x = 0.25, 0.50, 0.75) were synthesized via a single-step liquid reduction route with assistance of shape modifier (ethanediamine) and dispersant (PVP) by adjusting a molar ratio of Co^{2+}/BH_4^- ions (3:1, 1:1, 1:3, respectively) from $CoCl_2.6H_2O$ and $NaBH_4$.[185] The as-fabricated Co_xB_{1-x} amorphous alloys are ferromagnetic, and are structured as microspheres with size distribution ranging around 200–300 nm; the grain size gets smaller with increase of the cobalt content. The Co_xB_{1-x} samples catalyzed the methanolysis of AB for releasing H_2 after a long induction period (over 30 min), and $Co_{75}B_{25}$ achieved a highest TOF = 12.4 min^{-1}, which retained 71% of its initial catalytic activity after 5 cycling runs achieved from magnetic separation.

The current knowledge indicates that cobalt nanoparticles have probably among the highest intrinsic activity in pure monometallic form for a non-noble metal. This activity can be most valuably exalted by their encapsulation or supporting on photosensitive supports to produce light-enhanced processes for AB dehydrogenation. Bimetallic alloying –more than core-shell structure– seems also to be promising, especially with ruthenium and to a lesser degree copper. This, not true only from a mere activity viewpoint, but also from a fundamental approach aiming at further understanding of the so-called “synergetic” bimetallic effects, necessitates advanced knowledge of alloys preparation and structure. In addition, the magnetic properties of cobalt-based nanocatalysts in general led to easier and cleaner recycling with thus enhanced performances from this perspective. Notably, cobalt alloying with metalloid elements (P, B) recently provided several non-dispersed technological alternatives to the more classical mono- and bimetallic supported nanoparticle catalysts; such systems will certainly be further developed in the coming years.

3.7. Advances in nickel-based and alloys nanoparticle catalysts

The market price for nickel is notably stable, and was found around 14 USD kg^{-1} between 2012-2019.[189]

With such a low price, and availability as d^{10} metal, the catalysts based on nickel, and especially Ni nanoparticles, have early on attracted attention for AB hydrolysis.[30] Notably, monodisperse nickel nanoparticles (size 3.2 nm) were prepared by the reduction of $Ni^{II}(acac)_2$ with borane tributylamine, in the presence of oleylamine and oleic acid. The as-synthesized Ni nanoparticles supported on the Ketjen carbon support (S_{BET} = 800 m^2 g^{-1}), without surfactants removal, exhibited catalytic activity in H_2 production by hydrolysis of AB at 25 °C with a TOF = 8.8 min^{-1}, and retained *ca* 80% of its initial activity after the 5th cycling run for a TTO = 4200 over 23 h.[190] Following this milestone work, surfactant-free Ni NPs were prepared via a gas phase (dry) process in which volatile nickelocene [$Ni^{II}Cp_2$], Cp = cyclopentadienyl) was used as the precursor of Ni, and deposited by vapor deposition on a porous nanocarbon powder support (MSC-30, S_{BET} = 3135 m^2 g^{-1}).[41] Reduction at 300 °C under H_2 flow was then achieved to produce Ni@MSC-30, with Ni^0 nanoparticles of mean diameter of 6.3 ± 1.7 nm and catalysts S_{BET} = 934 m^2 g^{-1}. Ni@MSC-30 (Ni 18.2 wt%)

achieved another milestone benchmark activity, giving a TOF = 30.7 min^{-1} for hydrolysis of AB at 25 °C. Following this work with carbon support, nickel nanoparticles immobilized on three-dimensional nitrogen-doped graphene-based frameworks (Ni@3D-N-G, Ni 11 wt%, S_{BET} *ca* 934 m^2 g^{-1}) achieved hydrogen production from the hydrolysis of AB with a TOF = 41.7 min^{-1} at RT.[191]

The dispersion of Ni nanoparticles into zeolitic MOF ZIF-8 was achieved both via a dry vapor-phase sequential deposition–reduction method,[192] and different solution approaches.[192,193,194] The use of nikelocene, $NiCP_2$, in vapor deposition onto ZIF-8, or its dispersion in diethyl ether solution with methanol suspension of ZIF-8 and solvents volatilization, were followed by reduction with H_2 at 300 °C for several hours.[192] The Ni nanocatalysts resulting from vapor phase deposition-reduction process, presumably because of twice smaller NPs (2.7 ± 0.7 nm), achieved the best activity with a TOF = 14.2 min^{-1}. On the other hand, nanocatalysts of Ni (and also Fe, Co or Cu salts) were synthesized upon deposition-precipitation method using $NiCl_2.6H_2O$ as Ni source, ZIF-8 nanocrystals of 75 nm size as support, and mild fast reduction by $NaBH_4$ at RT. Ni@ZIF-8 (Ni NPs of 2.7 nm size) achieved the best performance in AB hydrolysis with a TOF = 85.7 min^{-1} at 25 °C.[193,194] Mechanistic studies using kinetic isotope effects suggested that the cleavage by oxidative addition of an O−H bond on Ni^0 in H_2O is the rate-determining step in the reaction. Accordingly, the AB hydrolysis is accelerated in the presence of NaOH as base and quenched in the presence of HCl. Thus, an "on−off" control of the reaction can be established by their successive addition. Reusability tests showed that the catalytic activity was maintained until the 5th run with a decrease of the rate for the last run. The comparison of these studies, which used chemically related ZIF-8 supports, and yielded NPs of approximately same size, highlighted the importance of materials synthetic method and metal reduction mode.

Beside intrinsic activity for AB hydrolytic dehydrogenation, studies seeking at structure-reactivity knowledge and recovery efficiency have also been performed. Ni^0 nanoparticles supported on polydopamine coated cobalt ferrite Ni/PDA–$CoFe_2O_4$ was prepared by two step impregnation-reduction method (NPs size 12.3 ± 0.7 nm) and used as catalysts in H_2 evolution from the hydrolysis of AB at RT. As-prepared, the catalyst was magnetically separable and reused along 10 runs without activity decrease from the initial TOF = 7.6 min^{-1}.[195] Ni NPs in the size range of 4.9−27.4 nm were synthesized by tuning the ratio of $Ni^{II}(acac)_2$ and trioctylphosphine in the presence of oleylamine, and eventually supported over various carbon supports. Their catalytic activities in the hydrolytic dehydrogenation of AB was found to be size- and support-dependent (TOF ranging *ca* 2.0-8.0 min^{-1}).[196]

Photocatalytic application of AB dehydrogenation with monometallic Ni NPs has also been studied by self-assembly of preformed Ni/oleylamine NPs,[190] and ultrathin graphitic carbon nitride (g-C_3N_4) nanosheets, as a semiconducting support.[197] An optimum AB hydrolysis rate was obtained when the size of the Ni NPs was 3.2 nm, with an initial TOF = 18.7 min^{-1} under visible light irradiation, while in the dark the rate of H_2 evolution decreased to a TOF = 9.5 min^{-1}. The Ni/g-C_3N_4 catalyst maintained 75% of its initial activity after four-cycles of the reaction with a noticeable aggregation of the NPs.

An innovative approach at the solid state was proposed in which nanosizing AB with solid nickel was achieved by encapsulating pre-synthesized nanosized AB particles within a nickel matrix.[198,199] This Ni/AB composite used for H_2 thermolytic evolution could reduce the H_2 release temperature, suppressed the melting of AB and the production of volatiles by-products, including diborane and borazine.[198] This approach in addition enabled a reversible release/uptake of pure H_2 at 200 °C and 60 bars pressure. The reversibility was hypothesized to occur through an iminoborane oligomer resulting from the initial decomposition of the nanosized Ni/AB matrix. Nanosized AB as a white powder had a particle size ranging from 20 to 160 nm (with crystalline size of 42 ± 2 nm) and the Ni nanoparticles were smaller (1-7 nm).[199] The resulting Ni/AB, a grey solid (Figure 37), was thus investigated for thermolytic dehydrogenation and partially-reversible hydrogen storage, but also as a one-shot all-solid and all-in-one material under hydrolytic conditions between 20–50 °C with TOF *ca* 14.0 min^{-1} at higher temperatures and conversion of AB about 80%.[199]

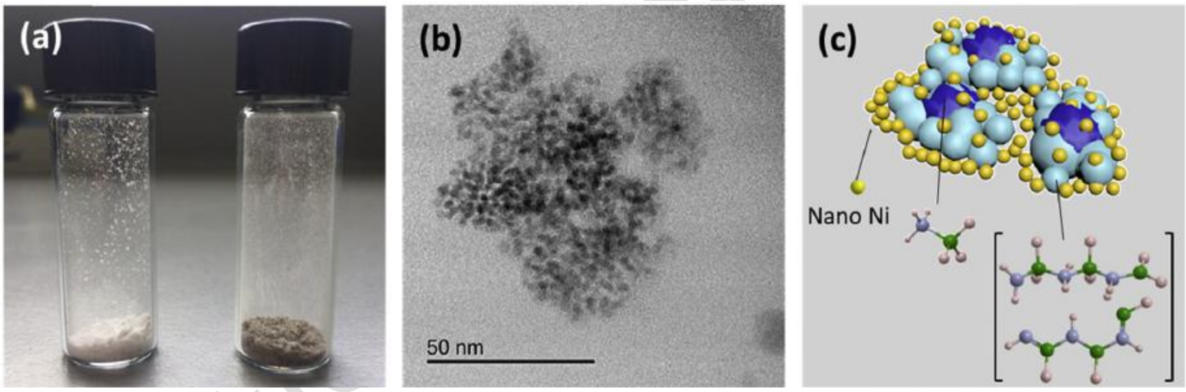

Figure 37. (a) Photograph of the AB nanoparticles (white sample, left) and of Ni/AB (grey sample, right). (b) TEM image of Ni/ AB. (c) Schematic representation of Ni/AB: crystalline AB nano-domains embedded within a matrix of oligomeric [BH_xNH_x] species and isolated metallic Ni nanoparticles. Reprinted with permission from ref 199. Copyright 2018 Hydrogen Energy Publications LLC, Elsevier Ltd.

The synthesis of bimetallic systems based on nickel, and further integrating various noble metals in minor amounts, has been successful for improving the catalytic rates of Ni-based catalysts in the H_2 production reactions from AB and derivatives.[61,62,200,201,202]

Nickel-gold alloy nanoparticles ($Ni_{93}Au_7$) were immobilized into MIL-101 by DSA combined with a liquid-phase concentration-controlled reduction.[61] Au^{3+} and Ni^{2+} precursors were introduced into the pores of the MOF by DSA,[92] and importantly, in the following reduction, a high concentration reductant solution was employed ($NaBH_4$ solution enters into the pores of the MOF by capillary force and reduces the metal specifically deposited in the very pores of MIL-101), resulting in the formation of $Ni_{93}Au_7$@MIL-101 as highly dispersed AuNi alloy ultra small NPs (1.8 ± 0.2 nm) encapsulated within the pores of MIL-101, without deposition of the NPs on the external surface. In AB hydrolysis for H_2 production, the$Ni_{93}Au_7$@MIL-101 catalyst was more active than equivalent monometallic samples (pure Ni NPs with slower but complete conversion are more active than Au NPs, which do not complete the H_2 production), with a TOF = 66.2 min^{-1}. The catalyst activity remained unchanged after five runs.

Nickel-rhodium nanoparticles supported on GO ($Ni_{88}Rh_{12}$/GO) have been synthesized through *in situ* co-reduction of $RhCl_3$, $NiCl_2$ and GO in water, using AB or MeAB under ambient conditions.[200] The formation of graphene supported Ni/Rh NPs (structurally ill-defined, sizing 1.8 ± 0.4 nm) indicated that the GO was reduced during the process. The activity in terms of TOF is *ca* 92 min^{-1}, considering both metals, for this as-synthesized NPs.

For nickel-ruthenium the DSA and site-controlled reduction strategy was also used for producing $Ni_{70}Ru_{30}$@MIL-101.[201] Morphologies of as-synthesized NiRu@MIL-101, and the recycled NiRu@MIL-101 catalyst after the 4th cycle, showed an average particle size of about 1.8 ± 0.4 nm. The BET surface area of MIL-101, NiRu@MIL-101 and recycled NiRu@MIL-101 were reported at 2276, 1285, and 945 m^2 g^{-1}, respectively. The $Ni_{70}Ru_{30}$@MIL-101 catalyst with a H_2 release at TOF = 273 min^{-1} from AB hydrolysis was found to undergo a gradual decrease in the catalytic activity along four cycles attributed to an increase of the viscosity of the solution and a high concentration of metaborate (BO_2^-), possibly clogging the pores of the MOF support.

Nickel-platinum bimetallic nanocatalysts prepared by the deposition-precipitation method have been enclosed into zeolites MOF ZIF-8 (polyhedron nanocrystals sizing *ca* 40-60 nm), with tunable composition (such as $Ni_{67}Pt_{33}$).[62] The mixture of metal cations from $NiCl_2$ and $PtCl_4$ was incorporated into ZIF-8 via aqueous suspension. Then, fast co-reduction by using $NaBH_4$ in water was conducted under N_2. The alloy nanocatalyst $Ni_{67}Pt_{33}$@ZIF-8, compared with bimetallic composites similarly synthesized $Co_{67}Pt_{33}$@ZIF-8, $Cu_{67}Pt_{33}$@ZIF-8, $Ni_{67}Rh_{33}$@ZIF-8, and $Ni_{67}Ru_{33}$@ZIF-8, exhibited the best activity in the AB hydrolytic dehydrogenation at 20 °C with a TOF = 361 min^{-1}. The S_{BET} of ZIF-8 was originally 1663.3 $m^2\ g^{-1}$ but largely decreased to 938.4 $m^2\ g^{-1}$ with the formation of amorphous 2.0 ± 0.5 nm alloy NPs packed in the ZIF-8 framework (Ni/Pt 7.3 wt%). All the alloyed nickel-platinum NPs gave much better results than the pure Pt@ZIF-8 or Ni@ZIF-8 supported materials (having TOF below 25 min^{-1} in the absence of additional base).[62] NaOH is a promoter of this bimetallic catalyst (boosting TOF up to 600 min^{-1}). The coordination of OH^- to the NPs surface increases its electron-richness and accelerates the rate-limiting surface oxidative addition of water. The $Ni_{67}Pt_{33}$@ZIF-8 nanocatalyst achieved a selective dual catalytic dehydrogenation-hydrogenation process using AB as H_2 source and 4-nitrophenol, styrene or benzonitrile as organic substrates (Figure 38).

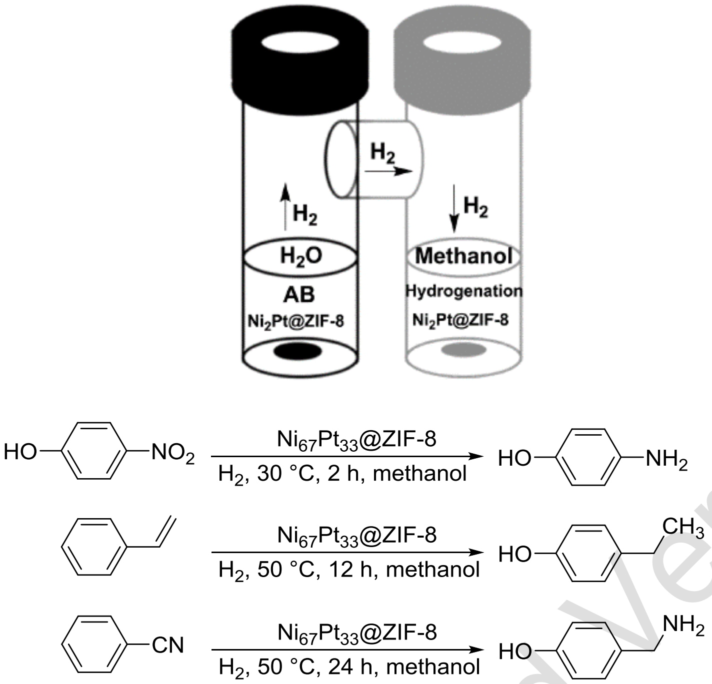

Figure 38. Tandem reaction for hydrogenation with H_2 generated from AB catalyzed by $Ni_{67}Pt_{33}$@ZIF-8. Reprinted and reproduced with permission from ref 62. Copyright 2018 American Chemical Society.

Consistent performances of bimetallic nickel-platinum were recently reported for nanoalloys with hollow structures supported on CNTs ($Ni_{67}Pt_{33}$/CNT with final particle size *ca* 4.5 nm). Such materials were synthesized using a multistep galvanic replacement method. A TOF = 302 min^{-1} was achieved for the hydrolysis of AB.[202]

Bimetallic nanocatalysts incorporating non-noble copper in addition to nickel were the subject of various studies extending from the examination of basic performances in AB hydrolysis to the use of the H_2 formed for tandem hydrogenation studies.[203,204,205,206]

Nickel-copper nanoparticles were prepared via wetness impregnation using nitrate salts $Cu(NO_3)_2$ and $Ni(NO_3)_2$ over mesoporous carbon or silica nanospheres (Figure 39, mesoporous silica MCM-48 and mesoporous carbon CMK-1 nanospheres of 1500-1600 m^2 g^{-1}). A metal loading of 5-20 wt% was achieved.[203]

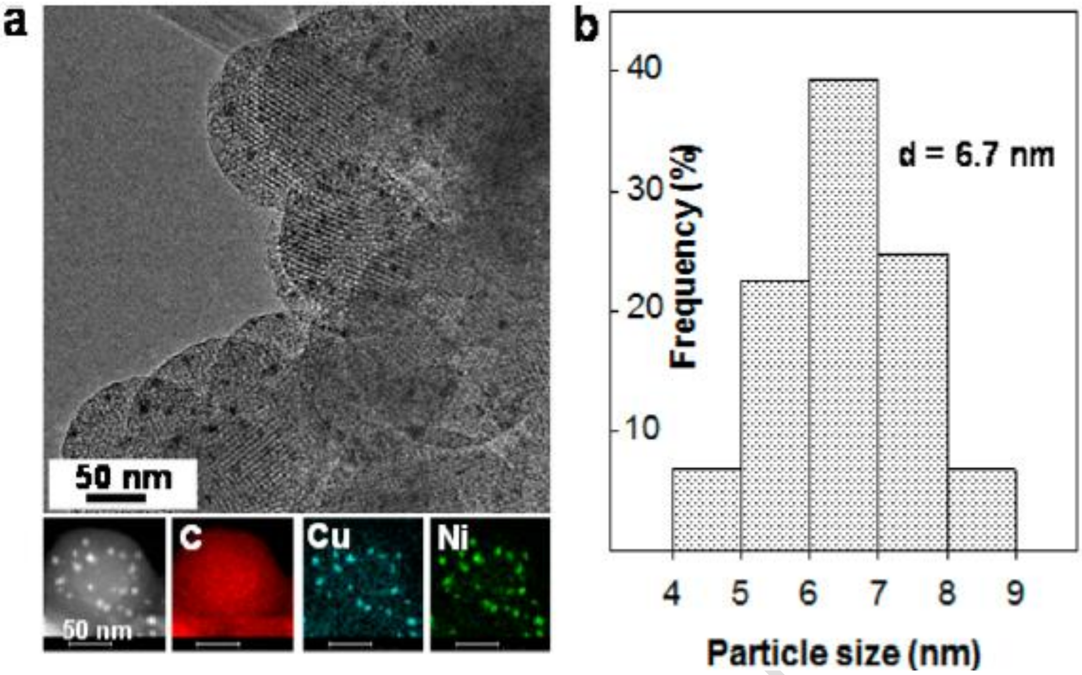

Figure 39. $Ni_{50}Cu_{50}$/CMK-1 (metal 4.7 wt%): a) HRTEM and STEM-HAADF imaging, EDS element mapping; b) metal particle size distribution histogram. Reprinted with permission from ref 203. Copyright 2015 American Chemical Society.

The impregnated samples were calcinated at 400 °C for several hours. The d-band center position for the NiCu alloy had binding strength to adsorbate located between Cu (−2.67 eV) and Ni (−1.29 eV). The resulting $Ni_{50}Cu_{50}$/CMK-1 (particle size 6.7 nm, 5 wt% Ni, Figure 39) exhibited superior activity for dehydrogenation of AB under ambient conditions with a TOF = 54.8 min^{-1}, and retained about 50% of this initial activity after six runs.

A milder synthetic approach for nickel-copper nanocatalysts synthesis employed the preformation of $Ni_{75}Cu_{25}$ nanoparticles from Ni and Cu acetylacetonate in the presence of oleylamine and trioctylphosphine (Figure 40), followed by NPs supporting on SiO_2 beads.[206]

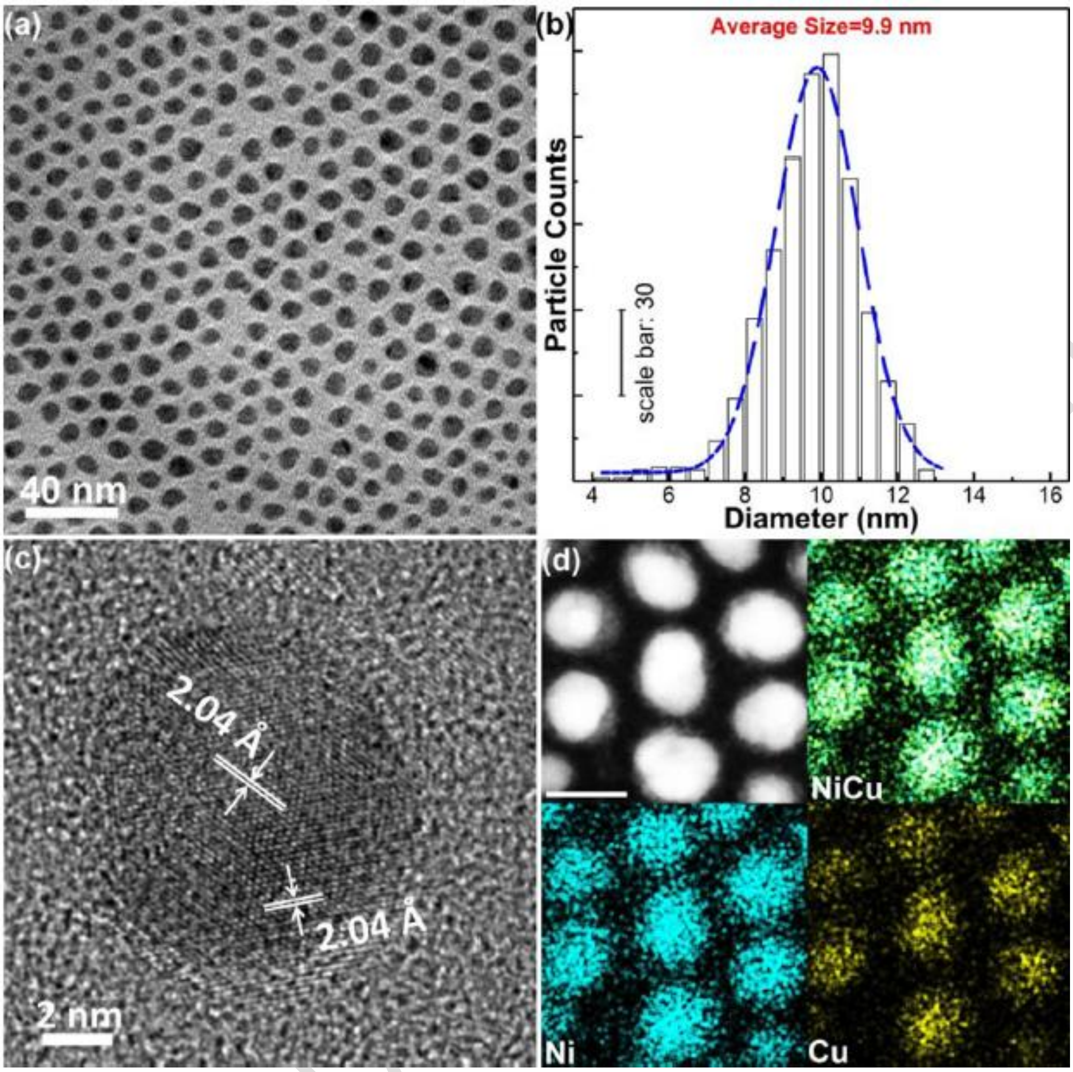

Figure 40. $Ni_{75}Cu_{25}$ NPs: (a) TEM imaging, (b) particle size distribution, (c) HRTEM imaging (d) HAADF-STEM and STEM-EDX elemental mapping (d). Reprinted with permission from ref 206. Copyright 2019 American Chemical Society.

Differently sized nonporous silica spheres (*ca.* 50 to 500 nm) were used as supports. The activity of $Ni_{75}Cu_{25}/SiO_2$ in the hydrolysis of AB catalysts increased with SiO_2 beads size decreasing. Such result was attributed to a lesser aggregation of bimetallic NPs (*ca.* 9.9 ± 2.2 nm) by using SiO_2 spheres with higher curvature and longer individual separation. $Ni_{75}Cu_{25}$ NPs supported on the smallest 50 nm SiO_2 beads exhibited a maximum TOF = 25.3 min^{-1}, which was higher than other unsupported and supported analogues formed. Notably, S_{BET} of these nanocatalysts varied in the range of 11 to 195 $m^2\ g^{-1}$, this latter value corresponding to the most active sample. Interestingly, the catalysts reusability was reported over eleven runs. That showed that the initial activity rate is retained up to 4 runs, and then slowly degrade along 6 further runs (*ca*. 40% at the 10th) but could be partially restored (*ca*. 80%) from "fresh" recycling at the 11th run with catalysts separation and cleaning instead of further AB addition.[206]

Ni(II) and Cu(II) from nitrate salts were incorporated into a mesoporous MOF MIL-101 ($Cr_3F(H_2O)_2O(BDC)_3.nH_2O$, BDC = benzene-1,4-dicarboxylate, n ≈ 25, with pore diameters of 2.9 and 3.4 nm) by DSA,[92] followed by *in situ* reduction using AB to produce the NiCu@MIL-101 nanocatalyst (average NPs size *ca* 3 nm of ill-defined structure).[204] The $Ni_{72}Cu_{28}$@MIL-101 (Cu 1.09 wt% and Ni 2.65 wt%) achieved cascade reactions of AB dehydrogenation followed by nitroarene hydrogenation (Figure 41), with for nitrobenzene a benchmark TOF = 1.65 min^{-1} (based on Ni). The use of methanol/water solvent mixture was necessary for the tandem reaction. For comparison, hydrogen sourcing by AB hydrolysis for the nitroarene hydrogenation was changed for an external H_2 hydrogen supply flow, whereas other reaction parameters remained unaltered. The reaction yield was as low as 2% after 19 h, suggesting that limited H_2 gas dissolved in the solution that hampered contacts with substrates.

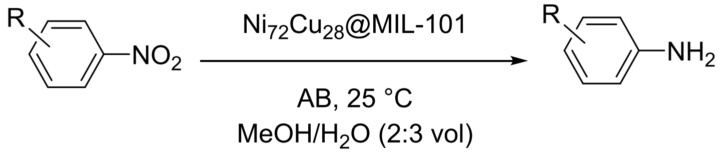

entry	substrate	product	yield (%)	time (min)
1	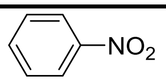	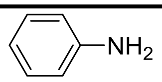	>99	4

2	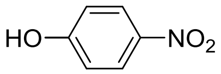	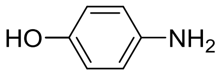	>99	4
3	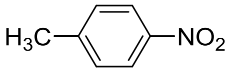	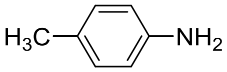	>99	4
4	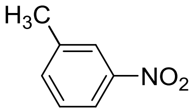	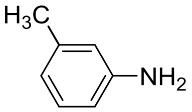	>99	4
5	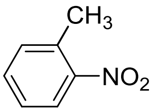	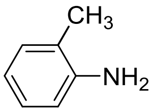	>99	4
6	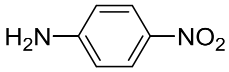	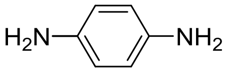	>99	4

Figure 41. Ni$_{72}$Cu$_{28}$@MIL-101 used for cascade reactions of AB dehydrogenation and nitroarene hydrogenation. Reproduced with permission from ref 204. Copyright 2017 Royal Society of Chemistry.

Consistent catalytic results were reported, describing a tandem H_2 production from AB methanolysis and nitro- or cyanoarenes hydrogenation. A better defined bimetallic nickel-copper nanoalloy (Ni$_{64}$Cu$_{36}$) was used and further immobilized on graphene.[205] Quasi-monodisperse CuNi NPs of 16.0 ± 1.0 nm (Figure 42, top) were prepared by the co-reduction of Ni^{II}(acac)$_2$ and Cu^{II}(acac)$_2$ with borane-*t*-butylamine as reducing agent in oleylamine as solvent and surfactant, and oleic acid (co-surfactant for further NPs stabilization). The alloy structure was ascertained by STEM-EELS elemental mapping showing Ni (green) and Cu (red) distribution within the NPs, further supported by the location of d-band center. Ni$_{64}$Cu$_{36}$@G nanocatalyst achieved the challenging AB methanolysis with a TOF = 49.1 min^{-1} and subsequent hydrogenation reactions in pure methanol with conversion yield above 97% (Figure 42, bottom).[205]

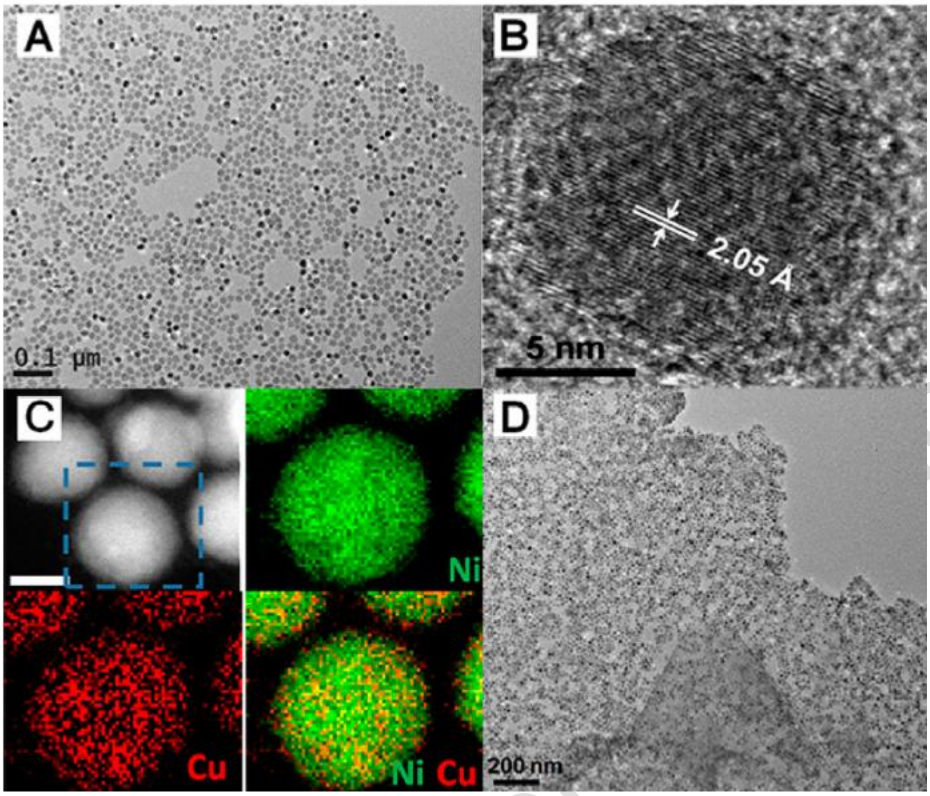

$$Ar{-}NO_2 \text{ (or Ar-CN)} \xrightarrow[\text{AB (3 mmol) methanol, 25 °C}]{Ni_{64}Cu_{36}@G} Ar{-}NH_2 \text{ (or Ar-}CH_2NH_2\text{)}$$

entry	substrate	product	yield (%)	time (min)
1	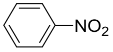	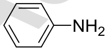	>97	30
2	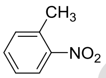	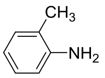	>97	30
3	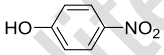	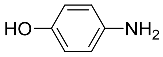	>97	30
4	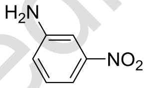	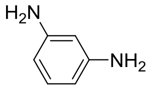	>97	90
5	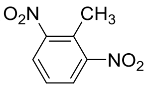	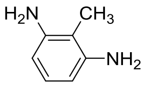	>97	120
6	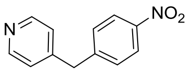	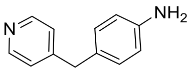	>97	30
7	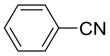	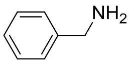	>97	30

Figure 42. Top: (A) $Ni_{64}Cu_{36}$@G TEM imaging; (B) HRTEM imaging; (C) HAADF-STEM (scale bar: 10 nm) and STEM-EELS elemental mapping with Ni (green) and Cu (red) distribution; (D) TEM image of CuNi NPs

activated by immersing in *t*-butylamine. Bottom: catalyzed tandem reduction of nitro and nitrile compounds. Reprinted and reproduced with permission from ref 205. Copyright 2017 American Chemical Society.

From selectivity perspective, when CN and NO_2 functions coexisted, NO_2 was selectively reduced to NH_2 while CN remained untouched. TOF in AB methanolysis of pure Ni@G or Cu@G analogues were determined to be 16.0 min^{-1} and 1.4 min^{-1}, respectively. Reusability of the catalyst showed no activity change in the first four runs. After the 10th cycle, the catalyst retained the alloy structure but the catalytic efficiency ceiled to 80% conversion yield. This degradation was attributed to NH_3 surface poisoning of the NPs, while their stability could be further improved by immersion of CuNi NPs in *t*-butylamine.

The activity of bimetallic and trimetallic (derived from Ni–Cu) Ni-based catalysts incorporating rarely employed Cr, Mo, W group 6 metals have also been explored recently, as well as other trimetallic catalysts derived from Ni–Pt association.[207,208,209] With the view of preventing agglomeration in small Ni nanoparticles, introduction of an atomic diffusion barrier –using refractory Cr, Mo, and W transition metals between the Ni atoms present in majority– was achieved by the preparation of unsupported bimetallic nanoparticles $Ni_{100-x}M_x$ (M = Mo, W, Cr).[207] These were synthesized via a surfactant-assisted co-reduction method using $NiCl_2.6H_2O$, $NaMoO_4.2H_2O$ (or $Na_2WO_4.2H_2O$, or $Cr(NO_3)_3.9H_2O$) in water with PVP and additional $NaBH_4$ reductant. TEM analysis for $Ni_{90}Mo_{10}$@PVP, $Ni_{80}W_{20}$@PVP, and $Ni_{90}Cr_{10}$@PVP confirmed that bimetallic NPs have a smaller size (3.8, 3.6 and 2.6 nm, respectively) than pure Ni analogs (5.1 nm). XPS suggested an alloy formation in surface with consistent Ni and group 6 metal band shifts. $Ni_{90}Mo_{10}$@PVP, $Ni_{80}W_{20}$@PVP, and $Ni_{90}Cr_{10}$@PVP achieved the catalytic hydrolysis of AB at RT with TOF = 27.3, 25.0, and 10.7 min^{-1}, respectively. These Ni/M-group 6 bimetallic catalysts only achieved a partial hydrolysis of hydrazine borane (HB, $H_4N_2 \rightarrow BH_3$), with TOF in the range 16.0–40.0 min^{-1} at

25 °C by hydrolyzing only BH_3 while the N_2H_4 group did not participate. Further works addressed a successful complete hydrolysis of HB by a trimetallic $Ni_{30}Cu_{20}Mo_{50}$ nanocatalysts, formed in the absence of PVP, which resulted in bigger NPs (5.9 ± 1.2 nm) with a TOF = 1.8 min^{-1} at 25 °C.[208]

Trimetallic Ni/Pt/Co nanocatalysts supported on shape-controlled dodecaborate-based supramolecular organic frameworks (BOFs) were prepared.[209] The varied morphologies of the supports included flowerlike structures, nanorods, nanocubes, and nanosheets incorporating alloyed small nanoparticles (Figure 43).

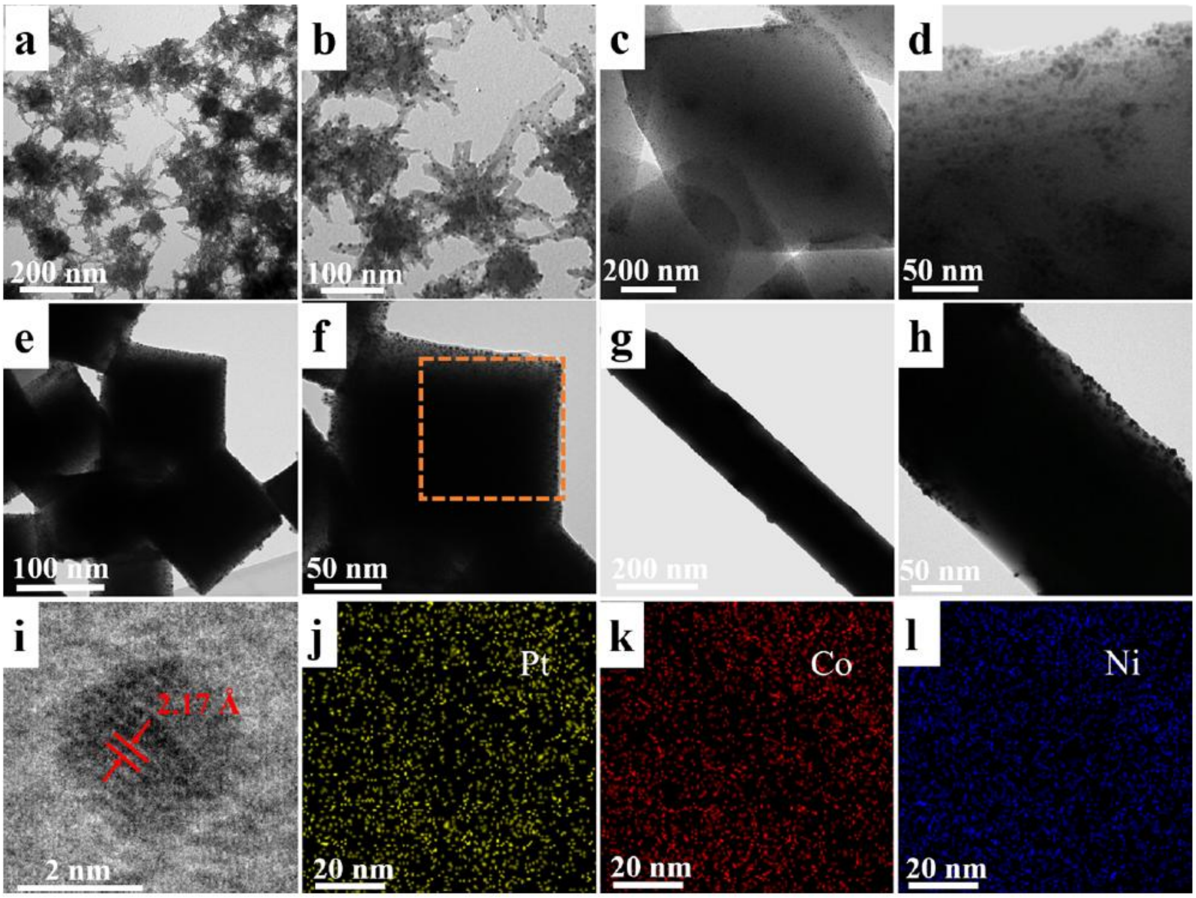

Figure 43. TEM images of $Ni_{40}Pt_{20}Co_{40}$ NPs supported on shape-controlled CB5−BOFs: $Ni_{40}Pt_{20}Co_{40}$@nanoflower BOFs (a,b) *ca* 5 nm, $Ni_{40}Pt_{20}Co_{40}$@nanosheet BOFs (c,d) *ca* 3.2 nm, $Ni_{40}Pt_{20}Co_{40}$@nanocube BOFs (e,f) *ca* 2.3 nm, and $Ni_{40}Pt_{20}Co_{40}$@ nanorod BOFs (g,h) *ca* 5.5 nm. HRTEM image of a single PtCoNi particle supported on nanocube BOFs (i). The elemental mapping of $Pt_1Co_2Ni_2$−BOFs

(j−l); the selected area is framed in (f). Reprinted with permission from ref 209. Copyright 2019 American Chemical Society.

On the preformed BOFs, precursors H_2PtCl_6, $NiSO_4$, and $CoCl_2$ aqueous solutions were injected under N_2, before further reduction step with $NaBH_4$. The cubic BOFs decorated with $Ni_{40}Pt_{20}Co_{40}$ alloys ($Ni_{40}Pt_{20}Co_{40}$@cubic-BOFs, NPs size of 2.3 nm) achieved the best catalytic performance in AB hydrolysis at 25 °C, with a TOF = 298 min^{-1}. Monometallic Co@cubic-BOFs, Ni@cubic-BOFs and Pt@cubic-BOFs catalysts showed comparatively poor performances, with TOF = 12.5, 14.1, 80.7 min^{-1}, respectively. Compared to $Ni_{40}Pt_{20}Co_{40}$@cubic-BOFs, a gradual decrease in catalytic effect appeared with the use of 3.2 nm $Ni_{40}Pt_{20}Co_{40}$@sheet-BOFs (TOF *ca* 99 min^{-1}), 5 nm $Ni_{40}Pt_{20}Co_{40}$@flowery-BOFs (TOF *ca* 50 min^{-1}), and 5.5 nm $Ni_{40}Pt_{20}Co_{40}$@rod-shape BOFs (TOF *ca* 37 min^{-1}). The difference in catalytic performances was ascribed to the size of $Ni_{40}Pt_{20}Co_{40}$ alloys in these BOFs, where the smaller NPs had an improved catalytic rate. $Ni_{40}Pt_{20}Co_{40}$@cubic-BOFs retained its initial activity in the five recycling runs.

Like it was the case for cobalt nanocatalysts, recent studies also addressed the synthesis of nickel phosphide derivatives and their catalytic behavior towards H_2 production from AB.[210,211,212] Phosphide were known as catalysts for electrocatalytic and photocatalytic hydrogen evolution in acid solutions.[213] Thus the activity of metal phosphides, FeP, Cu_3P, and Ni_2P, in the catalytic hydrolysis of AB were tested. Nanostructured Ni_2P achieved the best rate in the hydrolysis of AB with a TOF = 40.4 min^{-1} under air atmosphere at RT.[210] Unsupported Ni_2P NPs were prepared by reacting $Ni(OH)_2$ powder with solid NaH_2PO_2 under argon at 270 °C. TEM imaging showed Ni_2P particles as faceted single crystals (with lattice fringes showing a spacing of 0.221 nm corresponding to the (111) plane of Ni_2P) of average size less than 12 nm, but embedded in 50-200 nm aggregates. Along seven recycling runs with Ni_2P, the hydrogen-generating rate decreased gradually presumably because of further catalyst agglomeration. DFT calculations suggested that the Ni_2P (001) surface interacting with AB and H_2O substrates either via Ni or P. Globally, the reaction barrier reduced from about 6.6-9.5 eV without the Ni_2P catalyst, down to 0.1 eV.

Follow-up studies showed that the incorporation of Co into Ni_2P changes the electronic structures of the resulting $Ni_{2-x}Co_xP$ catalysts. Enhanced interaction with AB and facilitation of the hydroxyl activation of AB result in a decrease of the reaction barrier and an improvement of the catalytic rate.[211] The Co-doped Ni_2P nanocatalyst, $Ni_{23}Co_{43}P_{33}$ (formed of dispersed spherical NPs sizing 5-7 nm.) displayed a TOF = 41.5 min^{-1} for AB hydrolytic dehydrogenation at RT. Further improvement to TOF = 109 min^{-1} was achieved by using 5 nm sized ternary $Ni_{23}Co_{43}P_{33}$ NPs dispersed onto the surface of a GO. The improved catalytic activity stemmed from a fine tuning of the electronic structure at the NiP/Co surface that was optimized with this ternary content. This composite nanocatalyst $Ni_{23}Co_{43}P_{33}$/GO maintained 93.0% of its initial activity after 5 cycles. An approaching activity for AB hydrolysis at 25 °C, with a TOF = 95.2 min^{-1} in NaOH (0.4 M) was obtained by using a ternary NiCoP catalysts enriched in nickel and supported on oxygen-doped porous carbon OPC-300, $Ni_{66}Co_{19}P_{15}$/OPC-300, which retained after five cycles 85.0% of its initial catalytic activity.[212]

Ni doped with metal oxide was also proposed and the important role of the support as catalyst promotor was also emphasized from these three-component nanocomposites.[214] Ni nanocatalysts doped with CeO_x and supported on graphene (Ni-CeO_x/G) were synthesized via a chemical reduction route and applied for the hydrolysis of AB in aqueous solution at 25 °C. The Ni-CeO_x/G nanocomposites achieved a TOF = 68.2 min^{-1} which was found to be 50, 8, and 4 times higher than that of analogous Ni NPs (1.4 min^{-1}), Ni-CeO$_x$ NPs (8.4 min^{-1}), and Ni/G (18.0 min^{-1}), respectively, under the same conditions (Figure 44).

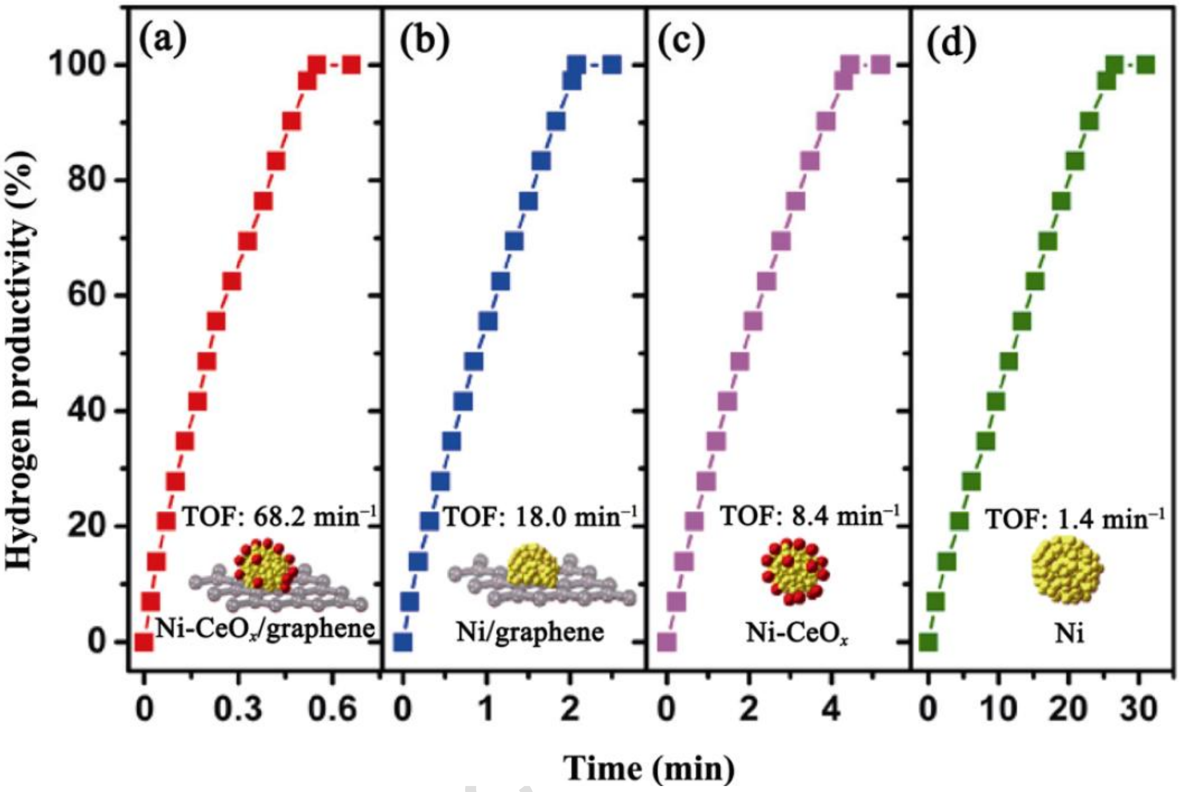

Figure 44. H_2 production from an aqueous AB solution (200 mM, 5 mL) catalyzed by (a) Ni-CeO$_x$/graphene, (b) Ni/graphene, (c) Ni-CeO$_x$, and (d) Ni at 298 K (n_{Ni}/n_{AB} = 0.08). Reprinted with permission from ref 214. Copyright 2018, Tsinghua University Press and Springer-Verlag GmbH Germany.

Nickel, being about half-less expensive than cobalt, seems to be “in the average” intrinsically only slightly less-reactive for the hydrolysis of AB, making it an interesting option for further development if its recognized toxicity is managed.[215,216,217,218] The long-known capacity of nickel for alloying also makes it a valuable candidate for “diluting” more active –but more expensive– noble metals such as Pt or Rh. Another promising opportunity when using nickel-based catalysts for hydrogen evolution from AB derivatives is clearly the tandem exploitation of their notable versatility in catalytic hydrogenation.

3.8. Advances in copper-based and alloys nanoparticle catalysts.

Exchange of stocks of high-grade refined copper is achieved at less than 1 USD kg^{-1} (*ca.* for 2019, 590 cents).[219]

However, the intrinsic activity of pure monometallic copper (or bimetallic with high copper content ≥ 90%) was found to be low, with TOF reported generally below 8 min^{-1} for AB hydrolytic dehydrogenation at RT.[30,220,221,222,223] Only copper NPs supported on silica coated Co(II) ferrite $SiO_2/CoFe_2O_4$ (CuNPs@SCF) acted as more active catalyst in the hydrolysis of AB, achieving an initial TOF = 40 min^{-1} at 25 °C.[43] Their characterization indicated the presence of ultra-small Cu^0 nanoparticles of average size 0.7 ± 0.3 nm supported on magnetically active $SiO_2/CoFe_2O_4$. Because of this unusual degree of activity for a monometallic copper catalyst, the question of alloying formation with Co is still posed, while the $SiO_2/CoFe_2O_4$ host material was reported as catalytically inactive.

Accordingly, copper-based bimetallic nanocatalysts have attracted a wide attention, first as core-shell materials with a Cu core (and surface made of either Fe, Ni, Co or Ni-Co alloys – achieving TOF *ca* 15 min^{-1} when measured–),[224,225,226] then under alloying form.[227,228,229,230,231,232,233,234] Core-shell were generally produced by an easier reduction of copper regarding the second metal, while alloy formed from co-reduction and similarity in redox potentials of the two metal precursors.

Copper bimetallic alloying was early on achieved with Ru. $Cu_{88}Ru_{22}$ nanoparticles supported on graphene were *in situ* synthesized by a one-step co-reduction of aqueous solution of Cu(II) chloride, Ru(III) chloride, and GO with AB under ambient condition.[227] The $Cu_{88}Ru_{22}$/G catalyst, formed of ill-defined nanoparticles, achieved for hydrolytic dehydrogenation of AB at RT a TOF *ca* 30 min^{-1} per total metal molar content (TOF = 135 min^{-1} normalized to Ru only). The catalyst retained 35% of its initial catalytic activities in the hydrolysis of AB in the 5th cycling run. Cu-Ru nanoparticle-embedded porous carbon composites $Cu_{92}Ru_8$@PC (Cu 67.8 wt%, Ru 9.4 wt%) were also synthesized by one-pot solvothermal reaction of $Cu(NO_3)_2$ and $RuCl_3$ with 1,3,5-benzenetricarboxylate in an ethanol and DMF solution at 85 °C for encapsulation into porous octahedral-shaped HKUST-1 (copper–1,3,5-benzenetricarboxylate MOF), further pyrolysed 3 h at 800 °C under Ar. The nanocatalyst, formed of NPs with sizes around 3-4 nm (113 m^2 g^{-1}), was used for AB hydrolysis at RT, and achieved a TOF *ca* 12 min^{-1} per total metal molar content (TOF = 97.0 min^{-1} normalized to Ru only).[228] These results suggested that copper is pertinent as metal for diluting active noble metal Ru catalyst, but seems to have an overall more a "poisonous" effect (as opposed to "synergetic") on their intrinsic activity.

The copper alloying with cobalt,[229] and cobalt oxide,[230] was found to be more promising. CuCo NPs with size below 2.4 nm have been immobilized on diamine-functionalized reduced GO, and displayed for the dehydrogenation of AB a TOF of about 51.5 min^{-1} at 30 °C.[229] While this system had a high content of cobalt (80 mol%), the related cobalt oxide with higher content of copper (80 mol%) $Cu_{0.8}Co_{0.2}O$/GO showed a catalytic activity with a TOF = 70.0 min^{-1} in the hydrolysis of AB at 25 °C.[230] A mild synthesis used chosen stoichiometry of $Cu(OAc)_2\cdot H_2O$ and $Co(OAc)_2\cdot 4H_2O$, which were mixed with GO in isopropanol solution and refluxed at 80 °C for 1 h, hydrolyzed for 30 min, and dried at 70 °C in air for 12 h. The resulting NPs sized 3.2 ± 0.5 nm (9 wt% metal) and dark-field TEM images and elemental mapping confirmed the alloy formation. The oxidized state of Cu (as CuO) and Co (as CoO) were confirmed by XPS. XRD pattern suggested an amorphous structure for the NPs. All CuO_xCoO_{1-x}/GO samples showed a TOF value higher than 45.0 min^{-1} contrasting with the value of 9.2 min^{-1} for CuO/GO (whereas CoO/GO was inactive). Interestingly, the TOF value increased with increasing Cu content in the bimetallic CuO_xCoO_{1-x}/GO samples.[230] The nanocatalyst $CuO_{80}CoO_{20}$/GO retained 94% activity after 5 cycling runs. The catalytic performance was attributed to the interfacial interaction between Cu_xCoO_{1-x} NPs and GO. Accordingly, synchrotron radiation- based X- ray absorption spectroscopy (XAS) investigation evidenced significant water adsorption on the catalyst, and strong interaction between AB and the catalyst during hydrolysis. The reduction of metal in these catalysts under AB hydrogen evolution remained an open question. In a follow-up study, the authors considered a more accurate design of their bimetallic catalysts considering the particle size and facet effects, and they synthesized a cube-like nanostructure on reduced graphene $Cu_{50}CoO_{50}$@rGO.[235] Freeze-drying process at −80 °C for six days leads to the formation of 31 nm cube-like nanostructures on rGO. The catalysts achieved a TOF = 81.7 min^{-1}, and maintained about 88% of its initial activity after 5 runs. According to a ten cycle deactivation studies the loss of cube-like structure and the reduction of Cu and Co was detrimental to the AB hydrolysis. X-ray absorption spectroscopy mechanistic studies, suggested that Cu sites in the catalyst may activate H_2O when neighboring Co oxide may anchor the AB molecules for a cooperative action.

The most recent studies addressed nanocatalysts alloying copper with platinum or palladium.[231,232,233] The synthesis of CuPt alloy NPs and their assembly on carbon-based support materials was achieved by mixing of $Pt(acac)_2$ and $Cu(acac)_2$ in co-reduction with *tert*-butylamine borane in a 1-octadecene (3 mL) solution in oleylamine (7 mL), where borane complex was used as a mild reducing agent and the amine as surfactant.[231] Preformed Cu_xPt_{1-x}

NPs were deposited on Ketjen Black (KB, S_{BET} = 800 m^2 g^{-1} by liquid-phase self-assembly, Figure 45). TEM imaging of $Cu_{68}Pt_{32}$/KB showed a deposition step without agglomeration of the monodisperse NPs of 2.2 nm average size (Pt 7.9 wt%). This synthetic method allowed tuning Cu_xPt_{1-x} content; however, tuning the ratio of atomic copper to a value higher than 75% resulted in the deterioration of the narrow particle-size distribution. The catalytic activity of $Cu_{68}Pt_{32}$/KB in the hydrolytic dehydrogenation of AB (and HB, incomplete at 3 equiv. H_2) at 25 °C was reported, with TOF around 270 min^{-1} per total metal molar content (for AB hydrolysis TOF = 859 min^{-1} normalized to Pt only). The activity of the catalyst drops in the 2nd run and preserved 75% of its initial activity until the 5th run. Consistent results, albeit with lower catalytic performance, were obtained from the synthesis of $Cu_{50}Pt_{50}$/Ketjen also using $Pt(acac)_2$ and $Cu(acac)_2$ mixed with oleylamine, but in the absence of borane reductant.[232] The resulting alloy nanoparticles of *ca* 4.0 nm (bigger in size) achieved the hydrolytic dehydrogenation of AB with an initial TOF = 102 min^{-1}, the metal surface being probably *in situ* reduced during AB hydrolysis. Along three successive cycle reaction, the catalyst maintained 75% of its initial activity.

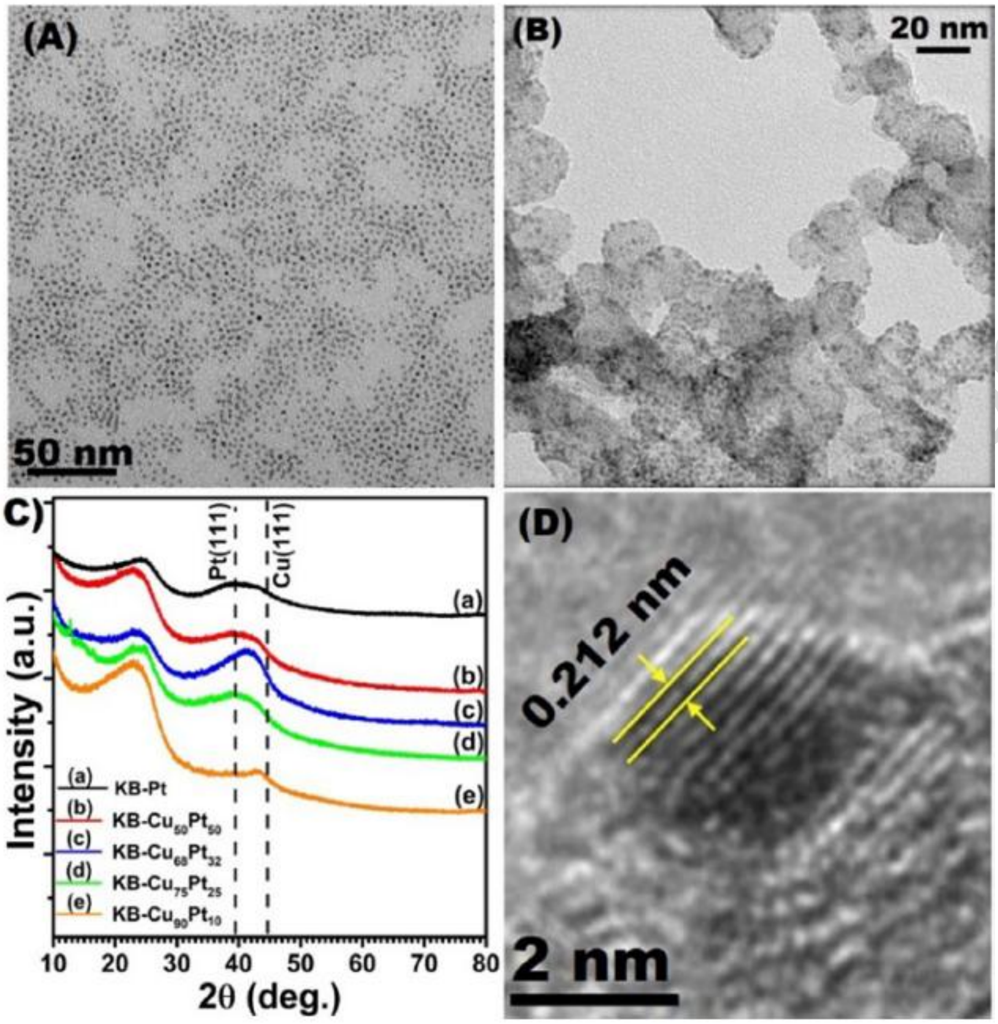

Figure 45. TEM imaging of (A) $Cu_{68}Pt_{32}$ NPs from hexane dispersion and (B) $Cu_{68}Pt_{32}$/KB NPs; (C) XRD patterns of KB-Cu_xPt_{1-x} catalysts; (D) HRTEM of a single NP $Cu_{68}Pt_{32}$/KB. Reprinted with permission from ref 231. Copyright 2017 Wiley-VCH Verlag GmbH & Co. KGaA, Weinheim.

Similarly, Cu-Pd alloy NPs were synthesized by co-reduction of $Pd(acac)_2$ and $Cu(acac)_2$ with morpholine-borane in 1-octadecene and oleylamine at 80 °C, and further supported on rGO from a dispersion in hexane/ethanol mixture.[233] Various Cu-Pd alloy NPs (2.7 nm $Cu_{30}Pd_{70}$, 2.9 nm $Cu_{48}Pd_{52}$, and 3.0 nm $Cu_{75}Pd_{25}$) were prepared, and the $Cu_{75}Pd_{25}$/rGO catalysts after annealing at 400 °C for 1 h under Ar+H_2(5%) was used for hydrolysis of AB at room temperature with the best TOF = 29.9 min^{-1}. Analogously prepared monometallic

Cu/rGO and Pd/rGO were found to be comparatively less or similarly active, with TOF = 3.61 min^{-1} and 26.6 min^{-1}, respectively.

A recent approach envisioned to employ trace amounts of palladium for doping Cu nanoparticles incorporated into MOFs of ZIF-8, ZIF-67, ZIF-67/ZIF-8 and core-shell ZIF-67@ZIF-8 type, using a DSA method.[234] The preparation of MPd_x NPs@ZIF-67@ZIF-8 composites included M = Cu, Ni, Co, Fe and Zn, with x = 0.005, 0.0067, 0.010, 0.020 and 0.05 for Pd. The composite $\text{Cu}_{99}\text{Pd}_1$@ZIF-67@ZIF-8 (M = Cu, x = 0.010) achieved an unexpected TOF *ca* 30 min^{-1} for AB hydrolytic dehydrogenation at 25 °C. This TOF was attributed to the small size of metal nanoparticles (*ca.* 3 nm) controlled by a confinement within the porosity of core-shell ZIF-67@ZIF-8 (Figure 46) and to some supposed bimetallic "synergistic effect".

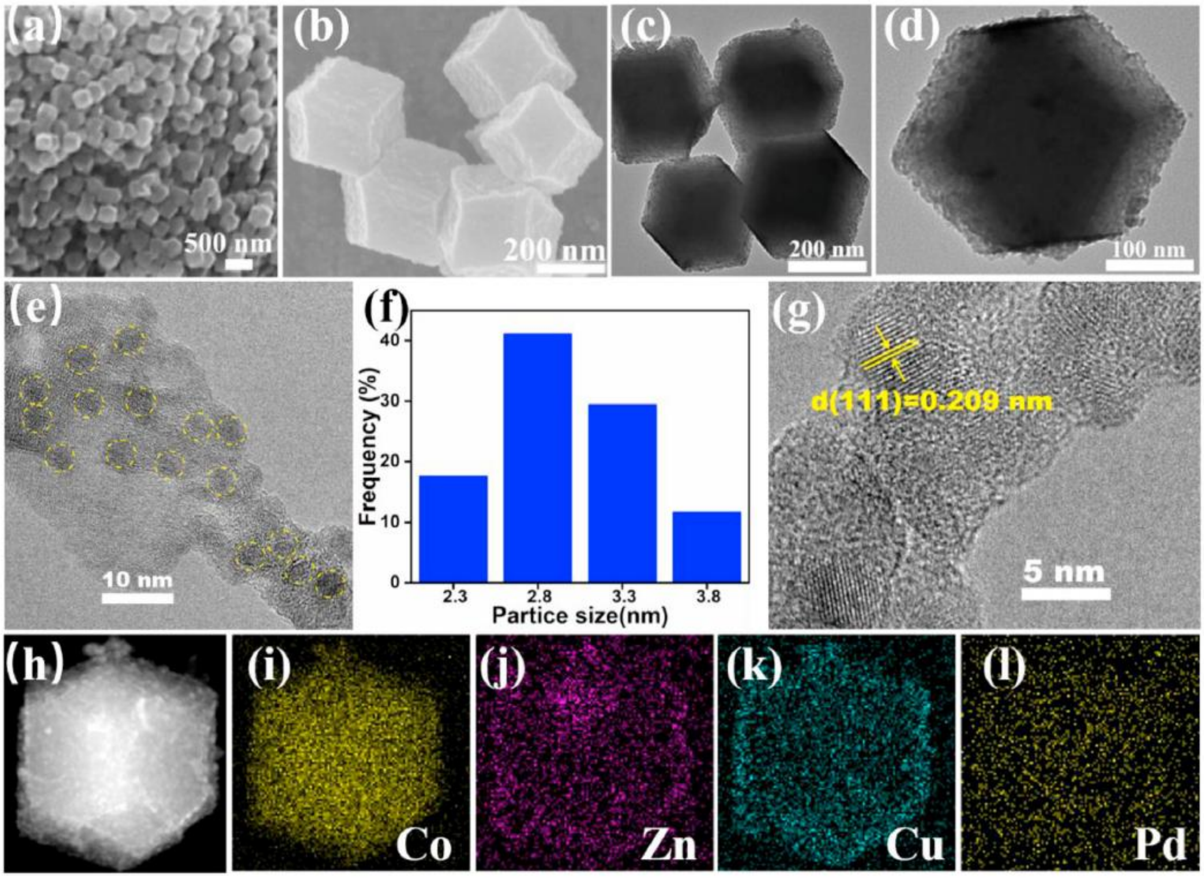

Figure 46. $CuPd_{0.01}$@ZIF-67@ZIF-8: SEM imaging (a,b), TEM imaging (c,d), HRTEM imaging (e,g), size-distribution histogram (f), and elemental mappings (h-l). Reprinted with permission from ref 234. Copyright 2020 Hydrogen Energy Publications LLC, Elsevier Ltd.

To date, the studies and results focused on copper nanoparticles used for AB hydrolytic dehydrogenation suggested that also for platinum group metals (Pt, Pd) the expensive metal can be valuably diluted within copper into bimetallic phases); like it was the case for Cu-Ru alloys. However, this alloying operates largely at the expense of the intrinsic high activity of the noble metal for the dehydrogenation of AB.

Trimetallic catalysts based on copper and preferentially cobalt, were also reported.[236,237,238] The trimetallic nanocatalysts $Cu_{52}Co_{31}Ru_{17}$@MIL-101 (Cu 1.39 wt%, Co 077 wt%, and Ru 0.75 wt%) characterized by a high $S_{BET} = 2868\ m^2\ g^{-1}$ and an average size of NPs of 6.9 ± 0.4 nm, was synthesized via a liquid impregnation method followed by reduction using $NaBH_4$ of a dispersion of $RuCl_3$, and Cu and Co nitrate salts into the porosity of hydrothermally stable MOF framework MIL-101.[236] This poorly structurally-defined catalytic material achieved H_2 evolution from AB hydrolysis at 25 °C with a TOF *ca* 40 min^{-1} (241 min^{-1} normalized to Ru only). The as-synthesized $Cu_{52}Co_{31}Ru_{17}$@MIL-101 retained about 77% of its initial catalytic activity toward hydrolysis of AB after the second run, which gradually decreased to 54% at the 5th cycling run.

The catalytic performances of Cu-based trimetallic alloys, in the absence of noble metal, have also been investigated with $Cu_{80}Co_{10}Ni_{10}$@MIL-101.[237] Chromium (III) terephthalate MIL-101 was chosen as a host matrix ($S_{BET} = 3622\ m^2\ g^{-1}$, pore volume 1.98 $cm^3\ g^{-1}$ and pore windows 1.2–1.4 nm) to encapsulate metal NPs. The nanocomposite synthesis was achieved by the solvent evaporation method. $CuCl_2.2H_2O$, $CoCl_2.6H_2O$, $NiCl_2.6H_2O$, and MIL-101 mixture in aqueous ethanol solution was heated at 60 °C before solvent evaporation, the precursors being adsorbed in the hydrophilic pores of the MOF by capillarity. The inner surface area of MIL-101 being larger than the outer surface area, the metal precursors are deposited inside the inner pores, thereby minimizing deposition on the outer surface. Reduction was performed with a pore-volume amount of high-concentration $NaBH_4$. The metal salts deposited in the MIL-101 were incorporated into the MOF pores, and NPs with an average size of 2.8 ± 0.2 nm formed inducing a significant S_{BET} decrease from = 3622 $m^2\ g^{-1}$ in the initial matrix to 2250 $m^2\ g^{-1}$ in the nanocomposite. $Cu_{80}Co_{10}Ni_{10}$@MIL-101 achieved AB hydrolytic dehydrogenation at 25 °C with a TOF = 70.1 min^{-1} and retained 73% of this TOF value after eight cycles. This drop in reaction rate was attributed to the deleterious increase in both the metaborate (BO_2^-) concentration and the viscosity of the solution. The authors proposed for explaining the “synergetic” effects observed using trimetallic NPs combined with MIL-101 that Cr^{3+} ions are Lewis acid sites in MIL-101. They would supply an acidic microenvironment, which favors AB hydrolytic dehydrogenation. The authors also proposed, based on trimetallic surface XPS and mass-analysis with D_2O in AB hydrolysis, that electron-transfer between Cu to Co and Ni leads to a decrease in its electron cloud density that may facilitate the binding of H^- hydride with Cu to form the activated complex metal–H species, which enhances AB hydrolysis catalytic rate.

Consistent results were reported with the unsupported trimetallic $Cu_{72}Co_{18}Mo_{10}$ nanocatalyst, which was formed from co-reduction with $NaBH_4$ of a $CuCl_2$, $CoCl_2$ and Na_2MoO_4 mixture in water. This material exhibited a TOF = 40.1 min^{-1} for the AB hydrolysis at 25 °C.[238] The as-prepared $Cu_{72}Co_{18}Mo_{10}$ NPs had an average particle size of *ca* 5.7 nm. Interestingly, the authors investigated in details the effect of base as co-catalyst or promotor on the hydrogen production by AB hydrolysis, as done before by Astruc group.[193] The activity of $Cu_{72}Co_{18}Mo_{10}$ for the hydrolysis of AB nanoparticles improved with an increase of the NaOH amount from 0 to 1 M, while further increasing the NaOH amount leads to a rate decrease.[238] In the presence of 1 M NaOH (or KOH) a TOF = 119 min^{-1} was measured, 3-fold higher than without NaOH. The effect of weaker base (Na_2CO_3) can slightly enhance the catalytic performance presumably because of concomitant formation of OH^-. Conversely, NH_4^+ increased concentration (possibly formed from NH_3 evolution or external addition, for instance) was found to be deleterious for the reaction. Overall, the promoting effect of the base can be assumed general instead of alkali type-dependent.[238]

The intrinsic activity of pure monometallic copper for AB hydrolysis is limited. Besides the use of copper as inexpensive metal for diluting highly active noble metals in bimetallic approaches, the studies focused on non-noble trimetallic species –based for instance on Cu-Co alloy at high atomic content (> 50%)– are clearly promising since both the use of either acidic MOF porous supports or OH^- base additive provided significant rate enhancement in AB hydrolysis. However, while this strategy would allow to avoid expensive noble metals, the somewhat sophisticated mode of synthesis of highly dispersed triple metal nanoparticles, and the cost and treatment associated to further base additive, would have to be finely handled.

3.9. Advances in iron-based and alloys nanoparticle catalysts

The iron element, Fe, is one of the most abundant on earth. Iron and steel comprise about 95 percent of all the tonnage of metal produced annually in the world. On the average, iron (and steel) are, by far, the least expensive of the world's metallic products.

Early works by Xu group first indicated that γ-Al_2O_3-supported crystalline Fe nanoparticles did not catalyze the hydrolytic dehydrogenation of aqueous AB at RT.[30] The authors further studied the catalytic activity of Fe nanoparticles formed without support nor any protective shell with the view to favor surface activity.[32] Amorphous Fe^0 nanoparticles were *in situ* generated from the reduction of iron(II) sulfate, $FeSO_4$, by using $NaBH_4$ then immediately AB. The resulting nanocatalysts achieved the complete dehydrogenation of AB with a TOF = 3.1 min^{-1}. By comparison with preformed crystalline α-Fe^0 catalysts, the amorphous character was shown to be essential to a 14- to 20-fold higher activity of the Fe^0 nanoparticles in the H_2 production from AB aqueous solution. This was tentatively attributed to a much greater structural distortion in the amorphous nanocatalyst providing a higher concentration of active sites than its crystalline counterpart. The as-prepared Fe nanocatalyst was recycled by magnetic decantation for reusing up to 20 times. Interestingly, in a study making the link between iron homogeneous and heterogeneous catalysts, Manners groups reported that iron carbonyl molecular complexes can be used as pre-catalysts for the dehydrocoupling/dehydrogenation of the DMAB upon UV photo-irradiation at ambient temperature.[47] Rare *in situ* detailed mechanistic analysis were achieved, which notably suggested that the active catalysts generated were heterogeneous in nature and consisted of small iron nanoparticles ($\leq$ 10 nm).

Following the early works on pure monometallic Fe^0 nanocatalysts, the synthesis and application of magnetically recyclable iron-containing trimetallic (triple-layered $Au_6Co_6Fe_{88,}$ and core–shell $Cu_{40}@Ni_{50}Fe_{10}$),[239,240] bimetallic ($Fe_{67}Cu_{33}$ alloy nanoparticles),[241] and even tetrametallic ($Ag_{10}@Co_{44}Ni_{39}Fe_7$/graphene core–shell)[46] catalysts for AB hydrolysis were described. In these nanocomposites, the very different nature of multimetallic species both from metal content (atomic iron between 7 and 88%) and structure (multiple layering, core-shell, alloying) makes difficult to rationally compare the performances in terms of TOF for catalytic AB hydrolysis. However, fairly consistent values of TOF = 8.37, 13.95, and 11.85 min^{-1} were reported for $Cu_{40}@Ni_{50}Fe_{10}$, $Fe_{67}Cu_{33}$ NPs, and $Ag_{10}@Co_{44}Ni_{39}Fe_{7}$/graphene, respectively.[46,242]

Most recent studies in heterogeneous catalysis for AB hydrolysis addressed the activity of NPs containing oxidized iron, such as ferrites,[243,244] and mixed-valence iron hydroxide.[245] Magnetically recyclable metal ferrite nanoparticles $MnFe_2O_4$, $CuFe_2O_4$, $NiFe_2O_4$, and $ZnFe_2O_4$ were used as catalysts for hydrogen production from the hydrolysis of AB.[243] TEM images of the ferrites revealed that all the samples are cubic nanoparticles with similar morphology in the range of 5–17 nm. The $MnFe_2O_4$ nanoparticles achieved the best AB hydrolysis rate with a H_2 evolution of 1966 ml_{H2} min^{-1} g^{-1}_{catal} (TOF *ca* 2.0 min^{-1}), *vs.* 1367 ml min^{-1} g^{-1} for $ZnFe_2O_4$, 700 ml min^{-1} g^{-1} for $CuFe_2O_4$, and 433 ml min^{-1} g^{-1} for $NiFe_2O_4$. The performance of $MnFe_2O_4$ compared favorably to the reported tests achieved with other Manganese-based catalytic materials, and five recycling of manganese ferrites were achieved by magnetic separation. Besides nanocatalysts, copper ferrite macrostructure were also prepared as cubic spinel $Cu_{0.67}Fe_{2.33}O_4$ with dominating Fe^{2+} content by high temperature combustion method from glycine-nitrate precursor.[244] The heterogeneous catalyst obtained were both used for solid-phase thermolysis of AB and its hydrolysis and were found more active than reported copper and iron oxide heterogeneous catalysts, albeit with very modest activity compared to nanocatalysts. A mixed-valent iron-layered double hydroxide (“green rust” GR as only-Fe-LDH) heterogeneous catalyst (needle- or belt-like structures with a width of up to 150 nm and a thickness of up to 20 nm), prepared by one-pot solvothermal reaction using iron(III) chloride and glycerol, was used as solar photocatalyst for H_2 evolution from AB, while other iron minerals (magnetite Fe_3O_4, hematite α-Fe_2O_3, and goethite α-FeOOH) and a benchmark TiO_2 showed little to no activity.[245] GR did not catalyze H_2 evolution at higher temperatures but achieved H_2 production at room temperature when irradiated with a solar simulator with a TOF = 0.11 min^{-1}.

The intrinsic activity of heterogeneous catalyst iron for AB hydrolysis is objectively low compared to other metals and to date, the most efficient use of iron is encountered in the generation of multimetallic nanocatalysts still of limited activity. The magnetic recyclability represents nevertheless an opportunity for recycling, which can make a marked difference for reaching an extended number of cycling runs (rarely > 10). Notably, the use of iron complexes in homogeneous hydrogenation/dehydrogenation reactions, out of the present review scope, remains of critical interest.[246,247,248]

4. MISCELLANEOUS PROGRESS RELATED TO AB DEHYDROGENATION REACTIONS

4.1 Alternative solvolysis and pyrolysis

As previously mentioned (see section 2), ammonia borane is usable for chemical H_2 storage and production both from metal-catalyzed hydrolysis in solution, and from thermolytic dehydrogenation above *ca.* 100 °C (pyrolysis), according to various inter- or intramolecular pathways.[10,268] However, some limitations of the solution hydrolytic approach should be noted, which include *i)* the state of AB and its concentration, *ii)* the optimization of the storage capacities, *iii)* the purity of evolved H_2, and *iv*) the borate waste production. For instance, concerning *effective* storage capacity, the hydrolysis of AB requires excess H_2O to form hydrated metaborates (anhydrous metaborates are not in thermodynamically stable form in the aqueous environment);[249] this reduces the effective H-content, and in a saturated AB solution at 25 °C, hydrogen content is decreased *ca.* to 5 wt%.

Another point is that in the H_2 production step, the catalyst is usually synthesized separately and then mixed with AB for achieving hydrolysis. The mode of contact is thus a decisive technological issue. Briefly, the way of putting solid hydride (amine boranes but also $NaBH_4$, *etc.*) into contact with the catalyst could be via the injection of aqueous solution of AB onto a solid-state catalyst, or alternatively the use of solid-state AB and injection of an aqueous solution of the catalyst. An all-solid approach based on the use of solid-state AB with a nanocatalyst is attractive since it may allow maximizing the effective gravimetric hydrogen storage capacity.[199] This approach has been used when nanosizing AB with solid nickel (see details in section 3.7), albeit still requiring higher thermal conditions.[198] Nanoconfinement of AB in porous nanoscaffolds was also early on found effective to promote hydrogen release, but a large amount of porous materials was required leading to a lower effective hydrogen storage.[250] Very recently, Li and Xu proposed an all-solid solution with an alternative to thermal activation by using Ti_2O_3 photothermally-induced pyrolytic dehydrogenation of AB.[249] Nanostructured Ti_2O_3 particles (corundum, rice-like NPs of 50 ± 20 nm average size) were prepared by reducing TiO_2 NPs (rutile) by reaction with CaH_2 as reducing agent at 400 °C under vacuum condition. The as-prepared Ti_2O_3 particles were employed as solar-to-heat conversion material in a solid-state system consisting of solid AB powders and Ti_2O_3 particles mixed by mechanical grinding (Ti_2O_3 ratio 10 wt% to AB). Under optimized full spectrum irradiation and at room temperature, by the photothermal effect of Ti_2O_3 nanoparticles about 2.0 equiv of H_2 was produced in 30 min, measured equal to an effective H_2 release capacity of 11.8 wt% based on reactants and photothermal materials. Without adding Ti_2O_3, almost no H_2 was produced under light irradiation at room temperature and only *ca.* 0.65 equiv of H_2 was released at 100 °C in the same time. Nanostructured Ti_2O_3, as fairly large nanoparticles, showed nevertheless a better photothermal dehydrogenation performance compared with micro-powders and sub-micro particles prepared by ball milling method. [249] The photothermal dehydrogenation of AB show low decay of reactivity after three recycling and no obvious change in morphology and crystal structure of the Ti_2O_3 activator.[249] Finally, this new technology could combine with thermal and transition metal activation, since, with the assistance of $CuCl_2$ promotor at 70 °C an ambient sunlight irradiation of 100 mW cm^{-2} (1.0 sun) was sufficient to release 2.0 equivalents of H_2 from AB thermolysis. The temperature of the reaction system was measured at 93 °C, which was mainly raised from the photothermal effect of Ti_2O_3.

Besides hydrolysis, other ways of releasing H_2 from AB in solution are the solvolysis in protic solvents such as methanol (methanolysis).[34] Like for hydrolysis, the hydridic hydrogen of BH_3 moiety in AB is expected to react with the proton given by solvent. In the most favorable case, using efficient catalysts, 3.0 equivalent H_2 gas is liberated per mole of AB. Methanolysis of AB is of interest for several reasons:[35] *i*) AB has sufficient solubility in methanol,[251] *ii*) methanolysis produces a single gaseous product (pure H_2 gas) with no ammonia contamination, *iii*) catalytic methanolysis of AB can be easily achieved at temperatures below 0 °C (CH_3OH fusion point *ca* –97 °C) that may facilitate H_2 supply in cold climate, *iv*) the $NH_4B(OCH_3)_4$ product formed from the AB methanolysis can be back converted to AB by reaction with metal hydrides at RT,[34] and *v*) AB in methanol has a high stability against self-releasing H_2 gas that generally limits the H_2 production.[10,35] Therefore, methanolysis has been achieved successfully with ultra small size Rh nanocatalysts (average size *ca* 0.7 nm) obtained by using as immobilizing support organic molecular cage (CC3-R) with intrinsically porous skeleton.[252] Rh/CC3-R catalyst (2.4 wt% Rh) achieved RT AB full dehydrogenative methanolysis with a TOF = 215 min^{-1}. The nanocatalyst Rh/CC3-R showed no loss in activity and selectivity over 5 successive cycles of adding AB into the reactor after completion of the previous run. The methanolysis of AB was also achieved for evaluating the catalytic activity of small ruthenium NPs (average size *ca* 2.5 nm, TOF = 304 min^{-1}, see details section 3.4) encapsulated in a crystalline porous coordination cage (PCC),[144] like it was investigated with palladium catalysts[98-100] (up to TOF = 176 min^{-1}, see details section 3.2). The most advanced results described ultra-small Ru fcc NPs (average size *ca* 4.3 nm) formed from pyrolysis of a Ru-loaded MOF at 700 °C. The nanocatalyst achieves the methanolysis of AB with a TOF = 336 min^{-1} at 25 °C (see also section 3.4).[145] The introduction of nickel for bimetallic alloying with these noble-metals was recently reported.[253] Hydroxyapatite[$Ca_{10}(PO_4)_6(OH)_2$]-supported RhNi@HAP, RuNi@HAP, and PdNi@HAP nanoparticles (average size *ca* 1.3 nm) were formed from HAP ion-exchange followed by *in situ* reduction by AB. Consistently, $Rh_{62}Ni_{38}$@HAP, $Ru_{80}Ni_{20}$@HAP, and Pd_{80} Ni_{20}@HAP nanocatalysts achieved the methanolysis of AB at 25 °C with TOF = 120, 59, and 25 min^{-1}, respectively.

H_2 release from AB in other non-aqueous solvent is expected to make easier the regeneration of the starting material from the by-products in comparison with hydrolysis. On the other hand, the use of organic solvent allowed to conduct dehydrogenation with further tandem organic synthesis.[94] Pd-MOF hybrid materials were studied for the H_2 production from AB dehydrogenation carried out at 80 °C in 1,4-dioxane. Various Pd catalysts with Pd content of 4.8 mol%, with respect to AB, were tested and TOF ranging between 1.6 and 3.9 min^{-1} were obtained. Tandem phenylacetylene selective hydrogenation to styrene (with >99% selectivity) was also achieved.

4.2 Other amine-boranes

Hydrazine borane (HB) having a gravimetric hydrogen density of 15.4 wt% is also considered as a potential hydrogen storage material from its hydrolysis or methanolysis. Recent reviews treated the early works and challenges attached to the use of HB and alkali derivatives (*i.e.* lithium, sodium, and potassium hydrazinidoboranes, $MN_2H_3BH_3$, with M = Li, Na, and K).[254,255] Notably, the BH_3 group in HB is easy to hydrolyze in the presence of a suitable catalyst, while for the N_2H_4 group of HB, dehydrogenation is in competition with NH_3 release. Thus, interest on HB arises mainly if N_2H_4 moiety is effectively decomposed and dehydrogenated.[256] Mainly, nickel-based alloyed nanoparticles were used in this purpose for selective dehydrogenation of hydrous hydrazine, $N_2H_4{\cdot}H_2O$, at temperatures over the range of 20–70 °C.[254,255] $Ni_{60}Pt_{40}$ nanoalloys supported on nanoporous carbon (Maxsorb MSC-30) achieved a 100% selective and complete production of H_2 (5 equiv.) with one equiv. of N_2 per mole of $N_2H_4BH_3$ (site-time yield of H_2 was calculated to be 22.2 min^{-1} at 30 °C).[257] It was found to be stable in terms of conserved activity and selectivity over five cycles. However, in general, the catalysts for HB hydrolysis are evaluated in diluted favorable conditions, and the effective gravimetric hydrogen storage capacities remained therefore low (< 2.0 wt%) and somewhat unrealistic for practical implementation.

Cerium oxide-modified Rh-Ni NPs grown on rGO, $Rh_{80}Ni_{20}$@CeOx/rGO, achieved a complete hydrogen production from HB with a TOF = 1.8 min^{-1}.[258] Ni-Mo bimetallic catalytic system without noble metal, $Ni_{90}Cr_{10}$, $Ni_{90}Mo_{10,}$ and $Ni_{80}W_{20}$ nanoparticles achieved incomplete HB hydrolysis with TOF = 16.8, 40.0, and 18.7 min^{-1}, respectively. Note that these results are obtained by only hydrolyzing BH_3 group and not N_2H_4.[259] In a follow-up work, complete HB hydrolysis was achieved using unsupported trimetallic $Cu_{40}Ni_{60}Mo_{100}$ nanoparticles. These were well-dispersed with a mean particle size of 5.9 ± 1.2 nm, in contrast without molybdenum $Cu_{40}Ni_{60}$ nanoparticles achieved much larger size of 21.8 ± 5.7 nm.[260] The catalytic reactions for H_2 production from AB were completed at 50°C with a TOF = 1.8 min^{-1}.

Complete HB dehydrogenation was also achieved using Cr_2O_3-doped Ni-M nanoparticles (M = Pt, Rh, and Ir) that were synthesized via precursors co-reduction at RT.[261] The $Ni_{90}Pt_{10}$-Cr_2O_3 (of lowest Pt content) achieved dehydrogenation of HB with a TOF = 20 min^{-1} at 50 °C. The addition of Cr_2O_3 reduced the size of the bimetallic nanoparticles (average size *ca* 4.5 nm *vs.* 18.7 nm without the dispersant effect of Cr_2O_3) and increased the BET surface area as compared to that of pure $Ni_{90}Pt_{10}$ NPs (20-fold lower). This leads to an increase of the electron density of bimetallic Ni-Pt.

Using noble metal-free $Ni_{50}Fe_{50}$–CeOx/MIL-101, a complete dehydrogenation of HB with 100% H_2 selectivity and a TOF = 5.9 min^{-1} was reported.[262] $Ni_{50}Fe_{50}$–CeOx nanoparticles were immobilized on an MIL-101 support without surfactant by liquid impregnation method. Dispersion and uniform particle size of the $Ni_{50}Fe_{50}$–CeOx nanoparticles (average particle size *ca* 10.3 nm) was attributed to steric restrictions effect of the MIL-101 support (pore sizes of MIL-101 being smaller than 3.4 nm, the nanoparticles are not located into the porosity. Changing MIL-101 for other kinds of MOFs (UiO-66, ZIF-67, ZIF-8), the resultant NiFe–CeOx/MOF catalysts all show good catalytic activity toward HB decomposition, indicating the usefulness of MOF supported NiFe–CeOx catalysts.

$Rh_{50}(MoOx)_{50}$ NPs were prepared without any surfactant and support from the chemical reduction with $NaBH_4$ under ambient condition of $RhCl_3.3H_2O$ and $Na_2MoO_4.2H_2O$ in water. The resultant nanocatalyst achieved complete hydrogen evolution from HB with 100% H_2 selectivity in an alkaline aqueous solution, providing a TOF = 33.3 min^{-1} at 50 °C.[263] The catalytic performance was attributed to the small particles size (mean size of the dispersed nanoparticles *ca* 3.8 nm *vs* 8.8 nm for pure Rh NPs) and their low crystallinity. The MoOx presence thus improved Rh NPs dispersion, reduced their average size, and modified the electronic structure of the nanocatalyst in which strong basic sites of Rh nanoparticles are induced by the MoOx dopant.

Following an approaching concept, NiFe nanoparticles were decorated by the lanthanum hydroxide $La(OH)_3$ via a one-step co-reduction of $NiCl_2.6H_2O$, $FeSO_4.7H_2O$, and $La(NO_3)_3.6H_2O$ by $NaBH_4$ in water without surfactant or support under ultrasonic irradiation.[264] It was found that the presence of $La(OH)_3$ yielded NiFe nanoparticles having a smaller average size (2.4 nm against *ca* 15 nm, respectively) and lower crystallinity. Analogous $NiFeLt(O)_x$ doped with rare-earth hydroxide (L*t* = Dy, Ce, Gd, Sm, Eu, Nd, Pr and Yb at 7.0 mol%) have been synthesized and studied for N_2H_4 only dehydrogenation. The optimized lanthanum hydroxide nanocatalyst $Ni_{88}Fe_{12}[La(OH)_3]_7$ achieved from HB hydrolysis a TOF = 1.4 min^{-1} for the production of 5 equiv H_2 at 50 °C. As exemplified above, non-Rh and non-Ni catalysts did not achieve clean and complete hydrolysis of HB (*ca.* 5 equiv. H_2 and 1 equiv. N_2). The recently reported bimetallic Co-Ru nanoparticles stabilized by PVP surfactant CoRu@PVP were no exception.[265]

Ethylene diamine bisborane (EDAB, $H_3B{\leftarrow}NH_2CH_2CH_2H_2N{\rightarrow}BH_3$)[266] is also a potential H_2 storage material with a high hydrogen molar content of 16.1 %. EDAB has been originally tested under thermal dehydrogenation.[267] The H_2 release from hydrogen rich carbon-boron nitrogen compounds, including the decomposition of EDAB able to provide 2 equiv. H_2, has been recently reviewed.[268] Temperature-monitoring studies of EDAB suggested that it is likely to be more stable than AB when stored in the solid-sate even at relatively high ambient temperatures for prolonged periods.

Ozay's group originally studied Cu, Co, and Ni particles with average sizes of 75-150 nm that were formed in polymeric-(acrylic acid-co-vinyl-imidazole) hydrogel network structures, as catalysts for the hydrolysis reaction of EDAB.[269] Hydrogels are 3D cross-linked polymeric networks which, by swelling, retains water up to several hundred times their dry weight in aqueous media. Their hydrophilic functional groups and anionic structures are thus relevant for metal ions as absorbent material support. Cu-based materials were found to be more active catalysts in the reaction, with TOF = 0.357, 0.191, and 0.176 min^{-1} at 30 °C for Cu, Co, and Ni catalysts, respectively. Reuse tests determined that the best catalyst maintained its activity at 85% after 5 consecutive runs. Following this work, this group described several systems for EDAB hydrolysis, including: *i*) zerovalent Co, Ni, and Cu composite catalysts with fly ash support from coal combustion,[270] *ii*) 10 nm size Ru^0 nanoparticles supported on hydroxyethyl-base interpenetrating polymeric network hydrogel (TOF = 2.3 min^{-1} at 30 °C, retaining *ca* 80% of catalytic activity after the 5th cycling run),[271] *iii*) 12 nm size Cu^0 nanoparticles stabilized by cyclen derivative hydrogel networks (TOF = 1.1 min^{-1} at 30 °C, retaining *ca* 85% of catalytic activity after the 10th cycling run),[272] *iv*) 20 nm size Pd^0 nanoparticles supported on polymeric-(3-sulfopropyl acrylate) hydrogel (TOF = 5.9 min^{-1} at 30 °C, retaining *ca* 87% of catalytic activity after the 10th cycling run).[273] In all these works, the exact hydrolytic decomposition mode of EDAB and the H_2 production mechanism is still unclear and deserves more studies. However, measurement of ratio $nH_2/nEDAB = 5$ was obtained for instance with the Ru^0 nanocatalyst,[271] leading to the hypothetical assumption that 2 equiv. of H_2 came from EDAB and 3 equiv. came from water, providing to the active catalyst a double interest.

4.3 Miscellaneous related recent advances

Bimetallic nanocatalysts with nearly atomically dispersed Co and Ni atoms were synthesized using effects induced by strong metal-supports interactions with molybdenum carbide (α-MoC).[274] α-MoC support is capable of activating water and maintaining a high surface coverage of hydroxyl species at moderate temperature (30 °C). The $Co_{51}Ni_{49}$/α-MoC highly dispersed Co–Ni bimetallic catalysts supported on α-MoC for hydrogen production from the hydrolysis of ammonia borane was observed by chemical mapping at the atomic level (Figure 47). The scanning transmission electron microscopy (STEM) images of the nanocatalysts revealed that the α-MoC has a porous structure consisting of irregular shaped particles with a grain size of *ca* 5−10 nm Figure 47, a and b).[274]

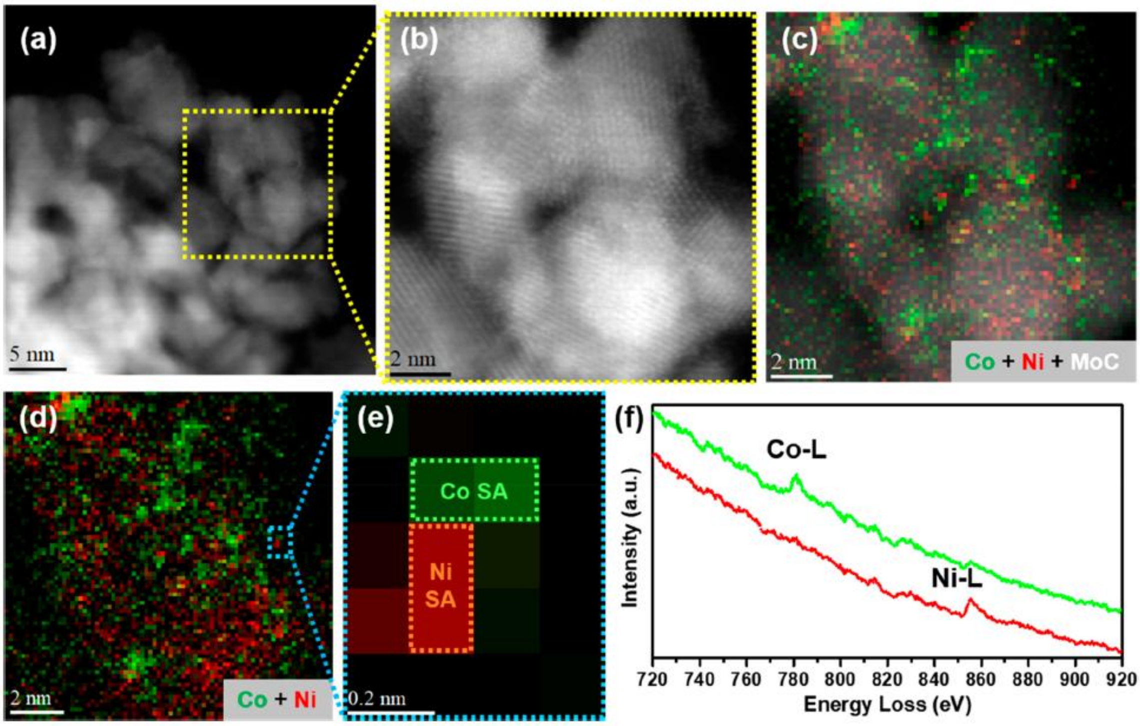

Figure 47. (a) HAADF-STEM image of 1.5Co1.5Ni/α-MoC. (b) High resolution HAADF STEM image of the highlighted area in (a). (c) Overlay of Co and Ni EELS maps with the simultaneously recorded HAADF-STEM image. (d) Overlay of the projected spatial distribution of Co and Ni. (e) Enlarged image of the highlighted pixels in (d). The size of each pixel is 0.15 nm. (f) EELS spectra of the Co single atom and the Ni single atom in the corresponding regions in (e). Reprinted with permission from ref 274. Copyright 2020 American Chemical Society.

To confirm the presence of atomically dispersed Co and Ni, atomic-scale chemical imaging via STEM-EELS mapping was achieved. Such technique depicted that most of the Co and Ni loadings are atomically dispersed at high density on the surface of α-MoC (Figure 47, c and d). Spatial distribution of the Co and Ni species is highly correlated. Figure 47, e and f show a pair of adjacent Co and Ni atoms that are less than 0.3 nm apart. The close proximity of the Ni and Co atoms suggests that they may be able to interact with the same substrate during catalytic reaction. The $Co_{51}Ni_{49}$/α-MoC catalysts (α-MoC loaded with Co 1.5 wt% and Ni 1.5 wt%) reached TOF = 128 min^{-1} at 25 °C, which was found to be 3-4 fold higher than that of the monometallic analogues Co/α-MoC and Ni/α-MoC catalysts (3 wt% metal). The changes in the reaction media from a neutral to a basic condition enhanced the hydrolysis TOF up to 321 min^{-1}. These catalytic performances were attributed to the nearly atomically dispersed Co and Ni atoms, which interestingly opens to the question of cooperative two-single-atom heterogeneous catalysts for AB hydrolysis. This transition from ultra-small nanoparticles to nearly atomically dispersed,[43,100,123,145,155,252] down to single-atom catalysts (SACs) is thus a challenge for the future of such hydrogen production reactions which already started to be addressed.

Single-atom catalysts have been studied as platform to investigate metal–support interactions to avoid most of the interference from the size, shape, and orientation of the metal particles.[275] SACs can be advantageously combined with phase-transition material supports, which are pertinent to study metal–support interactions in a catalysis process because the band structure of the substrate can be modulated while keeping the spatial distribution of the single atoms and the active sites unchanged. Vanadium dioxide, VO_2, undergoes such metal–insulator phase transition at approximately 67-68 °C. A single-atom catalyst consisting of isolated Rh atoms uniformly dispersed on the surface of VO_2 nanorods (Rh/VO_2, Rh 0.5 wt%) was synthesized by injecting a Na_3RhCl_6 solution into an aqueous solution containing VO_2 nanorods, followed by stirring at 300 rpm at RT for 1 h. The Rh^{3+} ions were reduced to Rh^{+} by $V4^{+}$ in the VO_2 nanorods as the average molar ratio of leached V species to supported Rh single atoms was determined to be *ca* 2:1 (two V^{5+} formed for one Rh^{3+} ion reduced). Individual Rh atoms were observed as bright spots (marked with white circles Figure 48) uniformly dispersed on the surface of VO_2.

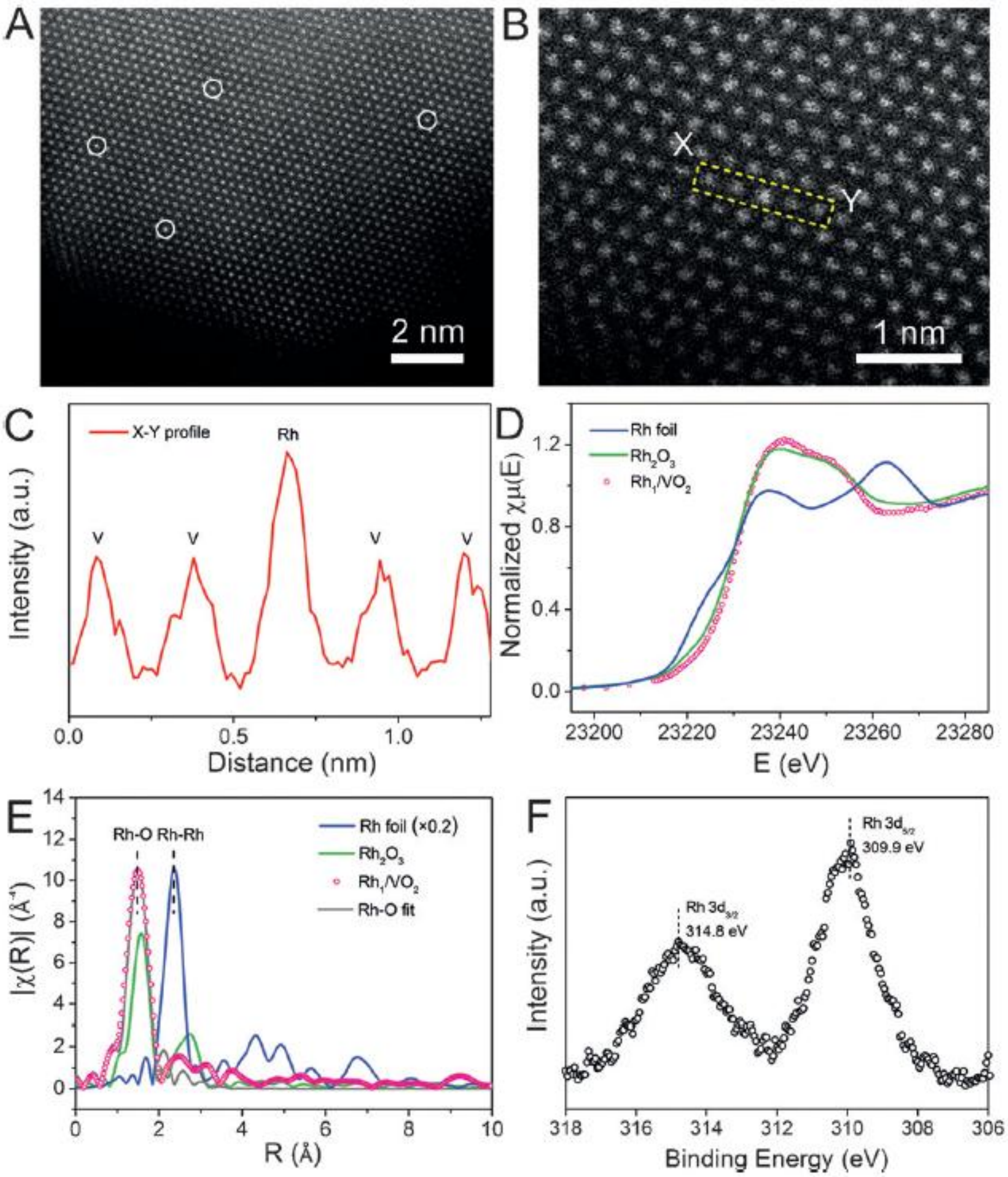

Figure 48. A) HAADF-STEM and B) magnified HAADF-STEM images of Rh_1/VO_2. C) Intensity profile along the X–Y line in (B). D) Rh K-edge XANES spectra for Rh_1/VO_2, Rh_2O_3, and Rh foil. E) Rh K-edge EXAFS spectra in R space for Rh_1/VO_2 with the corresponding fitted curve, Rh_2O_3, and Rh foil. F) XPS spectrum of Rh 3d for Rh_1/VO_2. Reprinted with permission from ref 275. Copyright 2017 Wiley-VCH Verlag GmbH & Co. KGaA, Weinheim.

Analysis of a magnified HAADF-STEM image of Rh/VO_2 showed that the Rh atoms exactly occupied the positions of V atoms (Figure 48, B).[275] The intensity profile (Figure 48 C) along the X-Y line in Figure 48 B corroborated the presence of isolated Rh atoms. The extended X-ray absorption fine structure (EXAFS) analysis of Rh/VO_2 exhibited a prominent peak at approximately 2.0 Å from the Rh–O shell with a coordination number *ca* 6.4 without typical Rh–Rh contributions at longer distances (>2.0 Å), confirming the dispersion of isolated Rh atoms. The complete hydrolysis of AB (3 equiv. H_2) was performed to study how the metal–support interactions in Rh/VO_2 changed upon the metal–insulator transition. Without catalyst or with VO_2 nanorods only, no gas evolution from AB was detected. AB hydrolysis achieved TOF = 72 and 48 min^{-1} at 80 and 60 °C, respectively. After five rounds of reaction at these temperatures, the SAC conserved more than 95% of its original reactivity and its atomically dispersed structures was unchanged. The TOF number decreased when the pH value increased from 6.0 to 8.0, indicating a positive correlation between the H^+ concentration and the reaction rate. The catalytic performance of Rh/VO_2 was correlated with the highest occupied state of the single Rh atoms (and generalized to other metals, M = Fe, Co, Ni, Cu, Ag, and Au).[275] Indeed, changes in the apparent activation energies of AB hydrolysis were measured for M/VO_2 that were induced by the phase transformation of theVO_2 support (insulator–metal phase transition). Thus, a quantitative relationship between the catalytic performance and metal–support interactions was established. The highest occupied state of the single Rh atom is decisive because of its influence over electron transfer to H^+ in the determining step of the AB hydrolysis. Notably, this issue of lowest apparent activation energy for AB hydrolysis has been recently surveyed, showing the best results with graphene and CNT supports ($E_a < 15$ kJ mol^{-1}).[58]

Besides new research pathways opened by SACs,[276,277] in the related field of homogeneous catalysis –that is classically focused on molecular metal complexes synthesis and ligands effects–, the catalytic dehydrogenation of (di)amine-boranes with a metal-free geometrically constrained phosphine-borane Lewis Pair has been described.[278] This work complements earlier reports on P/Al-based frustrated Lewis Pairs, and further opens a road to unexplored concerted nonmetal reactivity, which is probably worth to extend to heterogeneized systems.

In the course of the preparation of the present review, pertinent works have been reported, which are worth to be briefly mentioned. An overview of the recent achievements in the topic of nanocatalysis of hydrogen production from liquid-phase hydrogen storage materials, including metal-boron hydrides, borane-nitrogen compounds, and liquid organic hydrides have been provided.[279] A general overview of noble-metal-free nanocatalysts for hydrogen production from boron- and nitrogen-based hydrides, including metal boride and metal phosphide as well as carbide/nitride has been reported.[159] The vast and clearly system-dependent topic of mechanistic approaches for AB hydrolysis, which is out of the scope of the present review, has been reviewed recently.[48] Finally, it is worth quoting the survey work by Demirci group which addresses the "hydrogen energy" challenge from an holistic perspective, and lately focused on the general technological readiness of the H_2 production by hydrolysis of B(–N)–H compounds (including technology readiness level, TRL stages),[280] and the state-of-the art of amidoboranes and hydrazinidoboranes for hydrogen storage.[281]

5. CONCLUSIONS

The body of work condensed in this review highlights several important points regarding the remaining challenges for the production of H_2 from AB. Beyond the race for the highest possible TOF, the recycling and the stability of the catalyst, the importance of the synthesis method appears, as often in nanoscience, as an essential point. The choice of the chemical elements and their arrangement in the complex edifice of the nanostructure to form an efficient catalyst is crucial. The synthesis implemented will inevitably have an influence. A material with the same composition can have very different performances depending on its preparation mode. The electronic structure of the material, on which the reactivity will depend, depends on this mastery of their preparation. Even more than the observation of the "synergies" between elements (a word often used but which translates a deleterious magic character), it appears obvious that the community must seize this question to reveal the electronic structures of the complex edifices to control their properties. This requires a multidisciplinary approach bringing together chemists and physicists, both experimental and theoretical. In addition, for the deployment of catalysts and the development of the hydrogen sector, engineers, technicians and industrialists will also have to take part in the work. The challenges are numerous but the knowledge and know-how exist to meet them.

---

[1]. L. Schlapbach, A. Züttel, *Nature*, **2001**, *414*, 353–358.

[2]. N. Armaroli, V. Balzani, *ChemSusChem*, **2011**, *4*, 21–36.

[3]. S. Niaz, T. Manzoor, A. H. Pandith, *Renew. Sustain. Energy Rev.*, **2015**, *50*, 457–469.

[4]. T. B. Marder, *Angew. Chem. Int. Ed.*, **2007**, *46*, 8116–8118.

[5]. F. H. Stephens, V. Pons, T. Baker, *Dalton Trans.*, **2007**, 2613–2626.

[6]. C. W. Hamilton, R. T. Baker, A. Staubitz, I. Manners, *Chem. Soc. Rev.*, **2009**, *38*, 279–293.

[7]. U. B. Demirci, O. Akdim, P. Miele, *Int. J. Hydrog. Energy*, **2009**, *34*, 2638–2645.

[8]. H.-L. Jiang, S. K. Singh, J.-M. Yan, X.-B. Zhang, Q. Xu, *ChemSusChem*, **2010**, *3*, 541–549.

[9]. N. C. Smythe, J. C. Gordon, *Eur. J. Inorg. Chem.*, **2010**, 509–521.

[10]. A. Staubitz, A. P. M. Robertson, I. Manners, *Chem. Rev.*, **2010**, *110*, 4079–4124.

[11]. H.-L. Jiang, Q. Xu, *Catal. Today*, **2011**, *170*, 56–63.

[12]. K. Wang, J.-G. Zhang, T.-T. Man, M. Wu, C.-C. Chen, *Chem. Asian J.*, **2013**, *8*, 1076–1089.

[13]. A. K. Singh, Q. Xu, *ChemCatChem*, **2013**, *5*, 652–676.

[14]. M. Zahmakiran, S. Özkar, *Top. Catal.*, **2013**, *56*, 1171–1183.

[15]. W.-W. Zhan, Q.-L. Zhu, Q. Xu, *ACS Catal.*, **2016**, *6*, 6892−6905.

[16]. X. Zhang, L. Kam, R. Trerise, T. J. Williams, *Acc. Chem. Res.*, **2017**, *50*, 86−95.

[17]. U. B. Demirci, *Int. J. Hydrog. Energy*, **2017,** *42*, 9978–10013.

[18]. S. Akbayrak, S. Özkar, *Int. J. Hydrog. Energy*, **2018**, *43*, 18592–18606.

[19]. M. Liu, L. Zhou, X. Luo, C. Wan, L. Xu, *Catalysts*, **2020**, *10*, 788–823.

[20]. D. Teichmann, W. Arlt, P. Wasserscheid, R. Freymann, *Energy Environ. Sci.*, **2011**, *4*, 2767–2773.

[21]. P. Preuster, C. Papp, P. Wasserscheid, *Acc. Chem. Res.*, **2017**, *50*, 74−85.

[22]. L. Zhou, L. Sun, L. Xu, C. Wan, Y. An, M. Ye, *Catalysts*, **2020**, *10*, 648–669.

[23]. M. R. Axet, K. Philippot, *Chem. Rev.*, **2020**, *120*, 1085−1145.

[24]. I. G. Green, K. M. Johnson, B. P. Roberts, *J. Chem. Soc. Perkin Trans.* **1989**, *2*, 1963–1989.

[25] C. A. Jaska, K. Temple, A. J. Lough, I. Manners, *J. Am. Chem. Soc.*, **2003**, *125*, 9424−9434.

[26]. Y. Chen, J. L. Fulton, J. C. Linehan, T. Autrey, *J. Am. Chem. Soc.*, **2005**, *127*, 3254−3255.

[27]. M. Zahmakiran, T. Ayvali, K. Philippot, *Langmuir*, **2012**, *28*, 4908−4914.

[28] M. Zahmakiran, K. Philippot, S. Özkar, B. Chaudret, *Dalton Trans.*, **2012**, *41*, 590–598.

[29]. D. Sun, V. Mazumder, Ö. Metin, S. Sun, *ACS Nano*, **2011**, *5*, 6458–6464.

[30]. Q. Xu, M. Chandra, *J. Power Sources*, **2006**, *163*, 364–370.

[31]. M. Chandra, Q. Xu, *J. Power Sources*, **2007**, *168*, 135–142.

[32]. J.-M. Yan, X.-B. Zhang, S. Han, H. Shioyama, Q. Xu, *Angew. Chem. Int. Ed.*, **2008**, *47*, 2287–2289.

[33]. F. Durap, M. Zahmakiran, S. Özkar, *Appl. Catal. A Gen.*, **2009**, *369*, 53–59.

[34]. P. Veeraraghavan, P. D. Gagare, *Inorg. Chem.*, **2007**, *46*, 7810–7817.

[35]. S. Özkar, *Int. J. Hydrog. Energy*, **2020**, *45*, 7881–7891.

[36]. S. Akbayrak, Y. Tonbul, S. Özkar, *Appl. Catal. B Environ.*, **2016**, *198*, 162–170.

[37]. C. Du, Q. Ao, N. Cao, L. Yang, W. Luo, G. Cheng, *Int. J. Hydrog. Energy*, **2015**, *40*, 6180–6187.

[38]. W. Chen, J. Ji, X. Duan, G. Qian, P. Li, X. Zhou, D. Chen, W. Yuan, *Chem. Commun.* **2014**, *50*, 2142−2144.

[39]. J. Manna, S. Akbayrak, S. Özkar, *Appl. Catal. B Environ.*, **2017**, *208*, 104–115.

[40]. J. Chen, Z.-H. Lu, Y. Wang, X. Chen, L. Zhang, *Int. J. Hydrog. Energy*, **2015**, *40*, 4777−4785.

[41]. P.-Z. Li, A. Aijaz, Q. Xu, *Angew. Chem. Int. Ed.*, **2012**, *51*, 6753–6756.

[42]. P. Liu, X. Gu, K. Kang, H. Zhang, J. Cheng, H. Su, *ACS Appl. Mater. Interfaces*, **2017**, *9*, 10759−10767.

[43]. M. Kaya, M. Zahmakiran, S. Özkar, M. Volkan. *ACS Appl. Mater. Interfaces*, **2012**, *4*, 3866−3873.

[44]. M. Dinc, Ö. Metin, S. Özkar, *Top. Catal.*, **2012**, *183*, 10−16.

[45]. M. Rakap, *Appl. Catal. B Environ.*, **2015**, *163*, 129–134.

[46]. L. Yang, J. Su, W. Luo, G. Cheng, *ChemCatChem*, **2014**, *6*, 1617−1625.

[47]. J. R. Vance, A. Schäfer, A. P. M. Robertson, K. Lee, J. Turner, G. R. Whittell, I. Manners, *J. Am. Chem. Soc.*, **2014**, *136*, 3048−3064.

[48]. H. Wu, Y. Cheng, Y. Fan, X. Lu, L. Li, B. Liu, B. Li, S. Lu, *Int. J. Hydrog. Energy*, **2020**, *45*, 30325–30340.

[49]. Q. Yao, W. Shi, G. Feng, Z.-H. Lu, X. Zhang, D. Tao, D. Kong, X. Chen, *J. Power Sources*, **2014**, *257*, 293–299.

[50]. G. P. Rachiero, U. B. Demirci, P. Miele, *Int. J. Hydrog. Energy*, **2011**, *36*, 7051–7065.

[51]. S. Akbayrak, Y. Tonbul, S. Özkar, *Dalton Trans.*, **2016**, *45*, 10969–10978.

[52]. K. Mori, K. Miyawaki, H. Yamashita, *ACS Catal.*, **2016**, *6*, 3128−3135.

[53]. L. Zhang, Y. Wang, J. Li, X. Ren, H. Lv, X. Su, Y. Hu, B. Liu, *ChemCatChem*, **2018**, *10*, 4910–4916.

---

[54]. S. Akbayrak, S. Özkar, *ACS Appl. Mater. Inter.*, **2012**, ***4***, 6302–6310.

[55]. Q. Yao, Z.-H. Lu, Y. Jia, X. Chen, X. Liu, *Int. J. Hydrog. Energy*, **2015**, **40**, 2207–2215.

[56]. J. Shen, L. Yang, K. Hu, W. Luo, G. Cheng, *Int. J. Hydrogen Energy*, **2015**, *40*, 1062−1070.

[57]. Ö. Metin, E. Kayhan, S. Özkar, J. J. Schneider, *Int. J. Hydrogen Energy*, **2012**, *37*, 8161–8169.

[58]. C. Y. Alpaydin, S. K. Gülbay, C. O. Colpan, *Int. J. Hydrogen Energy*, **2020**, *45*, 3414–3434.

[59]. Z. Wen, J. Wu, G. Fan, *Catalysts*, **2020**, *10*, 1037–1049.

[60]. Z. Wang, H. Zhang, L. Chen, S. Miao, S. Wu, X. Hao, W. Zhang, M. Jia, *J. Phys. Chem. C*, **2018**, *122*, 12975−12983.

[61]. Q.-L. Zhu, J. Li, Q. Xu, *J. Am. Chem. Soc.*, **2013**, *135*, 10210−10213.

[62]. F. Fu, C. Wang, Q. Wang, A. M. Martinez-Villacorta, A. Escobar, H. Chong, X. Wang, S. Moya, L. Salmon, E. Fouquet, J. Ruiz, D. Astruc, *J. Am. Chem. Soc.*, **2018**, *140*, 10034−10042.

[63]. Q. Song, W. D. Wang, X. Hu, Z. Dong, *Nanoscale*, **2019**, *11*, 21513–21521.

[64]. Q. Sun, N. Wang, Q. Xu, J. Yu, *Adv. Mater.*, **2020**, *32*, 2001818–2001870.

[65]. R. F. Schulte, C. Pisut, U.S. Geological Survey, Mineral Commodity Summaries, Platinum-Group Metals, can be found at https://www.usgs.gov/centers/nmic/platinum-group-metals-statistics-and-information.

[66]. The high price volatility of rhodium (and to a lesser extent for palladium) is attributable to their main use in catalytic converters. Automotive industry makes up 80% of the demand for these precious metals. With global emissions standards rising, automakers need such resources. Mine strikes in South Africa in 2019 is another reason for the price explosion

(supply-and-demand issue). Electric vehicles still not being in mainstream use automakers in near future will continue seeking the best environmental version of gasoline-driven vehicles. Thus, catalytic converters will probably continue to be in demand, meaning rhodium and palladium will continue to be valued.

[67]. R. Ferrando, J. Jellinek, R. L. Johnston, *Chem. Rev.*, **2006**, *108*, 845–910.

[68]. Y. Tonbul, S. Akbayrak, S. Özkar, *J. Colloid Interface Sci*., **2019**, *553*, 581–587.

[69]. R. Lu, C. Xu, Z. Yang, L. Zhou, J. Wu, Y. Wang, Y. Zhang, G. Fan, *Int. J. Hydrogen Energy*, **2020**, *45*, 1640–1648.

[70]. S. Akbayrak, Y. Tonbul, S. Özkar, *ACS Sustainable Chem. Eng*., **2020**, *8*, 4216–4224.

[71]. M. Hu, M. Ming, C. Xu, Y. Wang, Y. Zhang, D. Gao, J. Bi, G. Fan, *ChemSusChem*, **2018**, *11*, 3253–3258.

[72]. J. Chen, M. Hu, M. Ming, C. Xu, Y. Wang, Y. Zhang, J. Wu, D. Gao, J. Bi, G. Fan, *Int. J. Hydrogen Energy*, **2018**, *43*, 2718–2725.

[73]. R. Lu, M. Hu, C. Xu, Y. Wang, Y. Zhang, B. Xu, D. Gao, J. Bi, G. Fan, *Int. J. Hydrogen Energy*, **2018**, *43*, 7038–7045.

[74]. W. Luo, X. Zhao, W. Cheng, Y. Zhang, Y. Wang, G. Fan, *Nanoscale Adv.*, **2020**, *2*, 1685–1693.

[75]. H. Liu, C. Xu, R. Lu, Q. Wang, J. Wu, Y. Wang, Y. Zhang, T. Sun, G. Fan, *Int. J. Hydrogen Energy*, **2019**, *44*, 16548–16556.

[76]. C. Xu, M. Hu, G. Fan, Y. Wang, D. Gao, J. Bi, *Dalton Trans.*, **2018**, *47*, 2561–2567.

[77]. M. A. Gunawan, O. Moncea, D. Poinsot, M. Keskes, B. Domenichini, O. Heintz, R. Chassagnon, F. Herbst, R. M. K. Carlson, J. E. P. Dahl, A. A. Fokin, P. R. Schreiner, J.-C. Hierso, *Adv. Funct. Mater.*, **2018**, *28*, 1705786–1705801.

[78]. S. Akbayrak, M. Kaya, M. Volkan, S. Özkar, *Appl. Catal. B Environ.*, **2014**, *147*, 387–393.

[79]. H. Jia, X.-J. Liu, X. Chen, X.-X. Guan, X.-C. Zheng, P. Liu, *Int. J. Hydrogen Energy*, **2017**, *42*, 28425–28433.

[80]. J. Wang, Y.-L. Qin, X. Liu, X.-B. Zhang, *J. Mater. Chem.*, **2012**, *22*, 12468−12470.

[81]. N. S. Çiftci, Ö. Metin, *Int. J. Hydrogen Energy*, **2014**, *39*, 18863–18870.

[82]. C. Yu, X. Guo, M. Shen, B. Shen, M. Muzzio, Z. Yin, Q. Li, Z. Xi, J. Li, C. T. Seto, S. Sun, *Angew. Chem. Int. Ed.*, **2018**, *57*, 451–455.

[83]. H. Göksu, S. F. Ho, Ö. Metin, K. Korkmaz, A. M. Garcia, M. S. Gültekin, S. Sun, *ACS Catal.*, **2014**, *4*, 1777−1782.

[84]. Y.-H. Zhou, Z. Zhang, S. Wang, N. Williams, Y. Cheng, S. Luo, J. Gu, *Int. J. Hydrogen Energy*, **2018**, *43*, 18745–18753.

[85]. W. Wang, Z.-H. Lu, Y. Luo, A. Zou, Q. Yao, X. Chen, *ChemCatChem*, **2018**, *10*, 1620–1626.

[86]. Y. Tong, X. F. Lu, W. N. Sun, G. D. Nie, L. Yang, C. Wang, *J. Power Sources*, **2014**, *261*, 221–226.

[87]. N. Z. Shang, C. Feng, S. T. Gao, C. Wang, *Int. J. Hydrogen Energy*, **2016**, *41*, 944–950.

[88]. H. Kahri, M. Sevim, Ö. Metin, *Nano Res.*, **2017**, *10*, 1627–1640.

[89]. H. Ç. Kazici, F. Yildiz, M. S. Izgi, B. Ulas, H. Kivrak, *Int. J. Hydrogen Energy*, **2019**, *44*, 10561–10572.

[90]. H. Göksu, H. Can, K. Sendil, M. S. Gültekin, Ö. Metin, *Appl. Catal. A Gen.*, **2014**, *488*, 176–182.

[91]. Q. Yang, Y.-Z. Chen, Z. U. Wang, Q. Xu, H.-L. Jiang, *Chem. Commun.*, **2015**, *51*, 10419–10422.

[92]. The double solvent approach (DSA) use an aqueous solution for metal with a volume slightly less than the pore volume of the support. This was pumped dropwise into the hydrophobic hexane containing the suspended support. Given the hydrophilic nature of the inner pore environment of MOF, the aqueous solution was readily absorbed into the pores by capillary force during the liquid impregnation process. The metal ions loaded are subsequently reduced in situ.

[93]. D. Sun, S. Jang, S.-J. Yim, L. Ye, D.-P. Kim, *Adv. Funct. Mater.* **2018**, *28*, 1707110–1707117.

[94]. V. R. Bakuru, B. Velaga, N. R. Peela, S. B. Kalidindi, *Chem. Eur. J.*, **2018**, *24*, 15978–15982.

[95]. X. Li, L. Song, D. Gao, B. Kang, H. Zhao, C. Li, X. Hu, G. Chen, *Chem. Eur. J.*, **2020**, *26*, 4419–4424.

[96]. Y. Liu, Q. Wang, L. Wu, Y. Long, J. Li, S. Song, H. Zhang, *Nanoscale*, **2019**, *11*, 12932–12937.

[97]. P. Xu, W. Lu, J. Zhang, L. Zhang, *ACS Sustainable Chem. Eng.*, **2020**, *8*, 12366–12377.

[98]. X. Guo, C. Yu, Z. Yin, S. Sun, C. T. Seto, *ChemSusChem*, **2018**, *11*, 1617–1620.

[99]. M. Muzzio, H. Lin, K. Wei, X. Guo, C. Yu, T. Yom, Z. Xi, Z. Yin, S. Sun, *ACS Sustainable Chem. Eng.*, **2020**, *8*, 2814−2821.

[100]. X. Yang, J.-K. Sun, M. Kitta, H. Pang, Q. Xu, *Nat. Catal.*, **2018**, *1*, 214–220.

[101]. XRD patterns of as-synthesized Au, Pd and Pd–Au nanoparticles were compared that exhibited for Pd–Au well-defined diffraction peaks in the position between the corresponding Au and Pd nanoparticles peaks, indicating the formation of the alloy structure, see: Ö. Metin, X. Sun, S. Sun, *Nanoscale*, **2013**, *5*, 910−912.

[102]. M. Gulcan, M. Zahmakiran, S. Özkar, *Appl. Catal. B*, **2014**, *147*, 394−401.

---

[103]. S. Karaboga, S. Özkar, *Appl. Surf. Sci.*, **2019**, *487*, 433−441.

[104]. Z. Wen, Q. Fu, J. Wu, G. Fan, *Nanomaterials*, **2020**, *10*, 1612−1622.

[105]. N. M. Patil, M. A. Bhosale, B. M. Bhanage, *RSC Adv.*, **2015**, *5*, 86529−86535.

[106]. M. Chandra, Q. Xu, *J. Power Sources*, **2006**, *156*, 190−194.

[107]. A. Aijaz, A. Karkamkar, Y. J. Choi, N. Tsumori, E. Rönnebro, T. Autrey, H. Shioyama, Q. Xu, *J. Am. Chem. Soc.*, **2012**, *134*, 13926–13929.

[108]. M. A. Khalily, H. Eren, S. Akbayrak, H. H. Susapto, N. Biyikli, S. Özkar, M. O. Guler, *Angew. Chem. Int.*, **2016**, *55*, 12257–12261.

[109]. Z. Li, T. He, D. Matsumura, S. Miao, A. Wu, L. Liu, G. Wu, P. Chen, *ACS Catal.* **2017**, *7*, 6762−6769.

[110]. X. Cui, H. Li, G. Yu, M. Yuan, J. Yang, D. Xu, Y. Hou, Z. Dong, *Int. J. Hydrogen Energy*, **2017**, *42*, 27055–27065.

[111]. Q. Wang, F. Fu, S. Yang, M. M. Moro, M. de los Angeles Ramirez, S. Moya, L. Salmon, J. Ruiz, D. Astruc, *ACS Catal.*, **2019**, *9*, 1110−1119.

[112]. Y. Ju, J. Kim, *Korean J. Chem. Eng*., **2020**, *37*, 1387–1393.

[113]. Y. Liu, M. Gao, W. Yang, Y. Yu, *ChemistrySelect*, **2020**, *5*, 7632–7637.

[114]. K. C.-F. Leung, S. Xuan, X. Zhu, D. Wang, C.-P. Chak, S.-F. Lee, W. K.-W. Ho, B. C.-T. Chung, *Chem. Soc. Rev.*, **2012**, *41*, 1911–1928.

[115]. M. Aksoy, Ö. Metin, *ACS Appl. Nano Mater.*, **2020**, *3*, 6836−6846.

[116]. S. Rej, L. Mascaretti, E. Y. Santiago, O. Tomanec, S. Kment, Z. Wang, R. Zboril, P. Fornasiero, A. O. Govorov, A. Naldoni, *ACS Catal.*, **2020**, *10*, 5261−5271.

[117]. P. Lara, K. Philippot, A. Suarez, *ChemCatChem*, **2019**, *11*, 766–771.

[118]. B. Sen, A. Aygun, A. Savk, M. H. Çalimi, M. F. Fellah, F. Sen, *Sci. Rep.*, **2019**, *9*, 15543–15554.

[119]. M. Navlani-Garcia, K. Mori, A. Nozaki, Y. Kuwahara, H. Yamashita, *Appl. Catal. A Gen.*, **2016**, *527*, 45–52. The B5-type sites are defined as consisting of five metal atoms in a 3D arrangement with three Ru atoms in one layer (as a kind of terrace) and two further Ru in the layer directly above this at a monoatomic step on a Ru (0001) terrace. The majority of such active sites were recognized to be favorably present at edges related to low-coordinated surface atoms, e.g., edge atoms on (110) and (113) planes and formed only on medium-sized nanoparticles with a mean diameters of 1.5–7.0 nm. The specific contribution of such unique catalytic sites in the AB dehydrogenation would come from strong physical adsorption of nitrogen, thus efficiently boosting structure-sensitive catalytic reactions.

[120]. G. Chen, R. Wang, W. Zhao, B. Kang, D. Gao, C. Li, J. Y. Lee, *J. Power Sources*, **2018**, *396*, 148–154.

[121]. C. Xu, M. Ming, Q. Wang, C. Yang, G. Fan, Y. Wang, D. Gao, J. Bi, Y. Zhang, *J. Mater. Chem. A*, **2018**, *6*, 14380–14386.

[122]. G. Fan, Q. Liu, D. Tang, X. Li, J. Bi, D. Gao, *Int. J. Hydrogen Energy*, **2016**, *41*, 1542–1549.

[123]. S. Zhang, L. Zhou, M. Chen, *RSC Adv.*, **2018**, *8*, 12282–12291.

[124]. H. Wang, C. Xu, Q. Chen, M. Ming, Y. Wang, T. Sun, Y. Zhang, D. Gao, J. Bi, G. Fan, *ACS Sustainable Chem. Eng.*, **2019**, *7*, 1178−1184.

[125]. H. Chu, N. Li, X. Qiu, Y. Wang, S. Qiu, J.-L. Zeng, Y. Zou, F. Xu, L. Sun, *Int. J. Hydrogen Energy*, **2019**, *44*, 29255–29262.

[126]. H. Chu, N. Li, S. Qiu, Y. Zou, C. Xiang, F. Xu, L. Sun, *Int. J. Hydrogen Energy*, **2019**, *44*, 1774–1781.

[127]. Y. Liu, X. Yong, X. Yong, Z. Liu, Z. Chen, Z. Kang, S. Lu, *Adv. Sustainable Syst.*, **2019**, 1800161–1800170.

---

[128]. W. Cheng, X. Zhao, W. Luo, Y. Zhang, Y. Wang, G. Fan, *ChemNanoMat*, **2020**, *6*, 1251–1259.

[129]. N. Li, C. Gao, S. Qiu, H. Chu, Y. Zou, C. Xiang, H. Zhang, E. Yan, F. Xu, L. Sun, *Recent Pat. Mater. Sci.*, **2018**, *11*, 65–70.

[130]. S. Akbayrak, G. Çakmak, T. Öztürk, S. Özkar, *Int. J. Hydrogen Energy*, **2021**, *46*, 13548–13560.

[131]. P. Pachfule, X. Yang, Q.-L. Zhu, N. Tsumori, T. Uchida, Q. Xu, *J. Mater. Chem. A*, **2017**, *5*, 4835–4841.

[132]. J. Zhang, J. Li, L. Yang, R. Li, F. Zhang, H. Dong, *Int. J. Hydrogen Energy*, **2021**, *46*, 3964–3973.

[133]. D. Genis, B. C. Filiz, S. K. Depren, A. K. Figen, *Microporous Mesoporous Mater.*, **2020**, *305*, 110363–110374.

[134]. M. Zahmakiran, M. Tristany, K. Philippot, K. Fajerwerg, S. Özkar, B. Chaudret, *Chem. Commun.*, **2010**, *46*, 2938–2940.

[135]. B. Sen, B. Demirkan, A. Savk, R. Kartop, M. S. Nas, M. H. Alma, S. Sürdem, F. Sen, *J. Mol. Liq.*, **2018**, *268*, 807–812.

[136]. B. Sen, A. Aygün, A. Savk, S. Duman, M. H. Calimli, E. Bulut, F. Sen, *J. Mol. Liq.*, **2019**, *279*, 578–583.

[137]. B. Bukan, S. Duman, *Int. J. Hydrogen Energy*, **2018**, *43*, 8278–8289.

[138]. S. Karaboga, S. Özkar, *Int. J. Hydrogen Energy*, **2019**, *44*, 26296–26307.

[139]. B. Sen, E. Kuyuldar, B. Demirkan, T. O. Okyay, A. Savk, F. Sen, *J. Colloid Interface Sci.*, **2018**, *526*, 480–486.

[140]. Y. Karatas, H. Acidereli, M. Gulcan, F. Sen, *Sci. Rep.*, **2020**, *10*, 7149–7159.

[141]. M. A. Khalily, M. Yurderi, A. Haider, A. Bulut, B. Patail, M. Zahmakiran, T. Uyar, *ACS Appl. Mater. Interfaces*, **2018**, *10*, 26162−26169.

[142]. S. Taçyildiz, B. Demirkan, Y. Karatas, M. Gulcan, F. Sen, *J. Mol. Liq.*, **2019**, *285*, 1–8.

[143]. V. B. Saptal, T. Sasaki, B. M. Bhanage, *ChemCatChem*, **2018**, *10*, 2593–2600.

[144]. Y. Fang, J. Li, T. Togo, F. Jin, Z. Xiao, L. Liu, H. Drake, X. Lian, H.-C. Zhou, *Chem*, **2018**, *4*, 555–563.

[145]. Y. Wang, J.-L. Li, W.-X. Shi, Z.-M. Zhang, S. Guo, R. Si, M. Liu, H.-C. Zhou, S. Yao, C.-H. An, T.-B. Lu, *Adv. Energy Mater*., **2020**, 2002138–2002149.

[146]. C. Anderson, M. Blackwell, U.S. Geological Survey, Mineral Commodity Summaries, Silver, can be found at https://www.usgs.gov/centers/nmic/silver-statistics-and-information.

[147]. X. Qian, Y. Kuwahare, K. Mori, H. Yamashita, *Chem. Eur. J.*, **2014**, *20*, 15746–15752.

[148]. K. Fuku, R. Hayashi, S. Takakura, T. Kamegawa, K. Mori, H. Yamashita, *Angew. Chem. Int. Ed.*, **2013**, *52*, 7446–7450.

[149]. L. Yang, J. Su, W. Luo, G. Cheng, *Int. J. Hydrogen Energy*, **2014**, *39*, 3360–3370.

[150]. C. Du, J. Su, W. Luo, G. Cheng, *J. Mol. Catal. A Chem.*, **2014**, *383–384*, 38–45.

[151]. L. Yang, J. Su, X. Y. Meng, W. Luo, G. Z. Cheng, *J. Mater. Chem. A*, **2013**, *1*, 10016–10023.

[152]. M. Wen, B. Sun, B. Zhou, Q. Wu, J. Peng, *J. Mater. Chem.*, **2012**, *22*, 11988–11993.

[153]. B. Sun, M. Wen, Q. Wu, J. Peng, *Adv. Funct. Mater.*, **2012**, *22*, 2860–2866.

[154]. P. Verma, Y. Kuwahara, K. Mori, H. Yamashita, *Chem. Eur. J.*, **2017**, *23*, 3616–3622.

[155]. M. Urushizaki, H. Kitazawa, S. Takano, R. Takahata, S. Yamazoe, T. Tsukuda, *J. Phys. Chem. C*, **2015**, *119*, 27483−27488.

[156]. S. Durgut, H. Ozay, *Int. J. Hydrogen Energy*, **2020**, *45*, 17649–17661. Hydrogels are cross-linked polymeric structures swelling in water that can be formed by the reaction of

various monomers. The water-holding capacity of hydrogels is due to hydrophilic functional groups contained in the polymeric structure. With these characteristics, p-sulfopropyl acrylate potassium-co-2-acrylamido-2-methylpropansulfonic acid sodium salts SPA-co-AMPS formed hydrogel was prepared in using 2- acrylamido-2-methylpropansulfonic acid (AMPS) and sulfopropyl acrylate potassium salt (SPA) monomers.

[157]. K. B. Shedd, A. Hwang, U.S. Geological Survey, Mineral Commodity Summaries, Cobalt, can be found at https://www.usgs.gov/centers/nmic/cobalt-statistics-and-information.

[158]. P. Fröhlich, T. Lorenz, G. Martin, B. Brett, M. Bertau, *Angew. Chem. Int. Ed.*, **2017**, *56*, 2544–2580.

[159]. Q. Yao, Y. Ding, Z.-H. Lu, *Inorg. Chem. Front.*, **2020**, *7*, 3837–3874.

[160]. J.-M. Yan, X.-B. Zhang, H. Shioyama, Q. Xu, *J. Power Sources*, **2010**, *195*, 1091–1094.

[161]. J. Hu, Z. Chen, M. Li, X. Zhiu, H. Lu, *ACS Appl. Mater. Interfaces*, **2014**, *6*, 13191−13200.

[162]. Z. Li, T. He, L. Liu, W. Chen, M. Zhang, G. Wu, P. Chen, *Chem. Sci.*, **2017**, *8*, 781–788.

[163]. Y. Fang, Z. Xiao, J. Li, C. Lollar, L. Liu, X. Lian, S. Yuan, S. Banerjee, P. Zhang, H.-C. Zhou, *Angew. Chem. Int. Ed.*, **2018**, *130*, 5381–5385.

[164]. S. Akbayrak, O. Taneroglu, S. Özkar, *New J. Chem.*, **2017**, *41*, 6546–6552.

[165]. D. Y. Kim, T. J. Choi, J. G. Kim, J. Y. Chang, *ACS Omega*, **2018**, *3*, 8745−8751.

[166]. H. Zhang, X. Gu, J. Song, N. Fan, H. Su, *ACS Appl. Mater. Interfaces*, **2017**, *9*, 32767−32774.

[167]. J. Song, X. Gu, Y. Cao, H. Zhang, *J. Mater. Chem. A*, **2019**, *7*, 10543–10551.

---

[168]. S. Zhang, J. Xu, H. Cheng, C. Zang, F. Bian, B. Sun, Y. Shen, H. Jiang, *ChemSusChem*, **2020**, *13*, 5264–5272.

[169]. N. Cao, J. Su, X. Hong, W. Luo, G. Cheng, *Chem. Asian J.*, **2014**, *9*, 562–571.

[170]. K. Kang, X. Gu, L. Guo, P. Liu, X. Sheng, Y. Wu, J. Cheng, H. Su, *Int. J. Hydrogen Energy*, **2015**, *40*, 12315–12324.

[171]. W. Feng, L. Yang, N. Cao, C. Du, H. Dai, W. Luo, G. Cheng, *Int. J. Hydrogen Energy*, **2014**, *39*, 3371–3380.

[172]. J. Li, Q.-L. Zhu, Q. Xu, *Catal. Sci. Technol.*, **2015**, *5*, 525–530.

[173]. Z. Wei, Y. Liu, Z. Peng, H. Song, Z. Liu, B. Liu, B. Li, B. Yang, S. Lu, *ACS Sustainable Chem. Eng.*, **2019**, *7*, 7014−7023.

[174]. Q. Wang, Z. Zhang, J. Liu, R. Liu, T. Liu, *Mater. Chem. Phys.*, **2018**, *204*, 58–61.

[175]. Z. Guo, T. Liu, Q. Wang, G. Gao, *RSC Adv.*, **2018**, *8*, 843–847.

[176]. S. Cheng, Y. Liu, Y. Zhao, X. Zhao, Z. Lang, H. Tan, T. Qiu, Y. Wang, *Dalton Trans.*, **2019**, *48*, 17499–17506.

[177]. A. Bulut, M. Yurderi, I. E. Ertas, M. Celebi, M. Kaya, M. Zahmakiran, *Appl. Catal. B*, **2016**, *180*, 121–129.

[178]. Y. Liu, J. Zhang, H. Guan, Y. Zhao, J.-H. Yang, B. Zhang, *Appl. Surf. Sci.*, **2018**, *427*, 106–113.

[179]. B. C. Filiz, A. K. Figen, S. Piskin, *Appl. Catal. A Gen.*, **2018**, *550*, 320–330.

[180]. C. Wang, L. Li, X. Yu, Z. Lu, X. Zhang, X. Wang, X. Yang, J. Zhao, *ACS Sustainable Chem. Eng.*, **2020**, *8*, 8256−8266.

[181]. J. Liao, D. Lu, G. Diao, X. Zhang, M. Zhao, H. Li, *ACS Sustainable Chem. Eng.*, **2018**, *6*, 5843−5851.

[182]. S. Guan, L. Zhang, H. Zhang, Y. Guo, B. Liu, H. Wen, Y. Fan, B. Li, *Chem. Asian J.*, **2020**, *15*, 3087–3095.

[183]. Z.-C. Fu, Y. Xu, S. L.-F. Chan, W.-W. Wang, F. Li, F. Liang, Y. Chen, Z.-S. Lin, W.-F. Fu, C.-M. Che, *Chem. Commun.*, **2017**, *53*, 705–708.

[184]. C. Tang, F. Qu, A. M. Aisri, Y. Luo, X. Sun, *Inorg. Chem. Front.*, **2017**, *4*, 659–662.

[185]. J. Zhan, Y. Duan, Y. Zhu, Y. Wang, H. Yao, G. Mi, *Mater. Chem. Phys.*, **2017**, *201*, 297–301.

[186]. H. Wu, M. Wu, B. Wang, X. Yong, Y. Liu, B. Li, B. Liu, S. Lu, *J. Energy Chem.*, **2020**, *48*, 43–53.

[187] D. Lu, J. Li, C. Lin, J. Liao, Y. Feng, Z. Ding, Z. Li, Q. Liu, H. Li, *Small* **2019**, *15*, 1805460.

[188] D. Lu, J. Liao, H. Li, S. Ji, B. G. Pollet, *ACS Sustainable Chem. Eng.* **2019**, *7*, 16474−16482.

[189] M. McRae, U.S. Geological Survey, Mineral Commodity Summaries, Nickel, can be found at https://www.usgs.gov/centers/nmic/nickel-statistics-and-information.

[190]. Ö. Metin, V. Mazumder, S. Özkar, S. Sun, *J. Am. Chem. Soc.*, **2010**, *132*, 1468–1469.

[191]. M. Mahyari, A. Shaabani, *J. Mater. Chem. A*, **2014**, *2*, 16652–16659.

[192]. P.-Z. Li, K. Aranishi, Q. Xu, *Chem. Commun.*, **2012**, *48*, 3173–3175.

[193]. C. Wang, J. Tuninetti, Z. Wang, R. Ciganda, L. Salmon, S. Moya, J. Ruiz, D. Astruc, *J. Am. Chem. Soc.*, **2017**, *139*, 11610–11615.

[194]. C. Wang, Q. Wang, F. Fu, D. Astruc, *ACC. Chem. Res.*, **2020**, *53*, 2483–2493.

[195]. J. Manna, S. Akbayrak, S. Özkar, *J. Colloid Interface Sci.*, **2017**, *508*, 359–368.

[196]. K. Guo, H. Li, Z. Yu, *ACS Appl. Mater. Interfaces*, **2018**, *10*, 517–525.

[197]. M. Gao, Y. Yu, W. Yang, J. Li, S. Xu, M. Feng, H. Li, *Nanoscale*, **2019**, *11*, 3506–3513.

[198]. Q. Lai, A. Rawal, Md Z. Quadir, C. Cazorla, U. B. Demirci, K.-F. Aguey-Zinsou, *Adv. Sustain. Syst.*, **2017**, *4*, 1700122–1700136.

[199]. Q. Lai, K.-F. Aguey-Zinsou, U. B. Demirci, *Int. J. Hydrogen Energy*, **2018**, *43*, 14498–14506.

[200]. J. Shen, N. Cao, Y. Liu, M. He, K. Hu, W. Luo, G. Cheng, *Catal. Commun.*, **2015**, *59*, 14–20.

[201]. S. Roy, P. Pachfule, Q. Xu, *Eur. J. Inorg. Chem.*, **2016**, 4353–4357.

[202]. Z. Li, Q. Pei, Y. Yu, Z. Jing, J. Wang, T. He, *ChemCatChem*, **2020**, *12*, 4257–4261.

[203]. H. Yen, Y. Seo, S. Kaliaguine, F. Kleitz, *ACS Catal.*, **2015**, *5*, 5505–5511.

[204]. Y.-H. Zhou, Q. Yang, Y.-Z. Chen, H.-L. Jiang, *Chem. Commun.*, **2017**, *53*, 12361–12364.

[205]. C. Yu, J. Fu, M. Muzzio, T. Shen, D. Su, J. Zhu, S. Sun, *ACS Chem. Mater.*, **2017**, *29*, 1413–1418.

[206]. K. Guo, Y. Ding, J. Luo, M. Gu, Z. Yu, *ACS Appl. Energy Mater.*, **2019**, *2*, 5851–5861.

[207]. K. Yang, Q. Yao, W. Huang, X. Chen, Z.-H. Lu, *Int. J. Hydrogen Energy*, **2017**, *42*, 6840–6850.

[208]. Q. Yao, Z.-H. Lu, R. Zhang, S. Zhang, X. Chen, H.-L. Jiang, *Mater. Chem. A*, **2018**, *6*, 4386–4393.

[209]. B. Qi, L. Du, F. Yao, S. Xu, X. Deng, M. Zheng, S. He, H. Zhang, X. Zhou, *ACS Appl. Mater. Interfaces*, **2019**, *11*, 23445–23453.

[210]. C.-Y. Peng, L. Kang, S. Cao, Y. Chen, Z.-S. Lin, W.-F. Fu, *Angew. Chem. Int. Ed.*, **2015**, *54*, 15725–15729.

---

[211]. C.-C. Hou, Q. Li, C.-J. Wang, C.-Y. Peng, Q.-Q. Chen, H.-F. Ye, W.-F. Fu, C.-M. Che, N. Lopez, Y. Chen, *Energy Environ. Sci.*, **2017**, *10*, 1770–1776.

[212]. X. Qu, R. Jiang, Q. Li, F. Zeng, X. Zheng, Z. Xu, C. Chen, J. Peng, *Green Chem.*, **2019**, *21*, 850–860.

[213]. Y. Shi, B. Zhang, *Chem. Soc. Rev.*, **2016**, *45*, 1529–1541.

[214]. Q. Yao, Z.-H. Lu, Y. Yang, Y. Chen, X. Chen, H.-L. Jiang, *Nano Res.*, **2018**, *11*, 4412–4422.

[215]. S. Buxton, E. Garman, K. E. Heim, T. Lyons-Darden, C. E. Schlekat, M. D. Taylor, A. R. Oller, *Inorganics*, **2019**, *7*, 89–127. Nickel notable human health toxicity effects identified from human and/or animal studies include respiratory cancer, non-cancer toxicity effects following inhalation, dermatitis, and reproductive effects. See also ref [216-217].

[216]. T. P. Coogan, D. M. Latta, E. T. Snow, M. Costa, *CRC Crit. Rev. Toxicol.*, **1989**, *19*, 341–384. Excess risk of carcinogenicity (lung and nasal) with nickel compounds represents the most widely recognized toxicity associated with nickel exposure.

[217]. R. Magaye, J. Zhao, L. Bowman, M. Ding, *Exp. Ther. Med.*, **2012**, *4*, 551–561. The carcinogenic potential of cobalt and its compounds were evaluated by IARC in 1991, which concluded that there was inadequate evidence for carcinogenicity in humans (lung cancer) but sufficient evidence in experimental animals.

[218]. L. Leyssens, B. Vinck, C. Vand Der Straeten, F. Wuyts, L. Maes, *Toxicology*, **2017**, *387*, 43–56. The risk of lung cancer related to inhalation of Co-containing dusts has been considered while it may be not causative agent, especially within tungsten carbide.

[219]. D. M. Flanagan, U.S. Geological Survey, Mineral Commodity Summaries, Copper, can be found at https://www.usgs.gov/centers/nmic/copper-statistics-and-information.

[220]. M. Zahmakiran, F. Durap, S. Özkar, *Int. J. Hydrogen Energy*, **2010**, *35*, 187–197.

---

[221]. Y. Yang, Z.-H. Lu, Y. Hu, Z. Zhang, W. Shi, X. Chen, T. Wang, *RSC Adv.*, **2014**, *4*, 13749–13752.

[222]. Q. Yao, Z.-H. Lu, Z. Zhang, X. Chen, Y. Lan, *Sci. Rep.*, **2014**, *4*, 7597–7603.

[223]. S.-J. Li, H.-L. Wang, J.-M. Yan, Q. Jiang, *Int. J. Hydrogen Energy*, **2017**, *42*, 25251–25257.

[224]. H.-L. Jiang, T. Akita, Q. Xu, *Chem. Commun.*, **2011**, *47*, 10999–11001.

[225]. X. Meng, L. Yang, N. Cao, C. Du, K. Hu, J. Su, W. Luo, G. Cheng, *ChemSusChem*, **2014**, *79*, 325–332.

[226]. H. Zhang, X. Wang, C. Chen, C. An, Y. Xu, Y. Huang, Q. Zhang, Y. Wang, L. Jiao, H. Yuan, *Int. J. Hydrogen Energy*, **2015**, *40*, 12253–12261.

[227]. N. Cao, K. Hu, W. Luo, G. Cheng, *J. Alloys Compd.*, **2014**, *590*, 241–246.

[228]. P. Pachfule, X. Yang, Q.-L. Zhu, N. Tsumori, T. Uchida, Q. Xu, *J. Mater. Chem. A*, **2017**, *5*, 4835–4841.

[229]. F.-Z. Song, Q.-L. Zhu, X.-C. Yang, Q. Xu, *ChemNanoMat*, **2016**, *2*, 942–945.

[230]. K. Feng, J. Zhong, B. Zhao, H. Zhang, L. Xu, X. Sun, S.-T. Lee, *Angew. Chem. Int. Ed.*, **2016**, *55*, 11950–11954.

[231]. T. Karaca, M. Sevim, O. Metin, *ChemCatChem*, **2017**, *9*, 4185–4190.

[232]. M. Gao, W. Yang, Y. Yu, *Int. J. Hydrogen Energy*, **2018**, *43*, 14293–14300.

[233]. K. Güngörmez, Ö. Metin, *Appl. Catal. A*, **2015**, *494*, 22–28.

[234]. Y.-H. Zhou, X. Cao, J. Ning, C. Ji, Y. Cheng, J. Gu, *Int. J. Hydrogen Energy*, **2020**, *42*, 31440–31451.

[235]. H. Zheng, K. Feng, Y. Shang, Z. Kang, X. Sun, J. Zhong, *Inorg. Chem. Front.* **2018**, *5*, 1180–1187.

---

[236]. K. Yang, L. Zhou, X. Xiong, M. Ye, L. Li, Q. Xia, *Micropor. Mesopor. Mat.*, **2016**, *225*, 1–8.

[237]. Z. Liang, X. Xiao, X. Yu, X. Huang, Y. Jiang, X. Fan, L. Chen, *J. Alloys Compd.*, **2018**, *741*, 501–508.

[238]. Q. Yao, K. Yang, X. Hong, X. Chen, Z.-H. Lu, *Catal. Sci. Technol.*, **2018**, *8*, 870–877.

[239]. K. Aranishi, H.-L. Jiang, T. Akita, M. Haruta, Q. Xu, *Nano Res.*, **2011**, *4*, 1233–1241.

[240]. H.-L. Wang, J.-M. Yan, Z.-L. Wang, Q. Jiang, *Int. J. Hydrogen Energy*, **2012**, *37*, 10229–10235.

[241]. Z.-H. Lu, J. Li, A. Zhu, Q. Yao, W. Huang, R. Zhou, R. Zhou, X. Chen, *Int. J. Hydrogen Energy*, **2013**, *38*, 5330–5337.

[242]. X. Meng, L. Yang, N. Cao, C. Du, K. Hu, J. Su, W. Luo, G. Cheng, *ChemPlusChem*, **2014**, *79*, 325–332.

[243]. D. R. Abd El-Hafiz, G. Eshaq, A. E. ElMetwally, *Mater. Chem. Phys.*, **2018**, *217*, 562–569.

[244]. O. V. Komova, G. V. Odegova, A. M. Gorlova, O. A. Bulavchenko, A. A. Pochtar, O. V. Netskina, V. I. Simagina, *Int. J. Hydrogen Energy*, **2019**, *44*, 24277–24291.

[245]. R. Tahawy, E. Doustkhah, E. A. Abdel-Aal, M. Esmat, F. E. Farghaly, H. El-Hosainy, N. Tsunoji, F. I. El-Hosiny, Y. Yamauchi, M. H. N. Assadi, Y. Ide, *Appl. Catal. B*, **2021**, *286*, 119854–119862.

[246]. P. Bhattacharya, J. A. Krause, H. Guan, *J. Am. Chem. Soc.*, **2014**, *136*, 11153−11161.

[247]. A. Glüer, M. Förster, V. R. Celinski, J. Schmedt auf der Günne, *ACS Catal.*, **2015**, *5*, 7214–7217.

[248]. S. Murugesan, K. Kirchner, *Dalton Trans.*, **2016**, *45*, 416–439.

[249]. H. Huang, C. Wang, Q. Li, R. Wang, Y. Yang, A. Muhetaer, F. Huang, B. Han, D. Xu, *Adv. Funct. Mater.* **2021**, *31*, 2007591.

[250]. A. Gutowska, L. Li, Y. Shin, C. M. Wang, X. S. Li, J. C. Linehan, R. S. Smith, B. D. Kay, B. A. Schmid, W. J. Shaw, *Angew. Chem., Int. Ed.* **2005**, *44*, 3578.

[251]. M. P. Confer, A. DeSimone, H. Burnham, W. McLeod, T. M. Klein, S. C. Street, D. A. Dixon, *Int. J. Hydrogen Energy*, **2021**, *46*, 10801–10808.

[252]. J.-K. Sun, W.-W. Zhan, T. Akita, Q. Xu, *J. Am. Chem. Soc.*, **2015**, *137*, 7063–7066.

[253]. N. Tunç, M. Rakap, *Renewable Energy*, **2020**, *155*, 1222–1230.

[254]. Z.-H. Lu, Q. Yao, Z. Zhang, Y. Yang, X. Chen, *J. Nanomater.*, **2014**, 729029, https://doi.org/10.1155/2014/729029.

[255]. R. Moury, U. B. Demirci, *Energies*, **2015**, *8*, 3118–3141.

[256]. Conversely, in the case of the NH_3 group of AB dehydrogenation is not achievable at RT, limiting thus the theoretical gravimetric hydrogen storage capacity of NH_3BH_3-$3H_2O$ to 7.1 wt% vs. 10.0 wt% theoretically for $N_2H_4BH_3$-$3H_2O$, see ref [255].

[257]. Q.-L. Zhu, D.-C. Zhong, U. B. Demirci, Q. Xu, *ACS Catal.*, **2014**, *4*, 4261−4268.

[258]. Z. Zhang, Z.-H. Lu, H. Tan, X. Chen, Q. Yao, *J. Mater. Chem. A*, **2015**, *3*, 23520–23529.

[259]. K. Yang, Q. Yao, W. Huang, X. Chen, Z.-H. Lu, *Int. J. Hydrogen Energy*, **2017**, *42*, 6840–6850.

[260] Q. Yao, Z.-H. Lu, R. Zhang, S. Zhang, X. Chen, H.-L. Jiang, *J. Mater. Chem. A*, **2018**, *6*, 4386–4393.

[261]. J. Chen, Z.-H. Lu, Q. Yao, G. Feng, Y. Luo, *J. Mater. Chem. A*, **2018**, *6*, 20746–20752.

[262]. S.-J. Li, H.-L. Wang, B.-R. Wulan, X.-B. Zhang, J.-M. Yan, Q. Jiang, *Adv. Energy Mater.*, **2018**, *8*, 1800625–1800632.

---

[263]. Q. Yao, M. He, X. Hong, X. Chen, G. Feng, Z.-H. Lu, *Int. J. Hydrogen Energy*, **2019**, *44*, 28430–28440.

[264]. H. Zou, F. Guo, M. Luo, Q. Yao, Z.-H. Lu, *Int. J. Hydrogen Energy*, **2020**, *45*, 11641–11650.

[265]. M. Rakap, *Int. J. Hydrogen Energy*, **2020**, *45*, 15611–15617.

[266]. H. C. Kelly, J. O. Edwards, *Inorg. Chem.*, 1963, *2*, 226–227.

[267]. S. Sahler, H. Konnerth, N. Knoblauch, M. H. G. Prechtl, *Int. J. Hydrogen Energy*, **2013**, *38*, 3283–3290.

[268]. R. Kumar, A. Karkamkar, M. Bowden, T. Autrey, *Chem. Soc. Rev.*, **2019**, *48*, 5350–5380.

[269]. M. Engin, O. Ozay, *Int. J. Hydrogen Energy*, **2018**, *43*, 15083–15094.

[270]. A. Onder, O. Ozay, *Int. J. Hydrogen Energy*, **2020**, *45*, 11651–11661.

[271]. H. Ozay, P. Ilgin, M. K. Sezgintürk, O. Ozay, *Int. J. Hydrogen Energy*, **2020**, *45*, 9892–9902.

[272]. H. Ozay, P. Ilgin, O. Ozay, *Int. J. Hydrogen Energy*, **2020**, *45*, 17613–17624.

[273]. H. Ozay, P. Ilgin, M. K. Sezgintürk, O. Ozay, *Renew. Energy*, **2020**, *155*, 500–512.

[274]. Y. Ge, X. Qin, A. Li, Y. Deng, L. Lin, M. Zhang, Q. Yu, S. Li, M. Peng, Y. Xu, X. Zhao, M. Xu, W. Zhou, S. Yao, D. Ma, *J. Am. Chem. Soc.*, **2021**, *143*, 628–633.

[275]. L. Wang, H. Li, W. Zhang, X. Zhao, J. Qiu, A. Li, X. Zheng, Z. Hu, R. Si, J. Zeng, *Angew. Chem. Int. Ed.*, **2017**, *56*, 4712–4718.

[276]. T. Zhang, A. G. Walsh, J. Yu, P. Zhang, *Chem. Soc. Rev.*, **2021**, *50*, 569–588.

[277]. C.-C. Hou, H.-F. Wang, C. Li, Q. Xu, *Energy Environ. Sci.*, **2020**, *13*, 1658–1693.

[278]. M. Boudjelel, E. D. Sosa Carrizo, S. Mallet-Ladeira, S. Massou, K. Miqueu, G. Bouhadir, D. Bourissou, *ACS Catal.*, **2018**, *8*, 4459−4464.

[279]. C. Wang, D. Astruc, *Chem. Soc. Rev.*, **2021**, *50*, 3437–3484.

[280]. U. B. Demirci, *Energy Technol.*, **2018**, *6*, 470–486.

[281]. C. A. Castilla-Martinez, R. Moury, U. B. Demirci, *Int. J. Hydrogen Energy*, **2020**, *45*, 30731–30755.